# DESIGN AND FABRICATION OF IRIDIUM OXIDE ($IRO_X$)-BASED MULTI-ELECTRODE ARRAY FOR BIOMEDICAL SENSORS

by

CUONG MANH NGUYEN

Presented to the Faculty of the Graduate School of

The University of Texas at Arlington in Partial Fulfillment

of the Requirements

for the Degree of

DOCTOR OF PHILOSOPHY

THE UNIVERSITY OF TEXAS AT ARLINGTON

MAY 2015

Acknowledgements

I would like to express my deepest appreciation and gratitude to Dr. Jung-Chih Chiao, my supervisor for his continuous support and guidance to achieve this milestone in my research career. His deep knowledge, vision and prompt advices are indeed helpful for me to overcome failures and challenges during the course of my research. Dr. Chiao's patient training and belief in my abilities give me the courage and confidence to conduct experiments, explore new ideas and processes. Under his mentorship, I have chances to attend many international and regional conferences, where I exposed to experts and professors in my research fields. I am very fortunate to have fully support to access to the iMEMS laboratory's resources including equipment, machines, computers, software and textbooks as well as the collaborators' laboratories. Without his support, this dissertation could not be finished.

I am also grateful to Dr. Jonathan Bredow for being my committee member and for supporting me while I worked as the Graduate Teaching Assistant for the Electromagnetics Laboratory. This was one of the most interesting lab sections I assisted, and I have leant and gained so much "hand-on" experiences. My thanks also go to Dr. Michael Vasilyev, Dr. Weidong Zhou and Dr. Harry F. Tibbals for taking interest in my research and accept to serve as the members of my comprehensive and dissertation committees. Their sharp suggestions are invaluable and very important for me to understand and look at issues in different angles.

I am thankful to Dr. Smitha Rao for the guidance, advices, and ideas she provided throughout my research works. She is very nice, patient and tolerate in helping me with professional writing. I have learnt so much from her personality, wisdom, thoughtfulness and enthusiasm in doing research.

I would like to thank Dr. Hung Cao for unlimited help since I first came to the USA. He was the first one who guided me go through every steps of how to do research, conduct experiments and analyze data. Some of his experiment setups and designs of sensors are still very useful for me to deploy new ideas and concepts. I also express my thanks to Ms. Trang Thai and Dr. Nha Nguyen for being my friends and buddies. They are the greatest friends that I can share everything in my life and my research.

This work would not have been possible without the help and suggestions of members, past and present of iMEMS Research group. I would like to express my thanks to Mr. Indra Gurung, Mr. Jeff Mays, Mr. James Oh, and Mr. Kyle Schadt who worked closely with me in many research projects. They are very smart and hard-working. My thanks also go to Dr. Uday Tata, Dr. Wen-ding Huang, Dr. Aydin Farajidavar, Mr. Minh Q. Nguyen, Mr. Souvik Dubey, and Mrs. Xuesong Yang for collaboration, suggestion and constructive criticism.

Finally, from the bottom of my heart, I am thankful to my father Mr. Nguyen Van Dong and my mom Mrs. Nguyen Thi Bich for their love and blessings. They always stand by me, encourage me to pursue my dreams and support me in whatever I do. I feel very fortunate to have my caring brother Mr. Nguyen Hung Cuong and my sister-in-law Mrs. Bui Thi Thu Trang. They have been taking care of my parents while I am staying so far away from home. I also want to dedicate my work to my dear and loving nephews Nguyen Hai Phong and Nguyen Hai Anh.

March 20, 2015

Abstract

DESIGN AND FABRICATION OF IRIDIUM OXIDE ($IRO_X$)-BASED MULTI-ELECTRODE ARRAY FOR BIOMEDICAL SENSORS

CUONG NGUYEN, PhD

The University of Texas at Arlington, 2015

Supervising Professor: Jung-Chih Chiao

Multi-electrode array (MEA) has emerged as one of the most important and common tools to monitor physiological and biological signals. Advanced micro-electro-mechanical systems (MEMS) and innovative nanofabrication technologies provide means to fabricate micro-scale MEAs for implantable bio-applications. One of the prominent advantages of such miniature electrodes is to minimize tissue damage or injuries during surgical implantation. The micro-scale electrodes are normally coated with materials or functionalized with proteins and enzymes to sense different analyates. Iridium oxide ($IrO_x$) owning with many important traits such as biocompatibility, high corrosion resistance in electrolyte materials, pH-sensitivity, large surface-to-volume ratio, and high charge storage has a broad range of applications in electrochemistry and biology. In this dissertation, bulk and nanostructured $IrO_x$ were grown for micro-MEAs on both flexible and rigid substrates for various applications such as pH sensors, dopamine and L-glutamate sensors.

Bulk $IrO_x$ was fabricated on a flexible substrate in a sol-gel dip-coating method. The two-step heat treatment process enables deposition within micro-scale electrodes. The flexible substrate was spin-coated with a thick SU-8 layer acting as a sacrificial mask to define exposing areas to iridium chloride solution. The sacrificial mask was then peeled off by bending the substrate after a first heat-treatment step. The layer of iridium oxide was

formed in a hard treatment step in an inert-gas Blue-M oven. Various dimensions of sol-gel $IrO_x$ electrodes including 1 mm × 1 mm, 500 µm × 500 µm, 100 µm × 100 µm and 50 µm × 100 µm were fabricated. The fabrication method yielded reliable $IrO_x$-based sensors with stable and repeatable responses. Sensor longevity and pH dependence were investigated by immersing the electrodes in hydrochloric acid, fetal bovine serum (FBS), and sodium hydroxide solutions for 30 days. A bending experiment of the flexible electrodes was also examined with different curvature surfaces. The fabrication method is suitable to make micro-pH sensors or micro-pseudo-reference electrodes for L-glutamate biosensors.

Nanostructured $IrO_x$ was implemented on the MEA in a template-based fabrication method. The nano-porous anodic aluminum oxide (AAO) template was locally created on sensing surface of the MEA in a localized anodization process. Two types of morphologies including $IrO_x$ nanorods and nanotubes were studied. High aspect ratio iridium (IV) oxide nanorods have been successfully grown in a chemical co-precipitation method. The nanorods with an aspect ratio of 22 can be synthesized within 45 minutes. X-ray diffraction measurement unveiled the crucial role of the AAO template that oriented and aligned the growth of $IrO_2$ nanorods along the [110] crystallography direction. Large surface area of the $IrO_2$ nanostructures exhibiting a high capacitive property can be utilized in supercapacitors or sensing applications. The fabrication process allowed to grow $IrO_x$ nanorods on the micro-scale sensing surfaces of dopamine sensors.

$IrO_x$ nanotubes was grown on microelectrodes in an electrodeposition process with support of nanoporous AAO templates. The microelectrodes had dimension of 50 µm × 100 µm. The free-standing nanotubes with a diameter ranging from 80 to 110 nm were yielded, corresponding to the AAO pore sizes. Material characterization was carried out with energy-dispersive X-ray spectroscopy, scanning electron microscopy and

transmission electron microscopy to confirm nanotube structures. Potentiometric responses of the miniature sensors to hydrogen ions in terms of sensitivity, repeatability, and response time were performed. Super-Nernstian response was achieved. The pH measurements for higher resolution targeting biological applications and sensor temperature dependence were also conducted.

The platform of the MEAs fabricated in both flexible and rigid substrates using high-throughput, reproducible and cost-effective processes can be applied for different types of electrochemical sensors. Circuit design of the dedicated low-energy, low-noise, and high-gain recording system was deployed. The research proposed a capability to produce a comprehensive and compact multi-functional MEA featuring with signal processing for wireless sensing bio-applications.

Table of Contents

List of Illustrations

List of Tables

List of Abbreviations

| | |
|---|---|
| AAO | Anodic Aluminum Oxide |
| ECG | Electrocardiogram |
| EDS | Energy Dispersive X-Ray Spectroscopy |
| EEG | Electroencephalogram |
| $IrO_2$ | Iridium (IV) Oxide |
| $IrO_x$ | Iridium Oxide |
| MEA | Micro-Electrode Array |
| MEMS | Micro-Electro-Mechanic System |
| Parylene | poly(p-xylylene) |
| pCO2 | Partial Pressure of Carbon Dioxide |
| pH | Potential of Hydrogen |
| pO2 | Partial Pressure of Oxygen |
| SEM | Scanning Electron Microscopy |
| SEoM | Standard Error of the Mean |
| TEM | Transmission Electron Microscopy |
| XRD | X-ray Diffraction |

# Chapter 1

# INTRODUCTION

## 1.1 Motivation

Clinical analyses and tests become more expensive, laborious and time-consuming. Non-hospital point-of-care allows continuous and convenience ways to monitor health conditions by patients at home or in various locations. These demands require developing wearable, telemetry and multi-functional sensing systems. The development of advanced technologies and wireless communication provides effective solutions to quickly connect and share data from multiple devices to servers. However, one of the remained challenges and difficult parts is the development of *in situ* sensors for rapid analyses with high accuracy and sensitivity. Implantable electrochemical sensors have emerged as one of the attractive means for sensing and monitoring biological conditions such as pH, pO2, and pCO2 [1-3]; physiological signals such as ECG, EEG [4]; and biological analytes such as glucose, lactate, uric acid, neurotransmitters [5-7]. Since the sensors are in-contact with the sensing sites, their measurement was updated instantaneously and continuously with high spatial and temporal resolution [4]. In addition, multiple microelectrode arrays (MEAs) with multi-functional sensing have become doable while still remaining the miniature dimensions of the implantable probes [8, 9].

Recently, there is a growing interest to miniaturize the implantable sensors for long-term recording [10]. Several advantages of smaller sensors are widely acknowledged including minimization of local tissue damage, reduction of inflammation, and improvement of large-scale integration [11-13]. Advancements in MEMS and micromachining technologies play a substantial role in the quest for miniaturizing the implantable sensors with batch production. Fabrication technologies also allow integrating MEAs on different substrates such as silicon, ceramic, glass and polyimide.

One of the biggest challenges for miniatures sensors is signal strength. The smaller sensors are, the weaker signal strength as well as the higher electrode impedance are. These electrical properties consequently bring several limitations in design of the acquisition systems. Firstly, more amplifier stages and higher amplifier gains are required to condition sensor signals. Secondly, pre-filter and impedance matching circuitry are included to reduce ambient noise and pick up small-signals. Thirdly, power consumption of these additional amplifier stages may become a critical issue with the wearable acquisition system having limited power source. Therefore, the crucial aim of my research works is to improve signal strength of the micro-electrodes while remaining their small footprints.

## 1.2 Methods and Approaches

Improving roughness of the sensing surface resulting increase of electroactive area offers a means of improving signal strength of the MEAs. Several methods have been utilized. The 3-D nanostructured materials grown on the surface of the micro-sensors became our interests. Since our ultimate goal is to implement such sensors for biomedical applications, the biocompatible nanostructured materials are considered. Conducting metallic oxides which possess high thermal and chemical stability such as ZnO, $OsO_2$, $RuO_2$, $TiO_2$, $IrO_x$ have been used as materials for durable electrodes in electrochemical studies [14-20]. Among these materials, iridium oxide ($IrO_x$) has received considerable attention due to its stable electrical transport properties [21-24]. In electrochemistry, $IrO_x$ is commonly used for pH sensors since it has stable sensitivity over a wide pH range, fast responses and less potential drifts [9, 25]. Moreover, endowed with lower impedance and higher charge storage capacity, $IrO_x$ has been suggested as a suitable material for electrochemical supercapacitors [19, 23, 26]. In addition, $IrO_x$ has been preferred for enzyme-based biosensors or neuro-stimulating electrodes due to its important traits of

biocompatibility, corrosion resistance in electrolyte solutions and antifouling ability for long-term usage [27, 28]. Therefore, in my dissertation, I am focusing on the fabrication methods of $IrO_x$ nanostructures and their applications including neurotransmitter sensors, pH sensors and supercapacitors.

Sol-gel-based fabrication was widely known as a simpler, high-throughput and cost-effective method for bulk $IrO_x$. The sol-gel-based method is of my interest within the scope of this work because it yielded micro-and macro-pores providing highly rough areas. Conventional method successfully yield $IrO_x$ over a large area. In my work, I also developed and compared different ways to produce bulk $IrO_x$ on a micro-area including implementation of microfluidic dispersive channels or employment of a sacrificial masks. The sol-gel-based $IrO_x$ has been utilized as materials for the pseudo-reference electrode of an amperometric sensor in biomedical applications. Additionally, preliminary experiments were deployed to show possibility to implement $IrO_x$ for both reference and working electrodes in these sensors. Due to less change in pH of the biological environment, which was also demonstrated, the $IrO_x$-based amperometric sensors with interchangeable working and reference electrodes were proposed with small errors or insignificant distortion.

## 1.3 Specific Aims

1. Design and fabricate platform of miniature multi-electrode array using MEMS technologies on flexible and rigid substrates.
2. Investigate the form of anodic aluminum oxide (AAO) template over the MEAs.
3. Investigate the growth of $IrO_x$ nanorods on micro-electrodes in a chemical bath deposition with the support of an AAO template and the use for micro-neurotransmitter sensors.

4. Investigate the growth of $IrO_x$ nanotubes on micro-electrodes in an electrodeposition process with the support of an AAO template and the use for micro-pH sensors.
5. Investigate the growth of bulk $IrO_x$ in a sol-gel dip-coating process and the use for pseudo-reference and working electrodes of electrochemical sensors.

## 1.4 Dissertation Organization

The dissertation is organized as follows: Chapter 2 will dedicate for fabrication processes of the MEAs. General MEMS-based fabrication processes will be described in details. The objective of the part is provide fundamental information of the platform of the MEAs which will be used throughout my work. Localized anodization process will also be utilized to generate nanoporous AAO template. Chapter 3 will focus on integration the $IrO_x$ nanorods on the aforementioned microsensors. Chemical bath deposition method and its mechanism will be discussed. The microsensors featured with nanorod structures will be demonstrated for dopamine sensors. Cyclic voltammetry and amperometric experiments were carried out to show improvement in surface roughness. In Chapter 4, the fabrication of $IrO_x$ nanotube structure will be described in an electrodeposition methods. The $IrO_x$ nanotubes improve signal strength of the micro pH sensors. Properties of high resolution, low-temperature dependence, and stability are investigated. In Chapter 5, I focus on the sol-gel dip-coating method to fabricate bulk $IrO_x$ within micro-areas. One of the applications is to fabricate pseudo-reference electrodes for electrochemical sensors. Long-term stability, bio-compatibility and highly corrosive resistance to electrolytes in biological environments allow $IrO_x$-based electrodes to become an alternative choice for the standard Ag/AgCl reference electrodes. Future work as described in Chapter 6 demonstrates the next generation of MEA fabricated on an ultra-thin and flexible substrate. The substrate made of biocompatible Parylene-C film is preferred in implantable applications because it

minimize tissue damage; however, it faces difficulties to penetrate into a body tissue during surgical implantation. The stiffness of the probe will be improved with an encapsulated biodegradable layer for surgical implantation. The layer will be degraded after insertion to expose the sensing area.

# Chapter 2

# LOCALIZED ANODIZATION AND THE FORM OF $IRO_X$ NANOSTRUCTURES ON MEAs

## 2.1 Introduction

Iridium oxide nanostructures have recently attracted a considerable interest due to their unique properties including water oxidation catalysis, high charge storage and wide pH sensing range [9, 29, 30]. Endowed with biocompatibility properties, $IrO_x$ nanostructures with high surface-to-volume ratios are also promisingly utilized to improve sensing capability of biosensors [31, 32]. Currently, several different methods have been reported to grow $IrO_x$ nanostructure. Non-template-based methods such as metal organic chemical vapor deposition and physical deposition techniques have been applied to grow well-aligned and highly-ordered $IrO_x$ nanowires [18, 23]. Although these techniques can be implemented on patterned electrodes, they require sophisticated equipment and multiple fabrication steps under precisely controlled conditions such as temperature and pressure. On the other hand, template-based methods including chemical bath deposition and electrodeposition technique using commercial polycarbonate membranes face issues of incorporating the templates onto pre-patterned electrodes [18].

Nanoporous anodic aluminum oxide (AAO) films grown by cost-effective, highly reproducible and controllable manufacturing processes have emerged as popular templates in the fabrication of nanostructures [33-35]. Up to now, the self-ordered nanoporous AAO have been commonly fabricated using aluminum sheets to produce nanostructures with high aspect ratios [33, 34]. However, this approach has trade-offs in incorporation of AAO membrane with a stable and permanent substrate such as a silicon wafer. M. Wesche *et al*. proposed another approach to anodize a layer of aluminum sputtered on a silicon wafer. The method was applied to fabricate the AAO template on microelectrodes for cell-based applications [36]. Although the method successfully

produced the favorable alumina membrane directly on a silicon substrate, the template was formed not just on desired areas but the entire wafer.

In this section, we investigated the feasibility of fabricating an AAO template on pre-patterned micro-scale areas using standard nanofabrication technology and localized anodization processes. The AAO template is later used as a supportive layer to grow either $IrO_x$ nanorods or nanotubes. The growth of different nanostructure morphologies will be discussed in Chapter 3 and 4.

## 2.2 Design of Fabrication Processes

The fabrication procedures of the micro pH sensing electrodes are depicted in Figure 2-1. First, a 550-μm thick *p*-type silicon wafer was cleaned with buffered HF solution (BHF). Afterwards, a layer of 500-nm thick silicon dioxide for electrical insulation was grown by a wet-thermal oxidation process, as shown in the Figure 2-1(a). Then, a layer of NR-9-1500PY negative photoresist (*Futurrex*) was spin-coated at speed of 1700 rpm for 45 seconds (Appendix A). According to our experimental results, the negative photoresist was preferred for lift-off process. Then, photolithographically patterned to create the bases of microelectrodes and connection lines (Figure 2-1(b)).

The sacrificial photoresist layer was removed in acetone, according to the lift-off process after deposition of layers of metals (900-nm thick aluminum, 10-nm thick gold and 150-nm thick titanium), as shown in Figure 2-1(c)-(d). Titanium and gold layers were deposited by electron beam evaporation while the aluminum layer was sputter-deposited [37]. The reasons of using titanium and gold for the metallic supportive layers are discussed later in the section 2.3.

Next, a passivation layer of 3.5-μm thick SU-8 (*MicroChem*) was spin-coated and patterned (Figure 2-1(e)). The choice of SU-8 for the passivation layer is because of its biocompatibility, high stability and durability. Figure 2-1(e) illustrates that the SU-8 layer

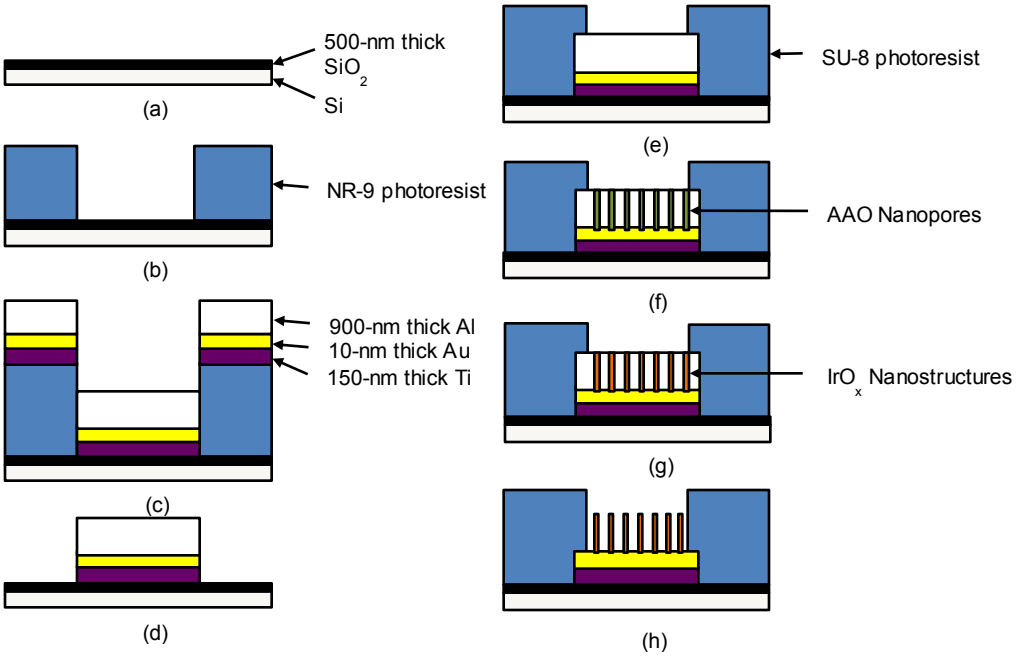


Figure 2-1: Fabrication process: (a) thermal oxidation to grow a 500-nm thick $SiO_2$ layer; (b) patterning micro-electrodes; (c) depositing metallic supportive materials; (d) lift-off; (e) patterning sensing areas; (f) localized anodization process to create nanoporous AAO template; (g) deposition of $IrO_x$ nanostructures; (h) dissolving AAO membrane to release $IrO_x$ nanotubes.

covered the entire microelectrode except for sensing sites and bonding pads. The sensing sites of each microelectrode had a dimension of 50×100 $\mu m^2$ while the bonding pads were designed to be much larger for convenience to make connections for signal processing circuits and recording purposes. Finally, cooper conductive connection lines were connected to the bonding pads using silver epoxy (*MG Chemicals 8331*), as shown in Figure 2-2(a).

The localized anodization process was carried out to form a supportive nanoporous AAO template (Figure 2-1(f)). The aluminum layer on top of the microelectrode arrays was anodized by a home-built two-electrode electrochemical cell. The actual experiment setup is shown in Figure 2-2(b). A platinum rod acted as a cathode while the

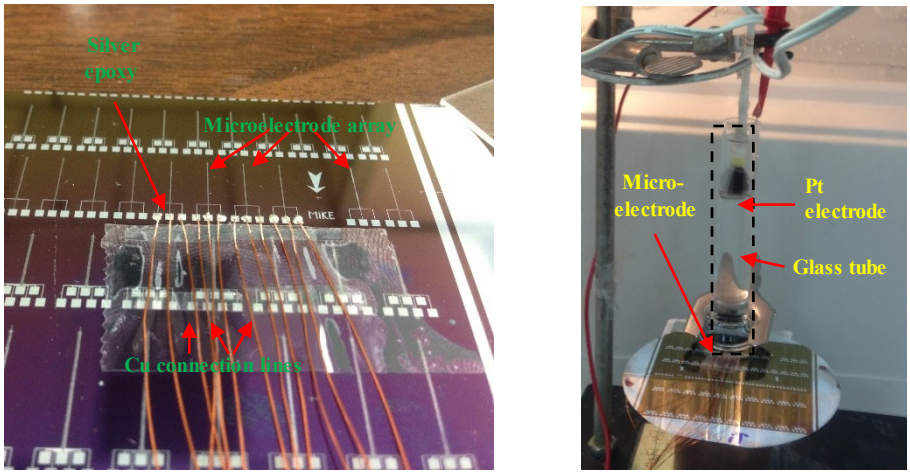


(a) (b)

Figure 2-2: (a) Microelectrode arrays with connection lines; (b) Setup of a two-electrode electrochemical cell for localized anodization.

anode was connected to the microelectrodes through conductive connection lines. Multiple microelectrodes were also connected to the anode in order to improve throughput of the experiment. A glass tube (*TGP Inc.*) contained sufficient amount of 0.023-M oxalic acid (*Ricca Chemical*) solution as electrolytes for the anodization process [31]. Anodization process was conducted at different voltages to investigate their effects on the morphology of AAO nanopores on patterned microelectrodes. According to our observations, the anodization process has been done with an estimated rate of approximately 45-nm/minute. Therefore, the total time for this step was controlled to stop after 20-minutes controlled by a customer-made program based in LabVIEW.

Afterwards, the pore-widening process was conducted in order to increase pore sizes of the AAO template as well as to remove undesirable aluminum oxide barrier area at the bottom of nanopores. The pore-widening step was carried out by dripping solution of phosphoric acid (*Em Science*) 10wt% onto the anodizing area of each microelectrode. Since each electrode has been patterned to have a total opening area of 5000 $\mu m^2$, a drop of phosphoric acid was enough for each microelectrode. The pore widening time was

varied in order to evaluate its effects on the morphology of AAO nanopores on the patterned microelectrodes.

Figure 2-2(g) describes the growth of $IrO_x$ nanostructures inside each nanopore of the AAO template. Different growing methods targeting to different morphologies will be described later in Chapter 3 and 4. The sacrificial AAO template plays an important role to orient and support the growth of the nanostructures. The final step of the fabrication processes is shown in the inset of Figure 2-1(h). The microelectrodes were immersed in a solution of 0.1-M KOH (*Em Science*) for 2 hours in order to dissolve the sacrificial AAO template. It should be noted that the alkaline solution may have side effect on the SU-8 passivation layer; thus, the step should not last more than 4 hours. .

## 2.3 Characterization of the Metallic Supportive Layers

The metallic supportive layers underneath the AAO membrane are essential to conduct charges for the anodization process as well as to transmit signals from the sensing sites. Thus, they require high conductivity, durability and stability. Some common materials such as copper, titanium, gold and platinum were considered. Although copper has exhibited compatibility with the anodized aluminum process and the formation of AAO nanotemplate in our preliminary investigation, the material is not preferred for long-term experiment, especially in biosensors. The anodization processes were carried out on macro-areas of 3.14 $cm^2$ at an anodization voltage of 40 V for 20 minutes in order to find the most compatible material. We monitored the anodization current as a control parameter for the anodization process. Figure 2-3 illustrates the anodization currents of samples using titanium, gold and platinum as the metallic supportive materials.

It shown that while the anodization current of the sample using Ti decreased at the end of the process, it increased drastically with other samples. It could be explained that

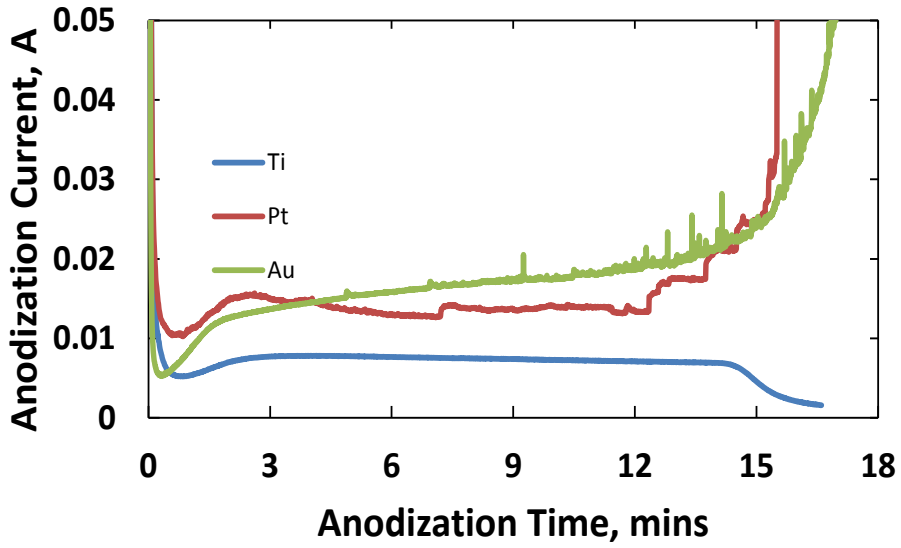


Figure 2-3: Anodization currents of different samples with different metallic supportive layers: Ti, Pt and Au. The processes were done on macro-areas of 3.14 $cm^2$ at an anodization voltage of 40 V for 20 minutes.

when the AAO nanopores created by anodizing aluminum reached the Al-Ti boundaries, the redox-reaction ceased since titanium was less anodized in oxalic acid solution [35]. In the case of inert materials such as gold and platinum, the redox-reaction of oxidizing water became more prominent in the end of the anodization process. This reaction generated heat and gas bubbles, which consequently loosened the adhesion of the AAO membrane and its metallic supportive layer. Therefore, we observed the increase of electrical currents. Thus, titanium becomes a material of choice for the metallic supportive layer to fabricate AAO membrane. However, gold has been commonly known as a favorable material for biosensors and electrochemical sensors because of its biocompatibility and small electrode/electrolyte interface impedance [36]. Therefore, we use the combined 150-nm Ti and 10-nm Au layers in our sensors.

Figure 2-4 shows scanning electron microscopy (SEM) photos of nanoporous AAO template on a patterned microelectrode. The AAO template was created when

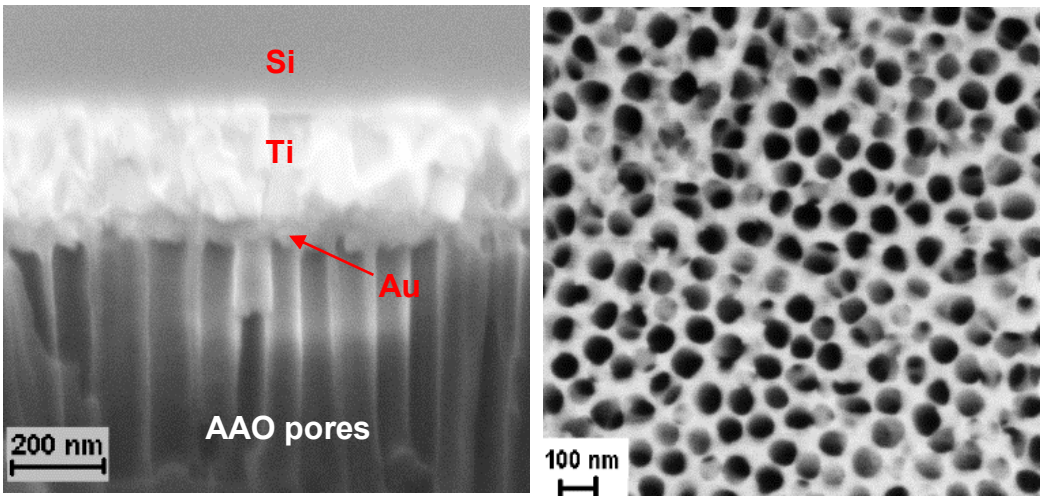


(a) (b)

Figure 2-4: SEM photos of AAO membrane after the 45-minute pore widening step with (a) cross-section and (b) top views.

anodizing at a voltage of 40 V followed by pore-widening for 45 minutes. Figure 2-4(a) of cross-section view clearly shows boundaries of the metallic supportive layers and the AAO membrane. The image demonstrates that the barrier layer was completely removed after 45-minute pore widening. In the Figure 2-4(b), the top view of the self-ordered AAO template shows the nanopores with diameters of approximately 70 nm. The porous morphology is not in a perfectly hexagonal lattice mainly due to quality of the sputtered aluminum film.

## 2.4 Localized Anodization of Sputtered Aluminum on MEAs

### *2.4.1 Anodization Voltages and Currents*

Although AAO membranes have been commonly used as templates to synthesize nanostructured materials, they are traditionally fabricated by anodizing a large-scale aluminum sheets [38-40]. Since our electrodes were of micro-scale sizes, the anodization processes were locally performed on the specified areas. Thus, we investigated the

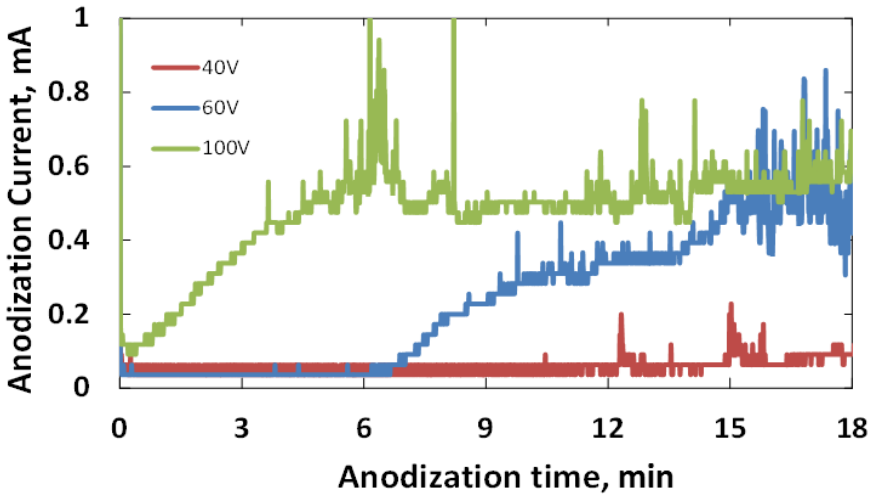


Figure 2-5: Current-time transient of anodization processes at different voltages of 40 V, 60 V and 100 V. The current spikes indicate the detachment of gas bubbles, which accumulated and formed during anodization processes, from the surface of electrodes.

morphology of AAO nanopores formed by localized anodization processes of sputter-deposited aluminum in order to define the fabrication parameters.

Different anodization voltages were applied to investigate their effects on the formation of the nanoporous AAO templates. From our experiments, the anodization rate was estimated to be 45nm/min, and hence the total anodization time for a 900-nm thick aluminum layer would be approximately 18 minutes [37]. Since anodization current and voltage plays vital roles in the formation of the AAO template, we monitored the electrical currents at different voltages of 40, 60, 100 V (Figure 2-5). Typically, there were three stages: reduction of current, steady-state current and increase in current. The reduction of current lasted only a few seconds in the beginning of the processes. In this stage, the entire aluminum layer was quickly oxidized under the electric fields created by the applied voltage to form a compact and uniform alumina layer. Since alumina is intrinsically non-conductive, the current density rapidly dropped as the alumina layer became thicker. In the next stage, the non-uniform electric fields due to inhomogeneity and surface roughness locally assisted

dissolution of the alumina layer to yield the first group of pores at certain points. Once formed, these localized pores continued to grow further through the aluminum layer. The process continued until pores were formed over the entire area and each individual pore reached the supportive gold layer. During this step, the current was steady. In the final stage, the anodization current increased since the gold layer was exposed to the electrolyte and the impedance was reduced. The increase in current was a sign of the completion of the anodization process.

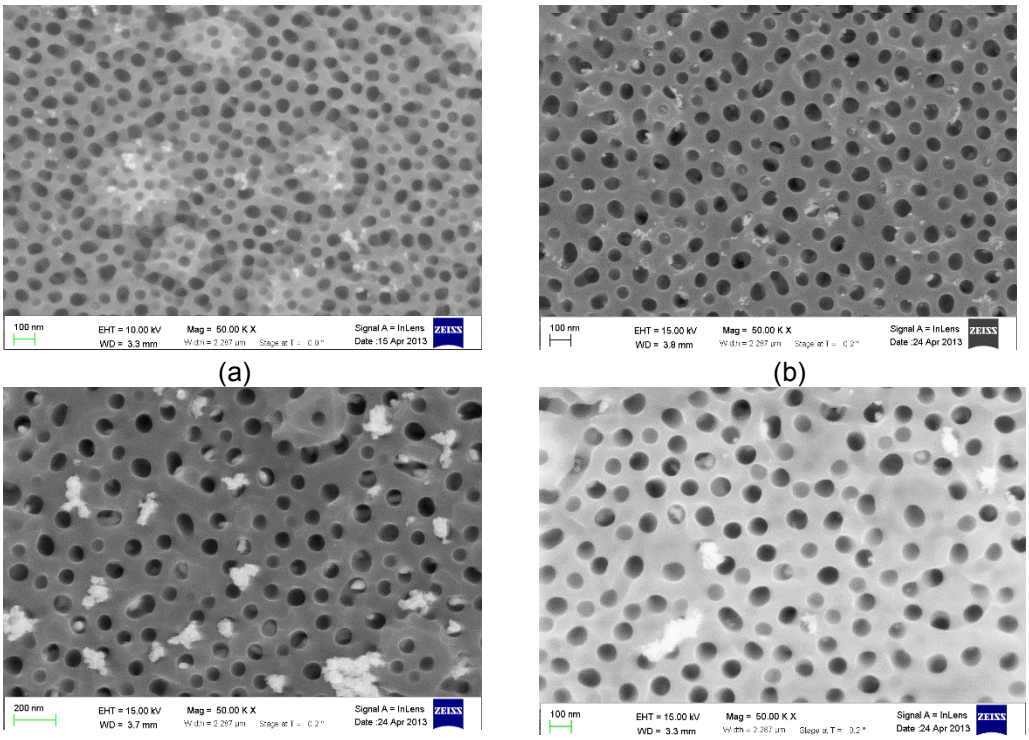


Figure 2-6: SEM photos of AAO membrane after the 45-minute pore widening step with different anodization voltages of (a) 40 V, (b) 60 V, (c) 80 V and (d) 100 V. The diameter of individual pores increase with anodization voltages.

According to Figure 2-5, the steady state of electrical currents when anodizing at 40 V lasted for 15 minutes while the one at 60 V lasted less than 8 minutes. In the case of 100 V, the steady state period was diminished. Obviously, the high applied voltage

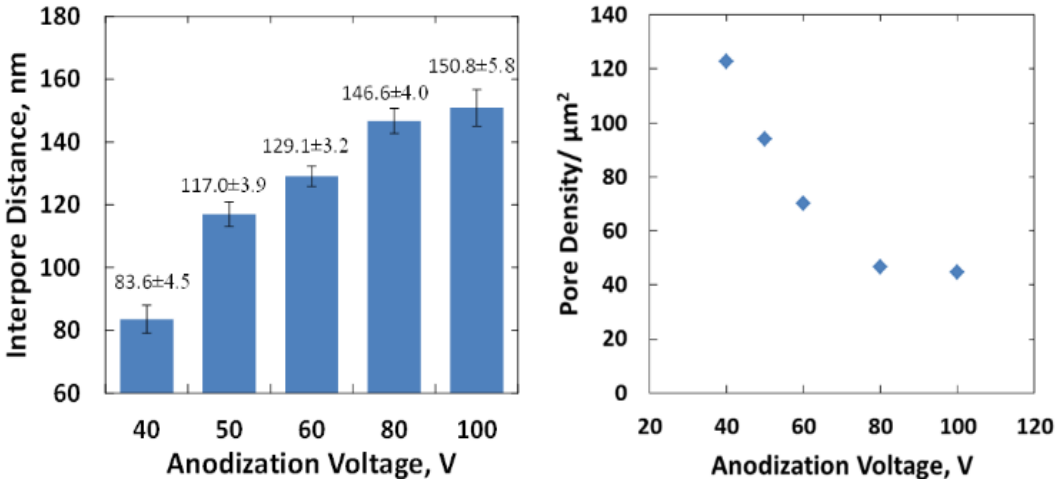


(a) (b)

Figure 2-7: The relationships of (a) inter-pore distance and (b) pore density with the anodization voltages.

generated strong electrical fields which increased the formation rate of the nanopores. Thus, the nanopores grew more non-uniformly and the gold layer was exposed sooner than desired. As a result, the period of steady current was shortened. In addition, the anodization processes generated heat and hydrogen gas bubbles. The gas bubbles were formed and accumulated on the alumina surface before they detached from the surface, which caused electrical current spikes, as shown in Figure 2-5. More evidences are shown later in the section.

Figure 2-6 show SEM photos of the AAO morphologies fabricated at different anodization voltages. These photos were taken with the same magnification. Although the pore widening time was keep similar (45 minutes), these photos illustrate that the higher anodization voltages is, the bigger diameters of these nanopores are. Statistical results in Figure 2-7 show relationship between anodization voltages and the interpore distance and pore density. Five samples were prepared and anodized at different voltages of 40, 50, 60, 80 and 100 V. The samples underwent the same pore-widening process for 40 minutes after anodization. As shown in the Figure 2-7(a), the average pore spacing was

proportional to the applied voltage with a rate of approximately 1.5 nm/V when the voltage was less than 80 V. The observation agreed with ones in literatures that the pore spacing increases with anodization voltage in large aluminum sheets [40, 41]. The inter-pore distance in the sample anodized at 100 V however is similar to the one at 80 V. The relationship between pore density and anodization voltage is shown by Figure 2-7(b). Experiment data again illustrate a subtle difference between anodization voltages of 80 V and 100 V. In general, many factors such as electrolyte solution, electrolyte concentration, temperature, applied voltage, inhomogenities and surface roughness of the aluminum layer affect the pore density. In literatures, increasing electric fields reduces pore densities has been reported with aluminum sheets given that other factors were fixed [40, 41]. In such case of sputtered aluminum, film quality also play a very important role to decide pore density as well as interpore distance.

*2.4.2 Film Quality of Sputtered Aluminum*

As aforementioned, we observed that increasing the applied voltage above a threshold voltage does not provide a lower pore density. At that point, the surface roughness and film quality of the aluminum layer play more significant roles and hence the pore densities are less dependent on the voltages. For example, figure 2-7(b) also indicates such an observation in the pore densities for samples anodized at 80 V and 100V.

Figures 2-8(a) and 4(b) shows the top views of nanoporous structure at a higher magnification when anodizing at 40 V and 100 V, respectively. The SEM micrographs were captured after the same pore-widening process for 40 minutes. The pore sizes of the samples anodized at 40 V and 100 V were 60.5±3.2, 86.9±1.5 nm, respectively. The larger pore sizes achieved with a higher anodization voltage agree with literatures [40, 41]. In addition, Figure 2-8 also illustrates micro bumps on the AAO template. The micro bumps were formed during the sputter-deposited process inevitably due to the fact that the

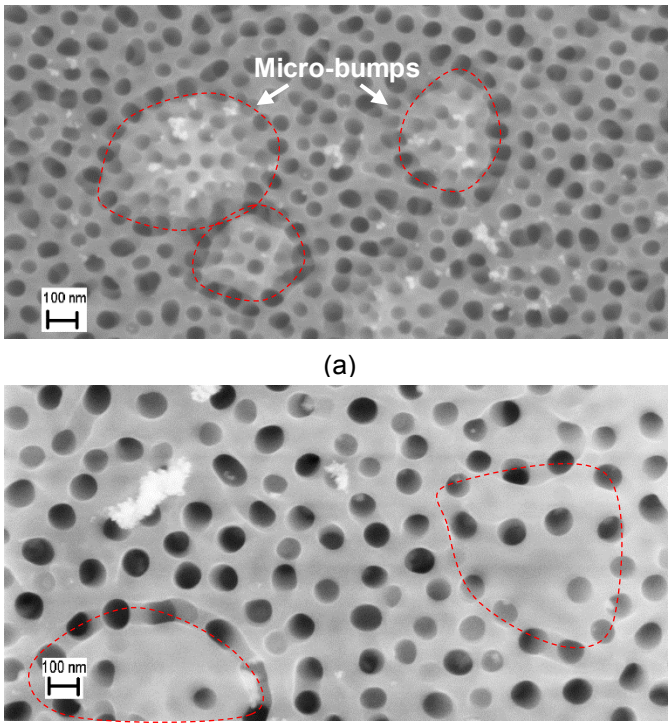


Figure 2-8: SEM photos of nanoporous structures formed at the voltages of (a) 40 V and (b) 100 V. The pore-widening time was 40 minutes. It shows a higher pore density along micro-bump boundaries.

sputtering process typically yields lower-quality thick films as the films are deposited on substrate with atoms following non-uniform electrical fields between the target and the substrate. After anodization, it was found that the nanopores densely formed along the micro-bump boundaries with increased inhomogeneties and surface roughness.

*2.4.3 Adhesion of the AAO Template*

Figure 2-9(a) shows a SEM photo of the top view of a microelectrode array before anodization while (b) depicts the microelectrode area after anodization. The microelectrodes have a size of 50×100 $\mu m^2$. Figure 2-9(a) and (b) display the well-patterned electrodes without the SU-8 passivation layer. The SEM photo of the cross-section view shows clearly boundaries of AAO, $SiO_2$ and Si in Figure 2-9(c) where a gap

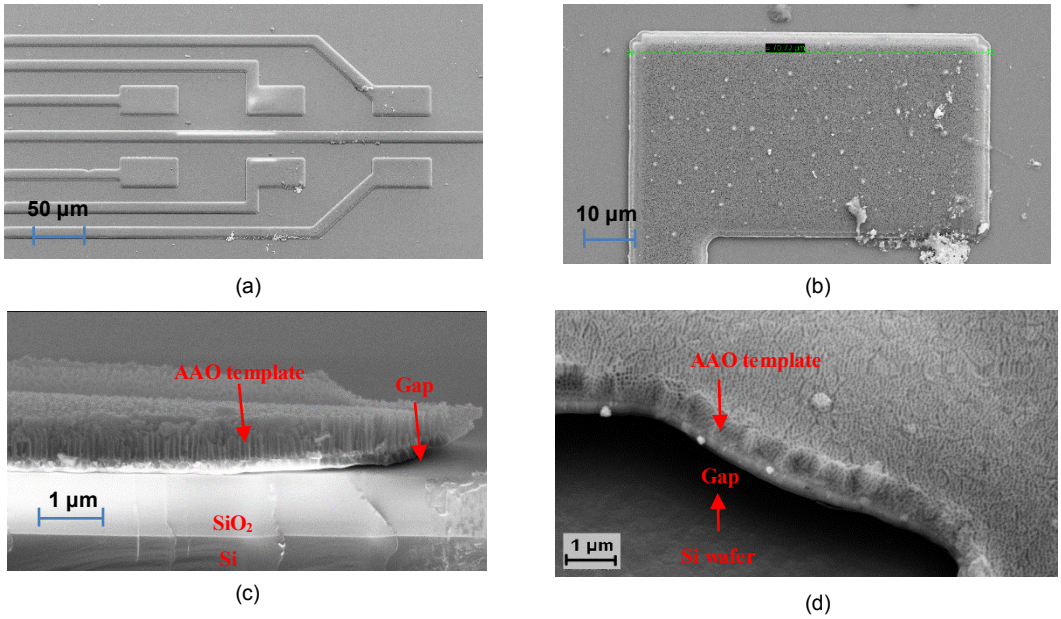


Figure 2-9: SEM photos of (a) top view of microelectrode array without SU-8 passivation layer before anodization; (b) top view of a microelectrode with a size of 50×100μm$^2$ after anodization; (c) cross-section view of the microelectrode after anodization; (d) side view of the edge of the microelectrode after anodization. There is a gap between the AAO template and the silicon wafer due to peeling-off issue.

between the AAO template and $SiO_2$ was identified. The side view in Figure 2-9(d) shows the gap in which the AAO template and metallic layer were curled up from the substrate. The photos in Figs. 2-9(c)–(d) were taken from the samples that were anodized at a voltage of 100 V. The effects from heat and gas bubbles, while anodizing at 100 V, affected adhesion of the alumina membrane and its supportive metallic layer, and consequently stimulated further increase in the anodization current density on the metallic layer. The phenomenon is expected to occur more severely at the edges of electrodes, which elucidates the presence of gaps shown in Figs. 2-9(c)–(d). In conclusion, high applied voltage could damage the structures of the nanoporous AAO template.

2.4.*4 Pore Widening Time*

Figure 2-10 illustrates the relationship of the diameter of pores and pore-widening time. The diameters of pores were measured based on SEM photos. The pore-widening

rate in phosphoric acid (10wt%) was calculated at around 1.34 nm/min. Besides the desired pore sizes, the other factor to be considered when finding the optimal pore-widening time is the condition of barrier layer. The undesired aluminum oxide barrier layer was also removed in pore-widening process. From our experiment, a pore-widening time of 45 minutes was enough to remove completely the barrier layer.

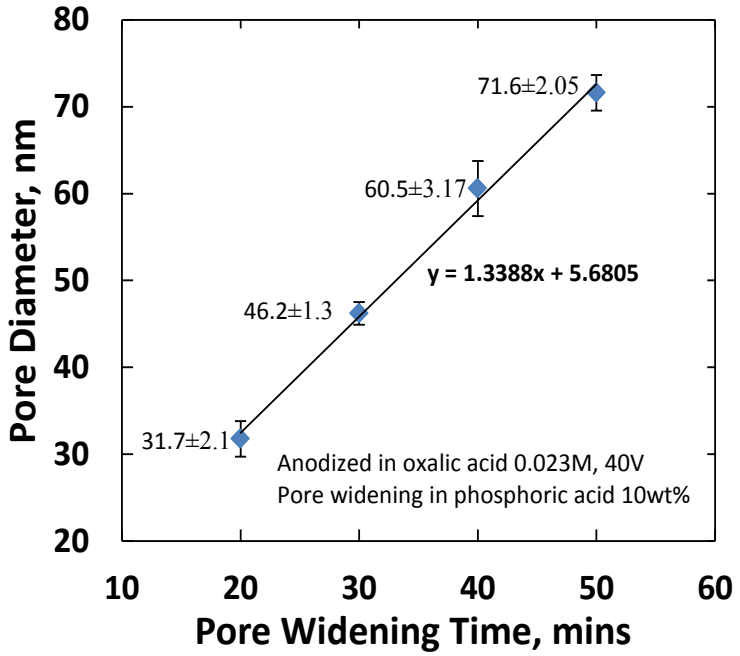


Figure 2-10: The relationship of pore diameter and pore-widening time: AAO membrane was created by anodization in oxalic acid 0.023 M at a voltage of 40V. Pore-widening process rate is found to be 1.33 nm/min.

## 2.5 Conclusions

We carried out a comprehensive fabrication and characterization of the localized anodization of sputtered aluminum film on a MEA. The metallic supportive layers underneath the AAO membrane was found to be a combination of Ti and Au. Micro-bumps appeared due to low quality of the sputtered aluminum film. The existence of micro-bumps play an important role to determine and limit pore density and interpore distance. Although

higher voltage theoretically increase pore-size and interpore distance, we suggested to use voltage lower than 100 V due to current spikes and peeling-off issues. Pore-widening and barrier-removing step is important to dissolve any alumina layer at the bottom of nanopores. We found that 45-minute pore-widening and barrier-removing in phosphoric acid is enough to remove the barrier. The fabrication processes of the AAO template on micro electrode are important to prepare platform for growth of nanostructure materials in next chapters.

# Chapter 3

# CHEMICAL BATH DEPOSITION OF IRIDIUM OXIDE NANORODS FOR NEUROTRANSMITTER SENSORS

## 3.1 Introduction

Researchers have successfully synthesized and characterized $IrO_2$ nanostructures [17, 18, 24, 42]. Nano-scaled $IrO_2$ with a low surface work function of 4.23-eV can be utilized as the catalyst for water splitting or methanol oxidation in fuel cells [18, 22]. The recent success in fabricating one-dimensional nano-sized iridium oxide with high surface areas offers a promising means in improving performance of $IrO_2$-based supercapacitors, implantable biosensors and electrochemical catalysts.

However, the current methods to grow well-aligned $IrO_2$ nanostructures, such as nanorods, required multiple processing steps and sophisticated depositing systems. For instance, the metal organic chemical vapor deposition (MOCVD) technique utilized low-melting iridium precursor (MeCp)Ir(COD) which was difficult to synthesize [23, 43]. The fabrication process had low repeatability because the precursor was oxidized and changed its properties after a few runs [23]. To overcome the barrier, using a physical deposition technique to grow $IrO_2$ nanorods without the need of precursor was suggested [23, 26]. Reactive magnetron sputter was used to deposit $IrO_2$ on high density carbon nanotubes (CNT) to form $IrO_2$/CNT nanocomposites. Although the growth conditions of physical deposition method were controlled, the morphological feature of as-deposited $IrO_2$ was dependent on the density of the CNT template [23]. Moreover, this fabrication process may not be suitable for mass production due to the use of costly iridium oxide targets. Therefore, there is still a need for cost effective methods to synthesize $IrO_2$ nanorods.

In this section, we reported a new method to synthesize $IrO_2$ nanorods by a low-temperature chemical bath process, supported by AAO template membranes. The method

offers several advantages including cost effectiveness, ease to prepare, high throughput and applicability on substrates that require low thermal budget such as polymers. The structural and spectroscopic properties of the nanorods were characterized by scanning electron microscope (SEM), energy dispersive X-ray spectroscopy (EDS) and X-ray diffraction (XRD). Cyclic voltammetry technique was applied to evaluate the charge storage capacity of $IrO_2$ nanorods.

In the later part, we put efforts to grow $IrO_2$ nanorods on the micro-area electrodes. The sensitivity of the sensors featuring with nanorods was experimented with dopamine, one of the most important neurotransmitters in the central nervous system (CNS) of a mammalian.

## 3.2 Materials and Methods

### *3.2.1 Chemicals and Agents*

Chemical bath solution for precipitation process was made with hydrated iridium (IV) chloride $IrCl_4.2H_2O$ (*Air Craft Chemicals Inc*, 99.5%) and potassium bicarbonate (*Alfa Aesar*, 99%). Home-made AAO membrane was fabricated using 25-μm thick aluminum foil (purity 99.5 %, metal basis). The chemicals for anodization and aluminum etching include oxalic acid (*Ricca Chemical*), copper chloride (*Fisher Scientific,* 98%), hydrochloric acid solution (*Banco,* 37%) and phosphoric acid solution (*Em Science,* 85%).

### *3.2.2 Template-Based Growth of $IrO_2$*

An amount of 0.1 gram $IrCl_4.2H_2O$ was dissolved in 40 ml deionized (DI) water. The solution was mixed with a magnetic stirrer for 3 hours before use. Color of the solution changed from light purple to light blue after one day and dark blue eventually. The change in color of the solution indicated the presence of iridium hydroxide and colloidal iridium oxide nanoparticles [39, 44]. According to Meyer et al., the suspension of homogenous $IrO_2$ nanoparticles slowly formed at the room temperature when the solution was exposed

to air for a prolonged period. For the solution we used, the precipitation rate of $IrO_2$ particles was too fast and unable to control if the solution was kept at room temperature more than 48 hours. However, the solution kept at 4°C can be used for multiple times.

The chemical bath solution for precipitation process was prepared by adding an amount of 1.5 mg $K_2CO_3$ to 5 ml of the iridium chloride solution (Appendix C). The role of $K_2CO_3$ in the forming of $IrO_2$ nanorods was considered as that the hydrolysis of $K_2CO_3$ in the aqueous solution generated sufficient hydroxyl anions promoting the formation of $IrO_2$ nanoparticles as follows:

$$K_2CO_3 + H_2O \rightarrow 2K^+ + 2OH^- + CO_2 \uparrow \quad (3\text{-}1)$$

$$IrCl_4 + OH^- \rightarrow IrO_2 + H_2O + Cl^- \quad (3\text{-}2)$$

The chemical bath solution was heated at 95°C during the deposition process. Thermal treatment is a necessary step for potassium bicarbonate to be hydrolyzed as shown in the reaction (3-1). In the meantime, $IrO_2$ colloids formed and aggregated inside the AAO porous membrane following the reaction (3-2). The role of AAO membrane was not only to stabilize $IrO_2$ nanoparticles [24, 44] but also to support the preferential orientation growth of $IrO_2$ nanorods.

*3.2.3 Fabrication Processes*

It is necessary to characterize the growth parameters before deploying with micro-electrodes. We demonstrated the aforementioned template-based fabrication of $IrO_2$ with an AAO template made of an aluminum sheet instead of the one made of sputtered aluminum.

The fabrication step is depicted in Figure 3-1. First, an aluminum sheet with a thickness of 25 μm was anodized in 0.023-M oxalic acid with a constant voltage of 40 V. According to our experiment, the anodization process was carried out at 4°C for 6 hours. The anodization current stayed constant during the process and it dropped quickly at the

end of the process. The nanopores have a thin barrier layer of aluminum oxide at the bottom, as shown in the step 1 in Figure 3-1. Therefore, the sample was immersed in 10wt% phosphoric acid at 25$^{o}$C for 70 minutes in order to remove the undesirable barrier layer (step 2). This step also widened the size of nano-pores, which finally had diameters of around 80-100 nm. In the second step, the backside of the aluminum sheet was etched by aluminum etchant solution (mixed of 0.5-M HCl and 0.3-M $CuCl_2$) in order to create through holes in the AAO membrane. Cross-sectional SEM images were obtained to examine the membrane thickness which was about 10 μm. In the third step, a 400-nm thick copper thin film acting as a support substrate was deposited by the thermal evaporation process on one side of the membrane (step 3). In the experiment, copper was chosen as the metallic supportive layer because it is cost-effective, and high conductivity.

To enforce the sample integrity, a piece of plastic film was attached underneath the copper thin film with a viscous PDMS (polydimethyl-siloxane) layer acting as the adhesive (the step 4 in Figure 3-1). Iridium oxide nanorods then were grown by the chemical bath deposition in the template and the sample was released afterwards by dissolving the AAO membrane in 1-M KOH solution in the steps 5 and 6 in Figure 3-1.

Figure 3-2 shows actual photos of the AAO template made of an aluminum sheet before and after the chemical bath deposition. Since the AAO template is transparent, Figure 3-2(a) indicates copper color underneath the AAO template. After the chemical bath deposition, $IrO_2$ was precipitated inside the AAO membrane with the dark color. It became visible in the Figure 3-2(b).

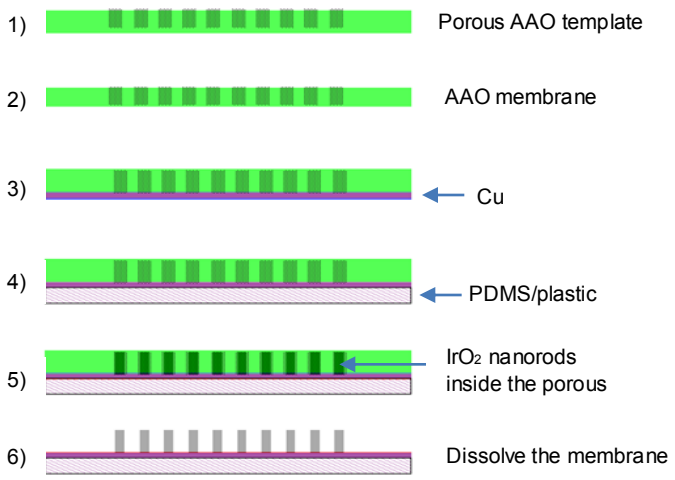


Figure 3-1: Fabrication process: (1) anodize aluminum film to form porous AAO layer; (2) etch away the remaining aluminum to form the AAO membrane; (3) deposit a 400-nm thick Cu thin film; (4) spin-coat a PDMS-based layer; (5) grow $IrO_2$ nanorods inside the AAO template; and (6) dissolve the AAO membrane and release nanorods.

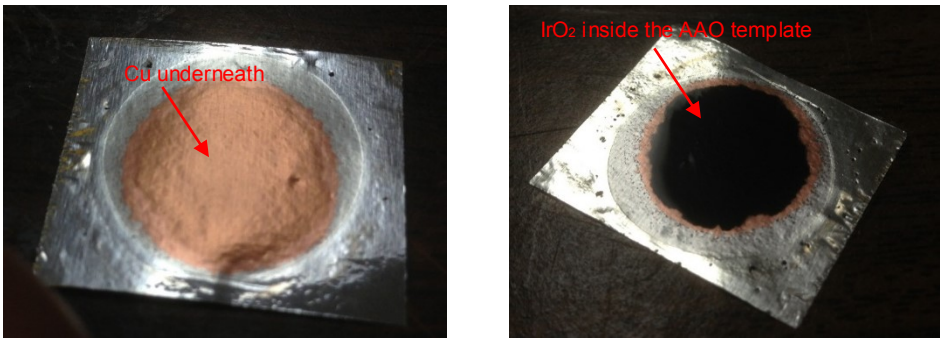


(a) (b)

Figure 3-2: (a) An AAO template with a supportive layer of copper underneath. (b) The membrane after chemical bath deposition of $IrO_2$. Dark color indicates the form of $IrO_2$ inside the template.

### *3.2.4 Experiment Results*

#### 3.2.4.1 Morphology and composition characterization

The presence of $IrO_2$ inside the AAO template is illustrated in Figure 3-3, the cross-section SEM photo. Individual nanorods was formed inside the template following the

nanoporous structures. Figure 3-4 shows nanorods with a length up to 1.02 μm. It should be noted that the nanorods were released from the AAO template under ultra-sonication field, which might break down the nanorods. Therefore, the length of the nanorods in the SEM photo does not illustrate the actual length in the template.

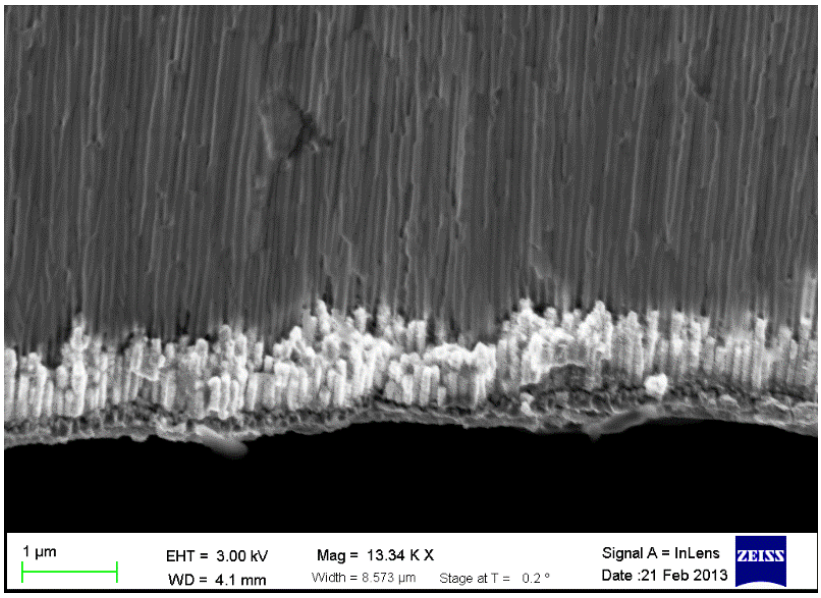


Figure 3-3: SEM photo of $IrO_2$ nanorods inside the AAO template

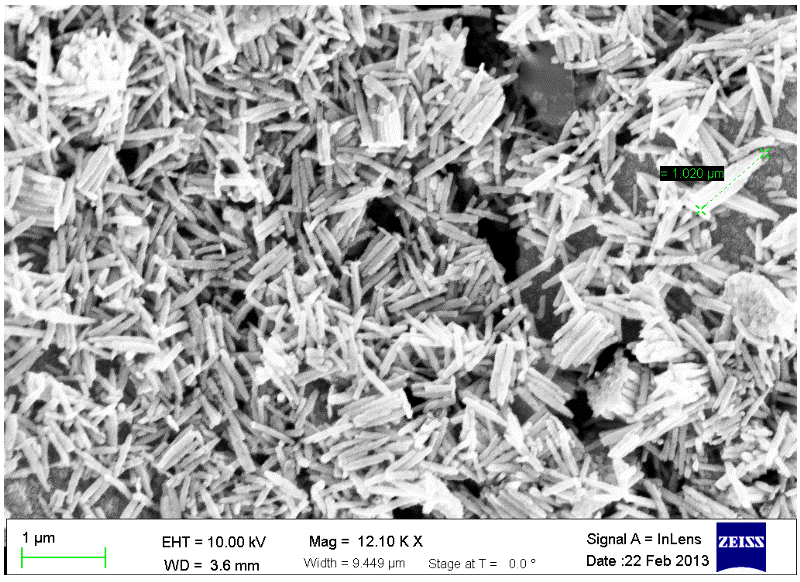


Figure 3-4: SEM photo of $IrO_2$ nanorods released from the AAO template

The morphology feature of $IrO_2$ nanorods on the Cu thin film substrate is shown in Figure 3-5. The top and tilted views in Figures 3-5(a) and (b) exhibited highly dense and well-ordered nanorods. It has been observed that nanorods were formed perpendicular onto the substrate. The nanorod density was estimated as about $3x10^9$ $cm^{-2}$. The diameters of nanorods were in the range of 80−100 nm, which is similar to the diameters of the pores in the AAO template. This implies that the colloidal $IrO_2$ nanoparticles were aggregated inside and self-assembled along the AAO channels. Therefore, the size of nanorods could be adjusted by controlling the diameter of nanopores in the template, which mainly depends on the anodization voltage and pore widening time. To demonstrate this feature, two additional AAO templates have been fabricated at the same anodized conditions but with different pore widening times. Figures 3-5(c) and (d) show the sizes of iridium oxide nanorods made from these two different templates. The diameters of rods are changed from about 79 nm to 196 nm corresponding to the pore widening times from 70 to 110 minutes.

Figure 3-5(e) showed the length of nanorods after 30 minutes of precipitation in the chemical bath solution. The length of nanorods depended on the precipitation time. Five samples were prepared at the same conditions but with different precipitation times in order to investigate nanorod growth rates. The temperature of bath solution was kept at 95$^oC$. SEM has been utilized to measure the lengths of the rods in each sample. The growth rates of the $IrO_2$ nanorods were obtained in Figure 3-6. The rods grew with a nonlinear rate since the abundant compounds and radicals produced following the reactions (1) and (2) accelerated the self-assembly processes of colloidal $IrO_2$ nanoparticles with time.

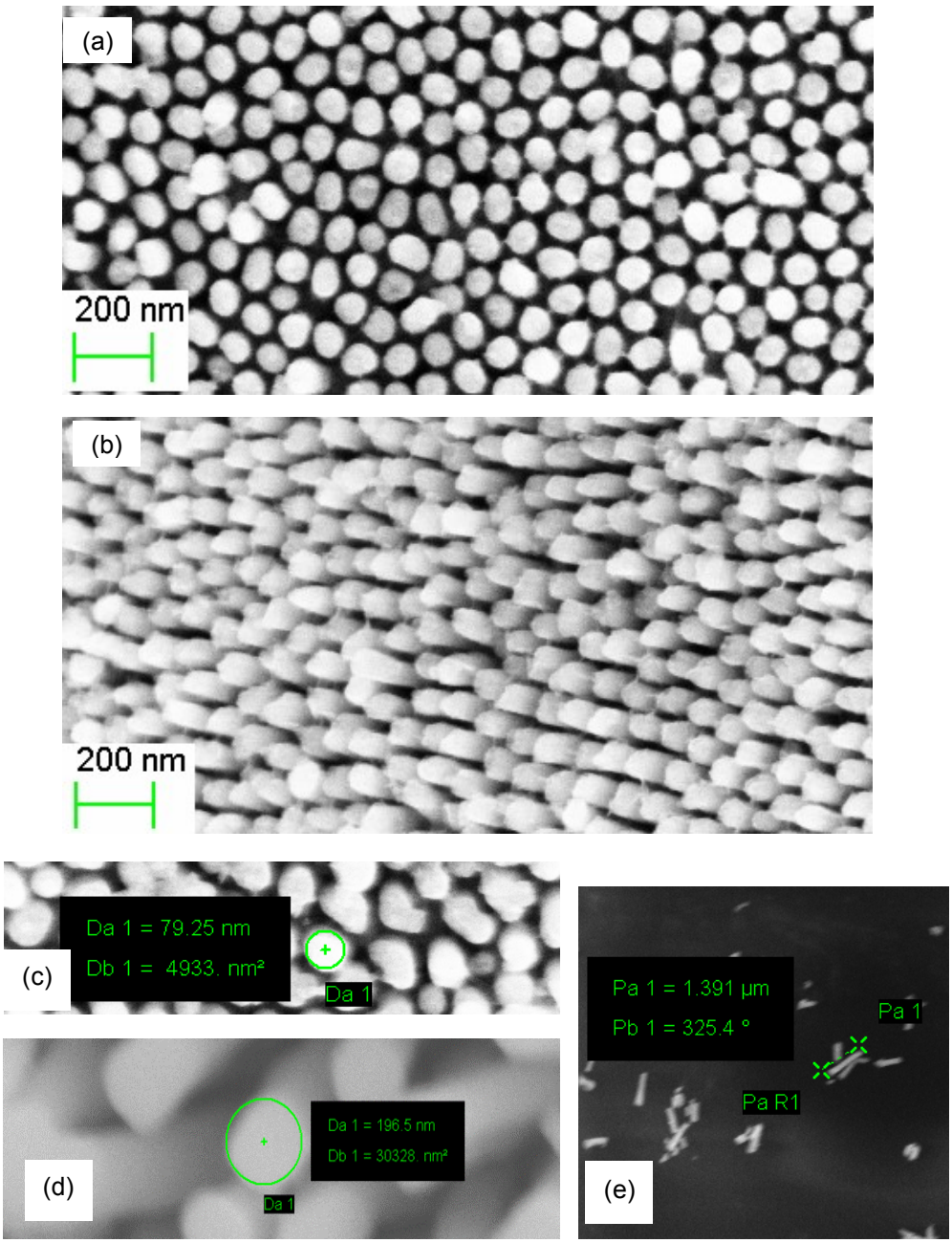


Figure 3-5: SEM photos of $IrO_2$ nanorods after the 30-mintue chemical bath deposition showing: (a) the top and (b) tilted views of high-density and well-aligned nanorods; (c) the diameter of 79 nm and (d) 196 nm of the nanorods made with the 70 and 110-minute pore widening AAO template processes, respectively; and (e) the length of 1391 nm of an exampled nanorod.

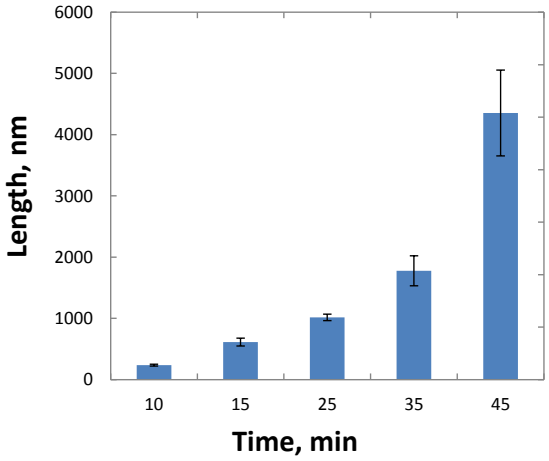


Figure 3-6: Growth rates of precipitated $IrO_2$nanorods in the chemical bath solution at 95°C. Measurements were conducted by SEM.

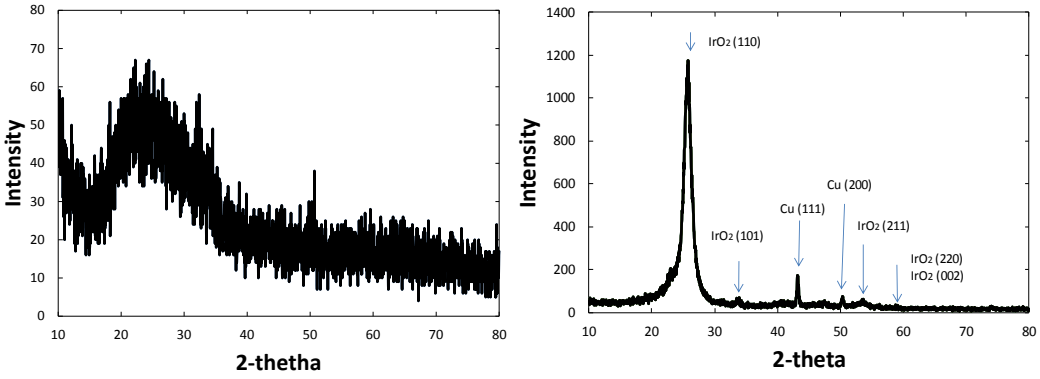


Figure 3-7: XRD analysis: (a) amorphous $IrO_2$ precipitation on a glass substrate compared to (b) precipitated nanorods of $IrO_2$ on a Cu substrateformed with the AAO template.

The result shows that we could achieve $IrO_2$ nanorods with the average length of 4352 nm and diameter of 196 nm, corresponding to aspect ratio of 22, after 45 minutes of precipitation.

3.2.4.2 Microstructural Analysis

Energy dispersive spectrometer (EDS) analysis for the precipitated $IrO_2$ on a Cu substrate was performed at 20 kV to investigate chemical composition of the sample.

Besides the presence of Ir, O and Cu, as expected, the residues of C and Cl molecules were also detected.

X-Ray diffraction (XRD) analysis was performed to study crystal structures. For comparison, Figure 3-7(a) shows the XRD pattern of $IrO_2$ powder precipitating on a glass substrate. The result with no typical peaks indicates the presence of amorphous $IrO_2$. Figure 3-7 (b) shows the XRD measurements of $IrO_2$ nanorods on a copper substrate. Besides the peaks of crystallized copper, it has a sharp peak at 26.3°. Using the Bragg's law, we find the spacing between planes in the atomic lattice is 3.347 Å which matches with the lattice spacing along the $IrO_2$[110] (3.281 Å as reported in [17][17][17][17]). The crystal index of $IrO_2$[110] was further verified by comparing the XRD pattern to the ones in literature [18]. XRD analysis inferred that the crystalized iridium oxide was preferentially oriented along the [110] direction inside the AAO template in our fabrication method.

3.2.4.3 Voltammetric Behavior

Cyclic voltammetry (CV) analysis was carried out to study charge capacity of precipitated nanorods. Three-electrode setup was utilized with a Pt wire counter electrode, a Ag/AgCl standard reference electrode, and a 1×1 $cm^2$ working electrode of $IrO_2$ nanorods. The solution of 1-M KOH supplied electrolytes for the experiment. The CV diagram of $IrO_2$/Cu has a scan rate of 100 $mVs^{-1}$ in the negative region from -1.0 V to 0 V, as shown in Figure 3-8. The presence of $IrO_2$ was manifested by the peak at -0.8 V, according to the literature [26]. The other peak occurred at -0.4 V was due to the absorption of hydroxide on the iridium oxide surface [26]. The CV curve in the potential range between -0.5 V and -0.7 V ($\Delta V$ = 0.2V) with no redox reaction was chosen to estimate the capacitance value, which was calculated by the following equation [26, 45]:

$$C = \frac{\int I dV}{2m \cdot \Delta V \cdot S} \tag{3-3}$$

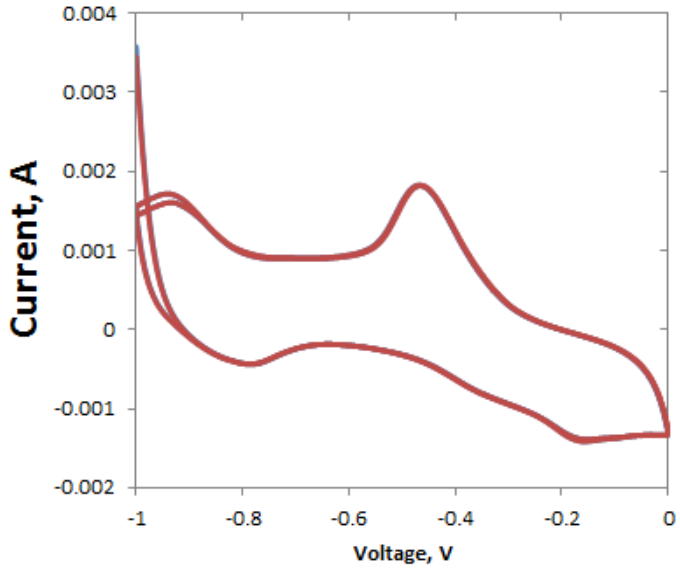


Figure 3-8: Cyclic voltammogram at 100mV/s for $IrO_2$ nanorods on a Cu substrate. Electrolyte solution was 1-M potassium hydroxide solution.

where *m*, *S* and $\int I\,dV$ are the mass of the active material, CV scanning rate and integration of the CV curve, respectively. The mass *m* is determined by the difference in mass of the sample measured before and after the growth of iridium oxide nanorods. As calculated, the $IrO_2$ nanorods unit capacitance was found to be 34.8 $Fg^{-1}$, which is twice the unit capacitance of the electrode made by carbon nanotubes with a diameter of about 40 nm [26].

### 3.3 Miniature Neurotransmitter Sensors Featured with Iridium Oxide Nanorods

Recently, amperometric sensors have been implemented to monitor many neurotransmitter signals in the mammalian CNS such as dopamine, L-glutamate, uric acid, and 3,4-dihydroxyphenylacetic acid [10, 46-48]. The implantable microsensors could assist the study of brain disorders such as Parkinson's disease, Alzheimer's disease, neurodegeneration and addiction [10, 46, 49, 50]. However, the low signal strength resulting from the micro-size of the amperometric sensors remains a challenge. Some

approaches have been developed to improve signal strength and signal-to-noise ratio of the sensor responses.

Optimizing the design of recording systems is one of the most common approaches to improve signal quality [51, 52]. Low-noise and high-gain amplifiers have been chosen to design signal conditioning modules [51]. The small output signals of the sensors requires to use multiple amplifier stages. However, the number of amplifier stages and amplifier gains of the recording circuit are constrained due to other criteria such as complexity, stability, power consumption, and noise figure. In other words, it is optimal to design a system with fewer amplifiers and lower gain. Thus, a method to improve micro-sensor signal levels without affecting the size of the sensor is required.

In this section, we introduced fabrication processes to grow $IrO_2$ nanorods directly on a silicon wafer. The micro-sensors were patterned by semiconductor fabrication processes before the AAO nano-template was applied in an anodization process. The AAO nano-template was necessary for $IrO_2$ growth in a chemical bath deposition process. The method yielded $IrO_2$ nanorods on the surfaces of micro-electrodes within a size of 50×100 $\mu m^2$ with mass-producibility and high reproducibility.

*3.3.1 Fabrication Process*

The microsensors featured with the AAO nano-template were fabricated according to the processes described in Chapter 2. Localized anodization processes were conducted to generate nanoporous AAO template on micro-areas, as shown in Figure 3-9 (a). Chemical bath deposition was thus utilized to grow the $IrO_2$ nanorods with the support of the aforementioned nano-template. The processes was following the recipe described in previous section (Figure 3-9(b)). The membrane then was dissolve in the alkaline solution and free-standing nanorods were formed as shown in Figure 3-9(c). Finally, the individual

sensors were tailored-to-size using laser micro-machining (Oxford Lasers). Figure 3-10 illustrate a 3-D prototype of the micro-electrodes featured with $IrO_2$ nanorods.

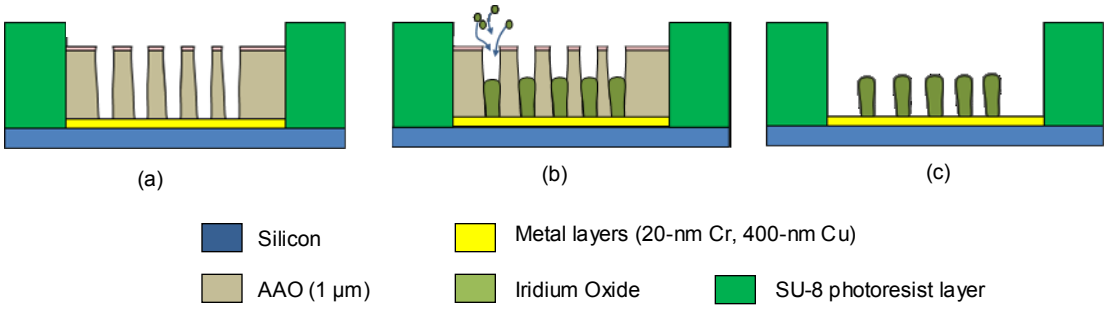


Figure 3-9: (a) Formed porous AAO nanotemplate in localized anodization process. (b) Chemical bath grown $IrO_2$ nanorods inside the nanotemplate. (c) Freestanding $IrO_2$ nanorods after the template is dissolved.

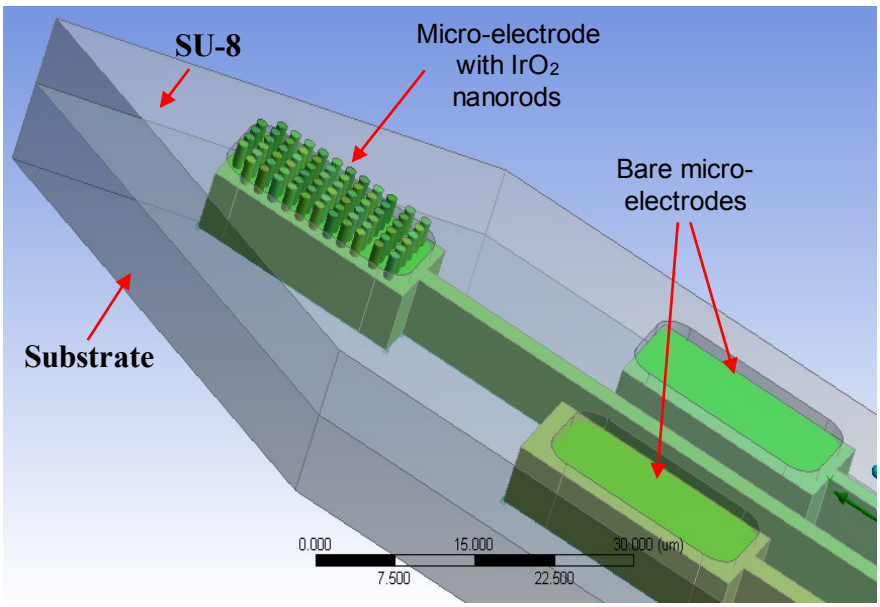


Figure 3-10: An 3-D prototype of micro-electrodes featured with $IrO_2$ nanorods to improve surface areas.

*3.3.2 Morphologies Characterization*

The morphologies of $IrO_2$ nanorods grown on a micro-electrode were investigated using SEM. Figure 3-11(a) illustrates the top-view of a micro-electrode with a size of 50×100 $\mu m^2$. The sensing area of the micro-electrode was confined by the SU-8 insulation layers. Nanorod structures grown in 30 and 40 minutes were illustrated in Figure 3-11(b) and (c). The diameter of each nanorods was in a range of 80−100 nm, which was similar to the inner diameter of the AAO nano-porous structure. The nanorods after a 40-minute

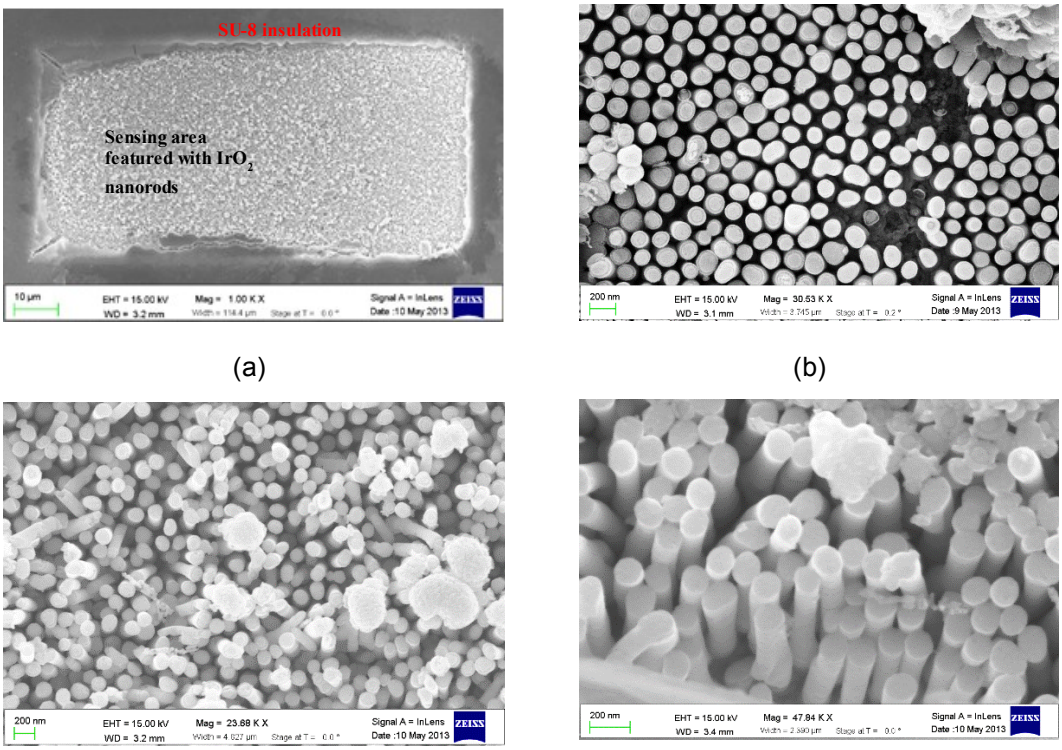


Figure 3-11: SEM images of (a) top-view of a microelectrode with a size of 50×100 $\mu m^2$. The sensing area featured with $IrO_2$ nanorods was confined by the SU-8 insulation layer; (b) top-view of $IrO_2$ nanorods grown after 30-minute chemical bath deposition; (c) top-view of $IrO_2$ nanorods grown after 45-miute chemical bath deposition; (c) tilt-view with high magnification of nanorods grown on the surface of the electrode. Nanorods have diameters of 80−110 nm and lengths of 200−300 nm.

chemical bath deposition were longer and denser than those of the 30-minute deposition. The support of the AAO nano-porous template was important to guarantee the nanorod structures. Figure 3-11(d) shows the higher magnification photo of individual nanorods, which were directly grown and connected to the surface of the micro-electrodes. The height

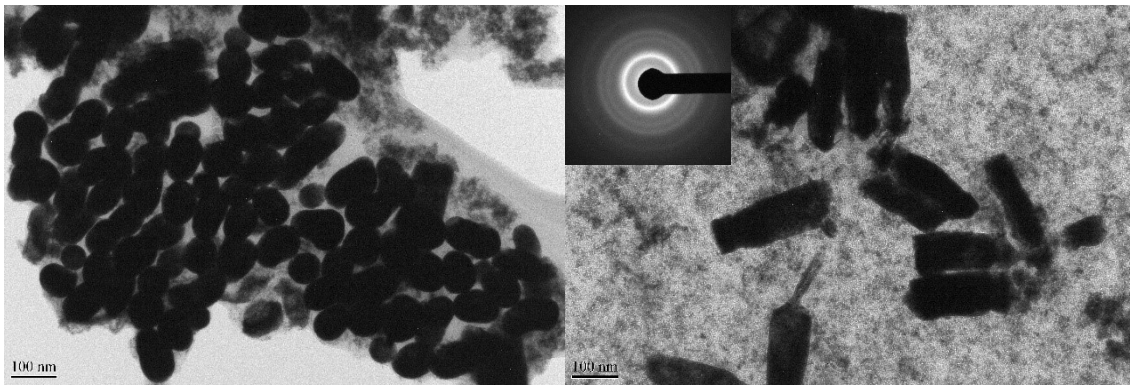


(a) (b)

Figure 3-12: TEM micrograph of nanorods: (a) nanorods which blocked electron beam of the TEM appear in black color; (b) nanorods have a diameter of 80 nm and length of 200 nm. Diffraction imaging indicates that $IrO_2$ nanorods have small polycrystalline structures.

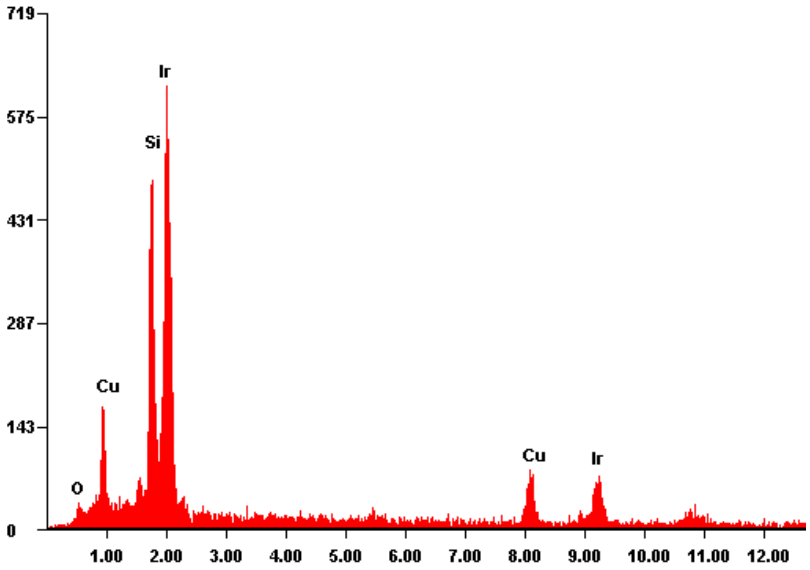


Figure 3-13: Energy dispersion X-ray spectroscopy analysis of $IrO_2$ nanorods on a microelectrode.

of the nanorods was estimated to be 200–300 nm. The density of the nanorods on the micro-electrodes was also similar to the pore density of the AAO nano-porous template.

Characterization of the nanorods was examined by transmission electron microscopy (TEM). The $IrO_2$ nanorods were released from the silicon substrate in a mechanical preparation processes. The nanorods were then mixed with DI water to reduce concentration in a centrifuge tube. Ultra-sonication field for 30 minutes was applied to thoroughly mix the solution. TEM sample holder made of a copper grid was utilized to collect nanorods from the centrifuge tube. The sample was dried before investigating using a Hitachi H-9500 high-resolution TEM. Figure 3-12(a) displays nanorods on the copper grid. Since the rods blocked the electron beam of the TEM, they appeared black in color. Figure 3-12(b) depicts individual nanorods with a diameter of approximately 80 nm and length of 200 nm. The TEM diffraction image of the nanorods shown on the upper corner of Figure 3-12(b) indicated that the $IrO_2$ nanorods have small polycrystalline structures.

Figure 3-13 shows analysis of $IrO_2$ nanorods on the microelectrode using energy dispersive spectroscopy (EDS). The measurement was performed when the accelerating voltage of the SEM was 20kV. The presences of Ir, O, Si and Cu atoms are illustrated with obvious peaks (Figure 3-13). Characterization by EDS showed the percentages of these materials were 66.76%, 2.3%, 16.22%, and 14.73%, respectively. Aluminum was not found due to complete dissolution of the AAO membrane. The EDS results showed iridium was the main component, while silicon and copper were found due to their existence in the substrate.

*3.3.3 Amperometric Sensors Based-on $IrO_2$ Nanorods*

Bench-top experiments were conducted in the laboratory. The performance of the micro sensors was calibrated using a beaker containing 40-ml phosphate buffered saline (PBS) solution. The beaker was kept at 37°C using a water bath to mimic conditions inside

the human body. Dopamine was chosen to test the performance of the sensors, since it is an important and widely present neurotransmitter in the mammalian CNS. The detection of the dopamine can be examined by a voltammetry electroanalytical method in which a constant voltage is applied and current response is monitored. A commercial potentiostat (*Pinnacle, Inc.*) was utilized to measure output signals. A constant voltage of 0.7 V was applied between the working electrode featured with $IrO_2$ nanorods and a standard Ag/AgCl reference electrode. Dopamine was incrementally added to the solution in order to raise the concentration by 15 μM every 6 minutes. A magnetic rod in the beaker was utilized to mix the solution.

The sensor responses are shown in Figure 3-14. Response time of the sensor was defined as the transient time required for output currents to approach 90% of stable responses after dopamine is added. The response time depends on many factors such as impedance of electrode/electrolyte interface, sensor dimensions, the volume of the testing

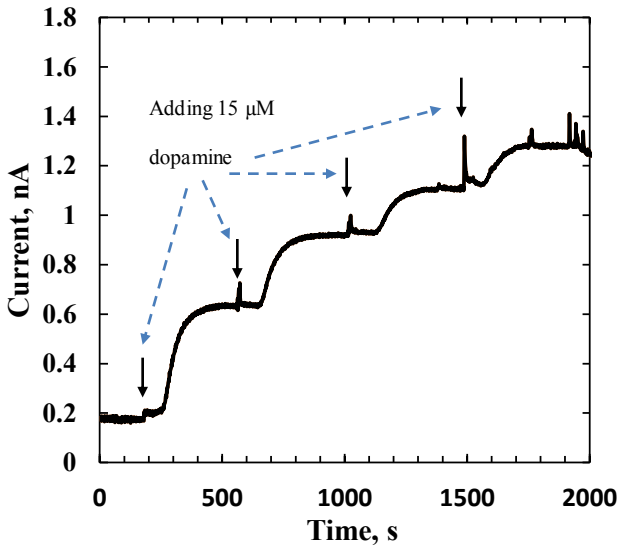


Figure 3-14: Sensor response to incremental addition of dopamine to increase concentration by 15 μM every 6 minutes. Sensor sensitivity of 18 pA/μM was recorded.

solution and the mean to mix solution. According to Figure 3-14, the response time of the sensor was 159–206 seconds. The sensitivity of the microsensor was measured of 18 pA/μM. Figure 3-14 also illustrates that the sensor response after the first incremental increase was greater than the last incremental increase. The issue of nonlinear response occurred due to saturation corresponding to high concentration of dopamine when the last drop was added.

## 3.4 Conclusions

A new precipitation method to grow high-density and well-aligned $IrO_2$ nanorods using solution precipitation method inside AAO membrane was proposed and implemented. The characterization by SEM, EDS and XRD showed that the AAO template assisted the formation of crystalline $IrO_2$ nanorods. Higher unit capacitance value due to the high contact surface area in nanorods was validated by the CV technique. It is possible to implement the nanorods modified surfaces for supercapacitors or sensor applications owing to the increase of active surface area while preserving the material advantages of $IrO_2$. The performance of the simpler, cost effective and fast deposited microsensors featured with $IrO_2$ nanorods was demonstrated with dopamine, one of the major electroactive neurotransmitters in the brain. The fabrication method could also be applied to different kinds of neurotransmitter micro-sensors with functionalized surfaces.

# Chapter 4

# ELECTRODEPOSITION OF IRIDIUM OXIDE NANOTUBES ON MICROELECTRODES FOR pH SENSORS

## 4.1 Introduction

It is important to monitor pH values in various biological and medical processes. These processes include, but not limited to, enzymatic reactions [53-55], exchange of nutrients and waste products in living organisms [56, 57], biological studies of cells [58, 59], medical drug synthesis [60, 61], and bioanalysis of drugs [62, 63]. To date, various types of pH sensors including ion-sensitive field-effect transistor (iSFET) pH sensors [59, 64], hydrogel-based pH sensors [65], optical pH sensors [66, 67], and potentiometric pH electrodes have been developed and utilized according to different requirements in applications. Among all sensors, the potentiometric pH electrodes have demonstrated great potentials for use in in vivo implants and in vitro analysis because of their simplicity, cost-effectiveness, miniaturization capabilities and simpler fabrication processes [68, 69].

The potentiometric pH electrodes are typically fabricated using micro-electro-mechanical system (MEMS) technologies and coated with pH-sensing solid-state oxide materials such as IrOx, $RuO_2$, $PtO_2$, $OsO_2$, $Ta_2O_5$ [1, 20, 70, 71]. Current technologies allow fabricating pH electrodes in micro-scales, which opens the possibility to develop micro pH electrodes. The micro pH sensors have potential advantages of lower power consumption, sensitive analyte detection, reduced sample quantities and multiple-point measurements [72, 73]. However, signal quality of miniature electrochemical sensors remains to be an issue [74, 75]. Since the micro pH electrodes with small sensing sites present large electrode/electrolyte interface impedances and have effectively less amount of sensing materials, they have lower sensitivities that also decay in long-term experiments [74, 76, 77].

Surface modification with nanostructured materials to improve signal quality in micro-electrochemical sensors has provided an attractive option to enhance the sensor performance. The large reaction surface areas of nanostructures can compensate for the decrease in the sensing electrode footprints. Many methods have been proposed to form nanostructured materials such as chemical vapor deposition [78], chemical bath deposition [79], atomic layer deposition [80] and template-based growth [31, 81, 82]. Among all methods, template-based synthesis offers a versatile and flexible means to grow nanostructured materials on a surface. However, applying the current template method onto a micro-scale electrode faces technical challenges.

In this section, we reported a novel micro pH sensor comprised of iridium oxide ($IrO_x$) nanotubes. $IrO_x$, the composition of $Ir_2O_3$ and $IrO_2$ was chosen for the sensing material owing to its wide-pH sensing range, biocompatibility, and ease of fabrication [72]. The $IrO_x$ nanotubes were grown by electrodeposition processes into a supportive anodic aluminum oxide (AAO) template. The sacrificial AAO template was fabricated on a wafer in a cost-effective and high throughput anodization process which can be applied on various types of substrates. All fabrication steps do not require high temperature environments or expensive equipment. In this paper, the micro pH sensors featured with the $IrO_x$ nanotubes produce high pH sensitivity, good stability, and fast response times. The implementation of $IrO_x$ nanostructure is thus proven to be a great choice for miniature pH sensors.

## 4.2 Fabrication and Methods

### *4.2.1 Sensor Preparation*

The sensor fabrication processes have been described in the Figure 2-1, Chapter 2. The step (g) in the Figure 2-1 is the process of electrodeposition. It should be noted that, the electrodeposition yielded a composition of both $Ir_2O_3$ and $IrO_2$. Therefore, iridium oxide

in this chapter will be denoted as $IrO_x$. The growth of nanotubes is illustrated in the Figure 4-1. Firstly, the cross-section of a micro-electrode with an AAO template was prepared (Figure 4-1(a)). Secondly, $IrO_x$ was electro-deposited inside the AAO template (Figure 4-1(b)). Over electrode deposition may happen depend on the electrolyte concentration and electrodeposition rates. We will discuss the phenomenon in the next section. Finally, the AAO template is removed to release free-standing $IrO_x$ nanotubes on the micro-electrode (Figure 4-1(c)).

*4.2.2 Electrodeposition of $IrO_x$ Nanotubes*

Up to now, there are many different deposition methods to grow iridium oxide thin film such as sputtering [83], electrodeposition [84], thermal oxidation [85], and sol-gel deposition processes [86]. The synthesis of iridium oxide nanotubes in our work was adopted from electrodeposition of $IrO_x$ into the AAO template because it is a cost-effective and quick deposition method. The electrolyte solution was made following the Yamanaka recipe [84]. An amount of 0.075-g iridium (IV) chloride salt (*ArtCraft Chemicals Inc.*) was dissolved in 50-ml deionized water. The solution was stirred for 30 minutes before adding 0.5 ml of 30% $H_2O_2$ and 0.5 g $C_2H_2O_4.2H_2O$. After mixing, the pH of the solution was adjusted to around 10.5 by adding potassium bicarbonate powder (*Alfa Aesar*). The solution was kept in 4$^oC$ for 2 days for stabilization [84].

Cyclic voltammetry deposition is commonly used for the electrodeposition. A two-electrode electrochemical cell with a platinum rod as the cathode was utilized. The deposition was controlled by a *CHI7001D* galvanostat (*CHI Instruments, Inc.*). The potential was varied in a range from 0.0 to 1.0 V with a scanning rate of 50 mV/s. The process was repeated over multiple cycles. Figure 4-2 shows the current-potential (I-V) curves after 20, 50, 80, 100 and 130 deposition cycles. There are one cathodic peak at 0.32 V and two anodic peaks at 0.71 V and 0.28 V. According to Figure 4-2, the I-V curves

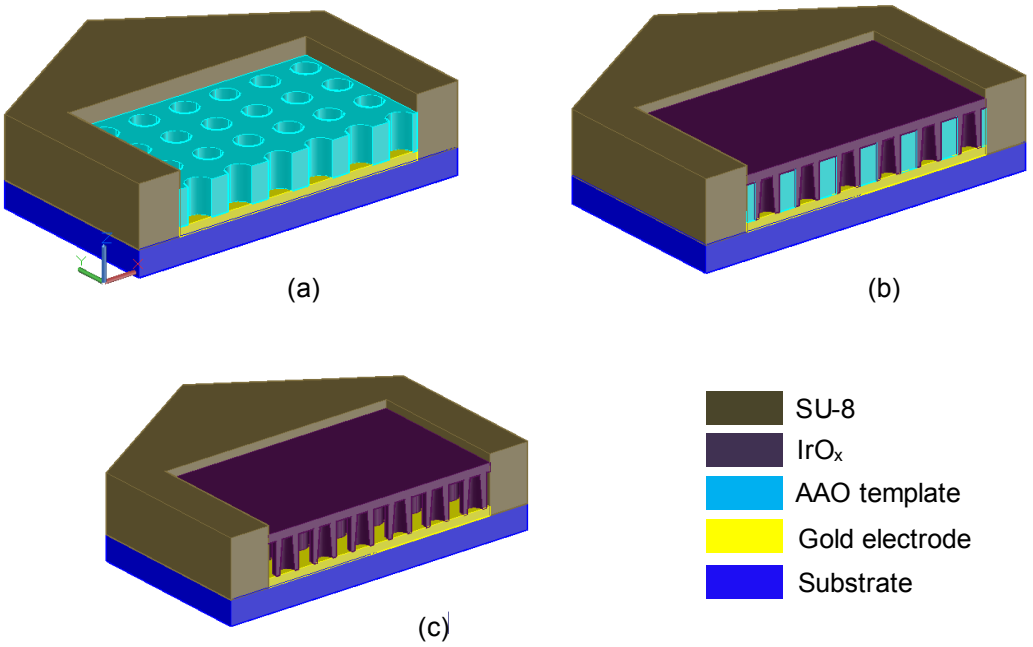


Figure 4-1: (a) A micro-electrode with an AAO template on top; (b) Electrodeposition of $IrO_x$ inside the AAO template. Over-electrodeposition phenomenon is also illustrated with a layer of $IrO_x$ connecting the top part of all nanotubes. (c) The micro-electrode with $IrO_x$ nanotubes after dissolving the AAO template.

with more deposition cycles were broader accompanied with higher current values, indicating that more iridium oxide was deposited. The I-V curves are similar to the work conducted by Mafakheri *et al.*, in which, however, the iridium oxide was grown into a large-scale poly-carbonate membrane [87], unlike our micro-scale AAO membrane on a limited electrode area.

Although the electrodeposition could yield both nanorods and nanotubes, our goal is to fabricate nanotubular structure to obtain higher surface-to-volume ratio. Thus, the use of cyclic voltammetry deposition by sweeping voltages was necessary. Initializing with low voltages associated with low deposition rates formed a thin layer of $IrO_x$ at the bottom of each AAO pore. This was followed by high anodization voltages, which allowed fast deposition of $IrO_x$ along the walls of the AAO pores. Although the fast deposition

dominated, the period for slow deposition was necessary to eliminate flaws such as weak structures and improper formations of the tubular structure during deposition.

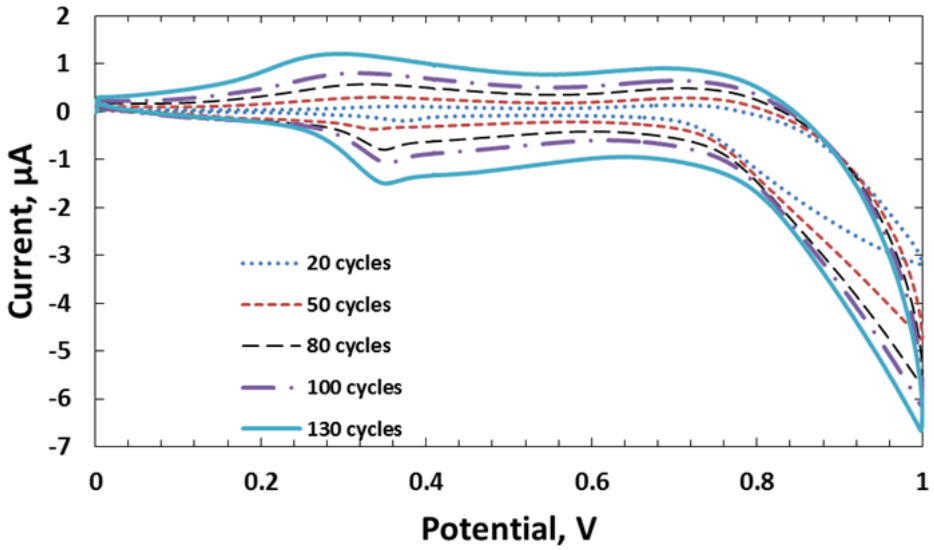


Figure 4-2: Cyclic voltammetry deposition of $IrO_x$ using potential cycling with various deposition cycles.

Figure 4-3 shows the top views of microelectrodes obtained with different deposition cycles before dissolving the templates. The AAO templates were fabricated at a 60-V anodization voltage for 18 minutes and with a 45-minute pore widening, afterwards. The deposition was conducted with the same potential cycling between 0.0 and 1.0 V as mentioned before. With 20 cycles of electrodeposition, the sample still showed the porous structure of the template. The 80-cycle electrodeposited sample had pores with smaller inner diameters. The figure showed the formation of iridium oxide inside the AAO pores. Figure 4-3(c) shows the top surface without visible pores after 130 depositing cycles. Our investigation indicated that nanopores became concealed under a layer of $IrO_x$ thin film when the sample was over deposited. The consequence of such over-deposition will be discussed later.

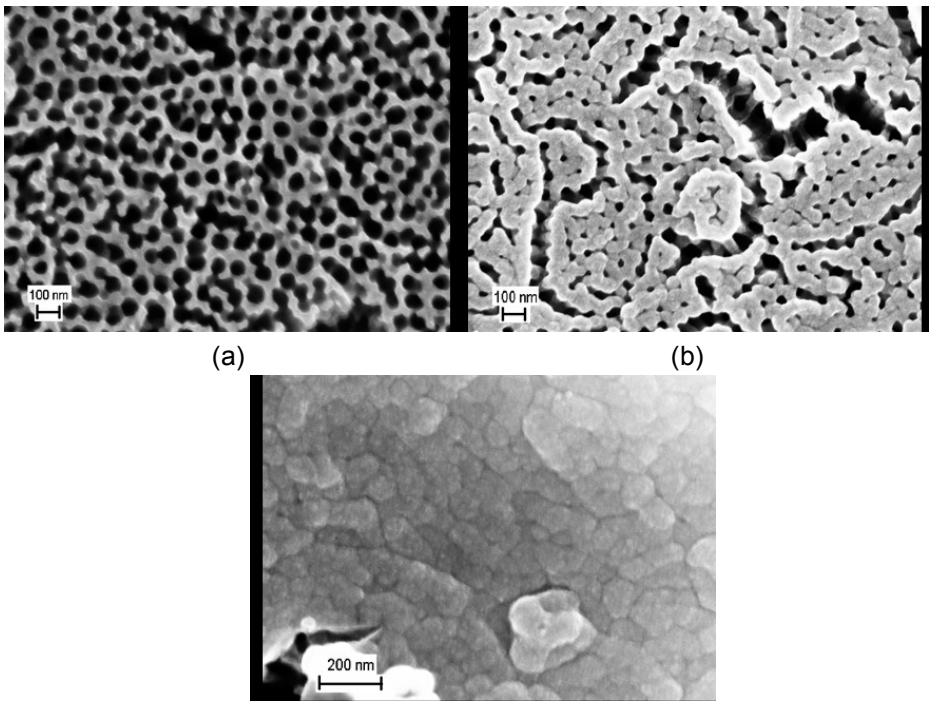


(a) (b)

(c)

Figure 4-3: SEM photos of the top surface of microelectrodes with different deposition cycles of (a) 20, (b) 80, and (c) 130 cycles.

In the final step, the microelectrodes were dipped into a 0.1M KOH solution for 2 hours to chemically dissolve the AAO template and reveal the free-standing $IrO_x$ nanotubes. The sample was then analyzed using energy dispersive X-ray spectrometer (EDS). The materials were Ir, O, Si, Au, Ti and Al with their percentages of, analyzed by EDS, 30.3, 10.4, 34.4, 24.5, 13.0 and 4.9%, respectively. Low aluminum percentage confirmed the complement of the processes.

Figure 4-3 shows SEM photos of a microelectrode with free-standing $IrO_x$ nanotubes. The microelectrode depicted in Figure 4-3(a) has a size of 50×100 $\mu m^2$. Higher magnification SEM photo in Figure 4-3(b) clearly shows the structure of the nanotubes on the surface. To show the nanotubular structure, the surface of the electrode was scratched and SEM photo was taken (Figure 4-3(c)). The nanotubes have outer diameters in a range

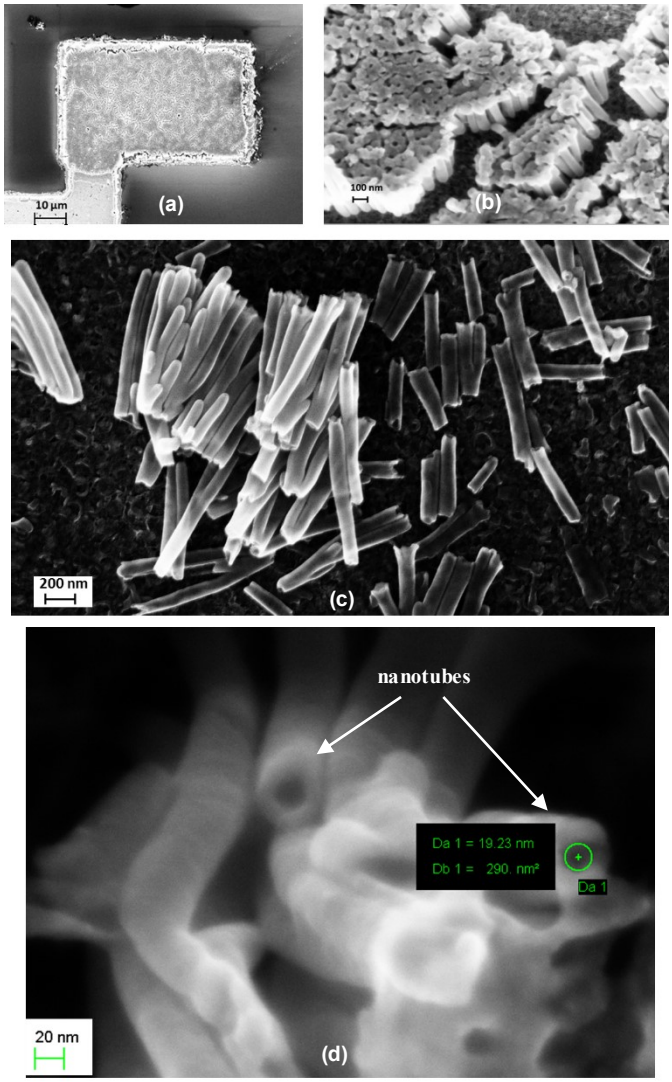


Figure 4-4: SEM photos of (a) the top surface of the microelectrode with a size of 50×100 µm$^2$ covered with $IrO_x$ nanotubes; (b) free-standing $IrO_x$ nanotubes on top of the microelectrode; (c) $IrO_x$ nanotubes, scratched out of the microelectrode surface, having outer diameters in the range of 80–110 nm and an average length of approximately 1 µm; (d) individual nanotubes with an inner diameter of 14–19 nm

of 80–110 nm and a length of approximately 1 µm, corresponding to the thickness of the template. The tubular shapes are revealed by arrows in Figure 4-3(d). They show hollow structure at the center of the tubes with an inner diameter of 14–19 nm.

In order to reveal the tubular structure, a transmission electron microscope (TEM) micrograph was taken. The nanotubes was released from its substrate in mechanical preparation processes and mixed with DI waters. A TEM sample holder made by copper grid was dipped into the solution to collect nanotubes. Figure 4-4 displays the TEM micrograph of two nanotubes. We observed two walls (darker color) of the nanotubes. The hollow structure was transparent under transmission electron beam. The micrograph also illustrates nanotubes with outer diameters in a range of 85–100 nm. Figure 4-4 also implicates the IrOx nanotubes have structures replicating the one of AAO nanopores.

## 4.3 Experiments and Results

Multiple micro sensors featured with $IrO_x$ nanotubes were prepared by cyclic electrodepositing iridium oxide for 100 cycles. The pH-sensing properties of the microelectrodes were characterized in different buffer solutions. Droplets of buffer solution were applied on the microelectrode. A standard silver/silver chloride reference electrode

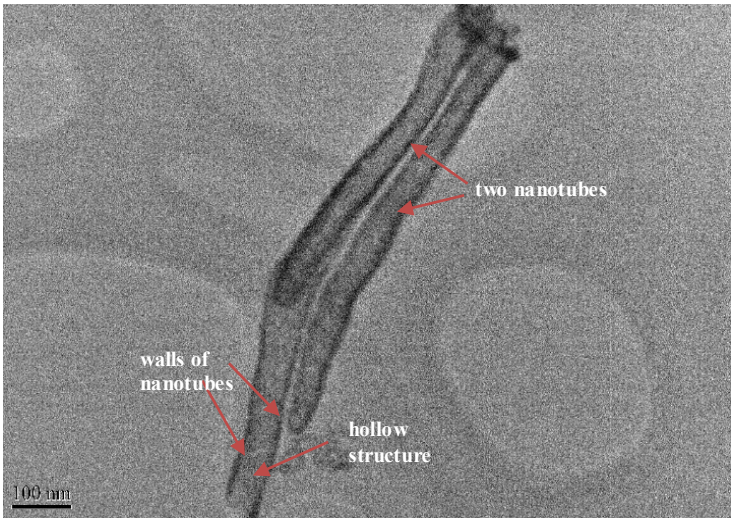


Figure 4-5: A TEM micrograph of two nanotubes. The two walls of each nanotube with highly dense material that blocked transmission electrons are displayed darker than the hollow structure at the center of the nanotube. The nanotubes have structures following the structures of AAO nanopores.

was utilized in the characterization. Voltage responses of the sensors were measured with a customer-built circuit connected to a data acquisition card and the signals were recorded with a LabVIEW-based recording program. The microelectrodes were rinsed in DI water and air-dried between experiments.

*4.3.1 Sensitivity and Repeatability*

The sensitivity of the microelectrodes was calibrated with buffer solutions with pH of 2, 4, 5, 7, 9, and 10 (*Metler-Toledo*). Each experiment lasted less than 100 seconds. The voltage responses versus the pH buffer solutions were shown in Figure 4-5. The sensitivity was calculated of 74.2 mV/pH, which is higher than the sensitivity of sol-gel based pH sensors (51 mV/pH) [72]. The voltage response acted quickly and stayed constant with subtle fluctuations. Voltage drifts of 12.0, 3.0, 2.0, 3.0, 5.0, and 3.0 mV, respectively, for solutions with pH of 2, 4, 5, 7, 9, and 10 were observed during the test periods. The maximal voltage drifts of less than 12 mV, corresponding to a pH value of 0.16, was lower than the voltage drifts reported with $IrO_x$ thin-film [72, 86].

The mechanism of pH-sensing properties of iridium oxide has been mentioned by Bezbaruah *et al.* [88]. It was referred that anodic electrodeposition generated majority of hydrated iridium oxide [88]. The half-cell redox reaction of hydrated iridium oxide was followed:

$$2[IrO_2(OH)_2.2H_2O]^{2-} + 3H^+ + 2e^- \leftrightarrow [Ir_2O_3(OH)_3.3H_2O]^{3-} + 3H_2O \qquad (4\text{-}1)$$

The reaction indicated that only 2 electrons transfer for every 3 protons ($H^+$); hence, the maximum slope of a Nernst equation could be obtained as high as 88 mV/pH [88]. The advanced sensitivities compared to the regular one of 51 mV/pH were known as super-

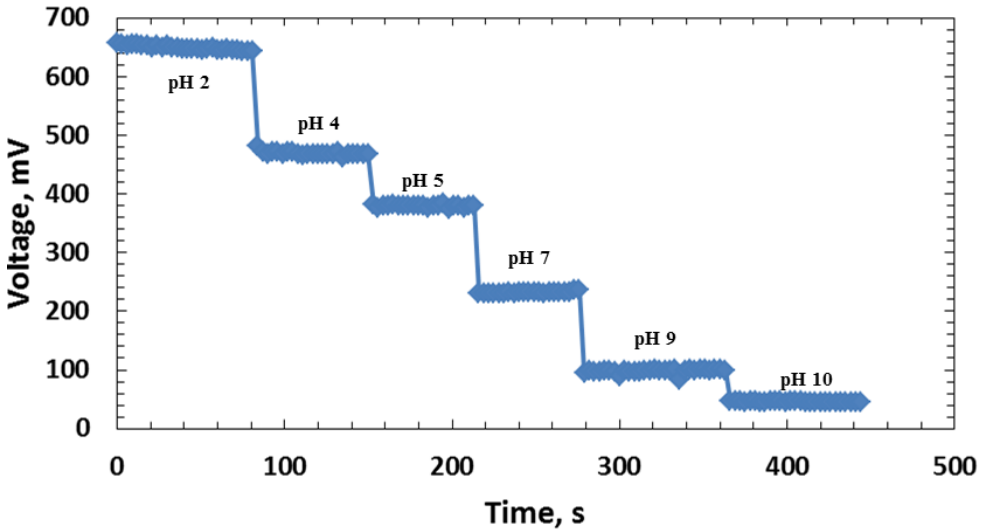


Figure 4-6: Sensitivity of our micro pH sensor featured with $IrO_x$ nanotubes on an electrode of 50×100 $\mu m^2$. The test was conducted with buffer solutions pH=2, 4, 5, 7, 9 and 10. A super-Nernstian response of 74.2 mV/pH was achieved.

Nernst responses. Our sensors with the response of 74.2 mV/pH indicated that the deposited $IrO_x$ has composition of both hydrated and dehydrated iridium oxide.

The repeatability tests for the sensor were carried out with buffer solutions with pH of 4, 7 and 10. The voltage responses of the sensor were sampled every 2 seconds in our recording program. The experiment started with pH=7 and 10, repeated again with pH=10, 7, and 4. The order of the buffer solutions was then reversed. The procedure was repeated 3 times. The sequence is shown in Figure 4-6. The periods of a certain solution left on the microelectrodes were random, but less than 100 seconds. The data were continuously logged during cleaning the sensor and changing the buffer solutions. In order not to disturb the experiment setup, the buffer solution was first removed by a pipette. DI water droplets were used to rinse the microelectrode. Then DI water was removed by the pipette before a new buffer solution was added. The program detected spikes of signals during changing solutions and filtered them out. The maximum voltage deviations for the buffer solutions

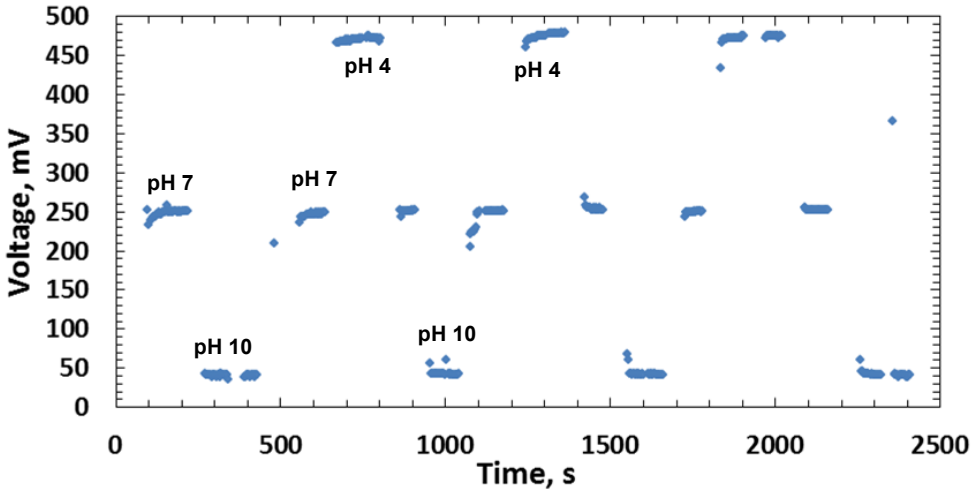


Figure 4-7: The repeatability and hysteresis tests with responses of the micro pH sensor. The experiments were conducted with buffer solutions pH=4, 7 and 10.

pH=4, 7, and 10 were 7.0, 5.0 and 2.0 mV, respectively, corresponding to variations of pH=0.094, 0.067, and 0.027. This demonstrated consistent responses in our micro-sensor.

The repeatability of the sensor was also investigated by monitoring sensor performance over time. Every 24 hours, the sensor was tested with buffer solutions pH=4, 7 and 10. Between experiments, the sensor was kept in phosphate buffer saline (PBS) solution, which was chosen as the sensor would have stayed in an environment of biological cells or tissues. The sensitivity of the sensor was found to reduce from the one in the first day, and became stable after the 3$^{rd}$ day. The average sensitivity was 65.3 mV/pH with a standard error of the mean (SEoM) of 1.6 mV/pH from the 3$^{rd}$ to 14$^{th}$ days. The high sensitivity of 74.2 mV/pH on the first day was likely owning to that the redox iridium oxide formed after electrodeposition might not be stable. Literatures agreed that the redox iridium oxide made by anodically electrodeposited process would reach a stable equilibrium after 2 days in PBS solution [88, 89].

*4.3.2 Temperature Dependence*

The potentials of the iridium oxide electrodes were intrinsically temperature dependent, as shown by the following formula [86]:

$$E = E^0 - \frac{RT}{zF}\mathrm{pH} \tag{4-2}$$

where the standard half-cell potential of the iridium oxide electrode $E^0$, Faraday's constant $F$, and gas constant $R$ are constants [86]. The number of moles of electrons transferred in the half-cell reaction $z$ depends on different redox mechanisms of $IrO_x$.

According to Huang *et al.*, the temperature dependence of the redox potentials $E$ are calculated with a coefficient of less than 2 mV/°C in the range of pH=2–10 [86]. In our experiment, the temperature dependence of the micro pH sensors featured with $IrO_x$ nanotubes was investigated in three different buffer solutions pH of 4, 7 and 10. Four sensors fabricated in the same batch were chosen for the experiments at five temperature points of 25°C, 35°C, 45°C, 50°C, and 55°C. The temperature was constrained in the range

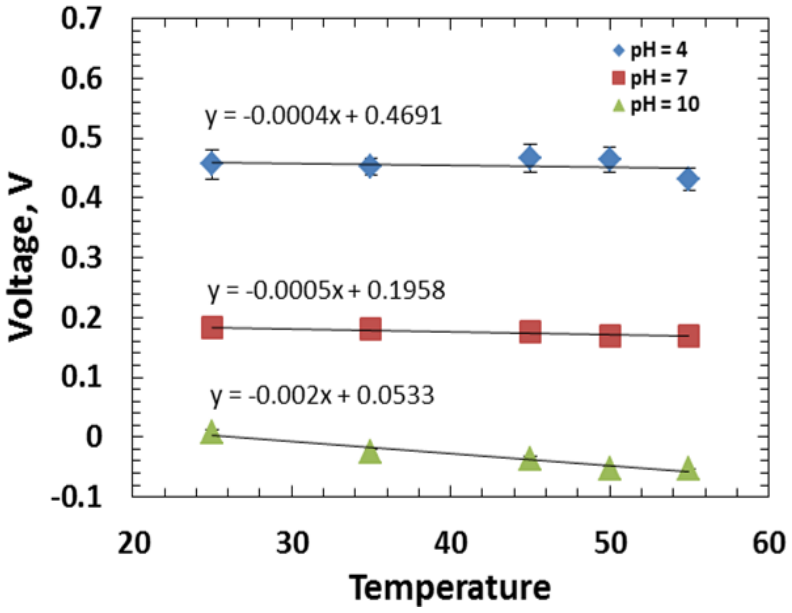


Figure 4-8: Temperature dependence of our micro pH sensor featured with $IrO_x$ nanotubes.

of 25–55°C for the use of pH sensors in biological applications. The buffer solutions in different beakers were kept in a water bath placed on top of a hot plate for uniformly heating and temperature controlling. The values of the measured temperature coefficients shown in Figure 4-7 were 0.4, 0.5 and 2.0 mV/°C at pH=2, 4 and 10, respectively. The error bars indicate the variations from four sensors. The results agreed well with the theory. The temperature dependence coefficients were small, especially for the buffer solution pH=7, at which most of the human body chemistry remains. Even at an acidic environment like stomach, the temperature dependence is still relative low. This means temperature dependent calibration of pH sensors may not be needed for most of *in vivo* applications.

*4.3.3 Higher Resolution pH Sensing*

Small differences in pH level within certain tissues in human body may reflect disorder of significant biological or physiological activities [3, 90]. Thus, pH sensors providing precise measurement with a higher resolution in a narrow range could be important for biomedical applications. In the following experiment, we demonstrated the use of our micro pH sensors to measure pH in a narrow range of 6.5–7.8. Solutions with pH=6.65, 6.90, 7.28, 7.51, 7.78 were prepared by mixing potassium biphthalate and sodium hydroxide (*Mettler-Toledo*) in dionized water. A commercial glass-rod pH meter (*Hanna Instruments*) was utilized as a reference to verify the pH values of each solution. A micro pH sensor was tested with each solution for 60 seconds. In the experiment, cleaning (rinsing and drying) procedures were not applied on the sensor as the solutions consecutively were added onto the microelectrode and withdrawn using a pipette. This procedure mimicked practical scenarios in sensing pH within biological tissues as the presence of solution residues may add interference to the sensor performance. Figure 4-8 shows the responses of sensors with distinguishable levels corresponding to different pH values. The voltage response of the sensor to the solution pH=6.65 initially has slowly

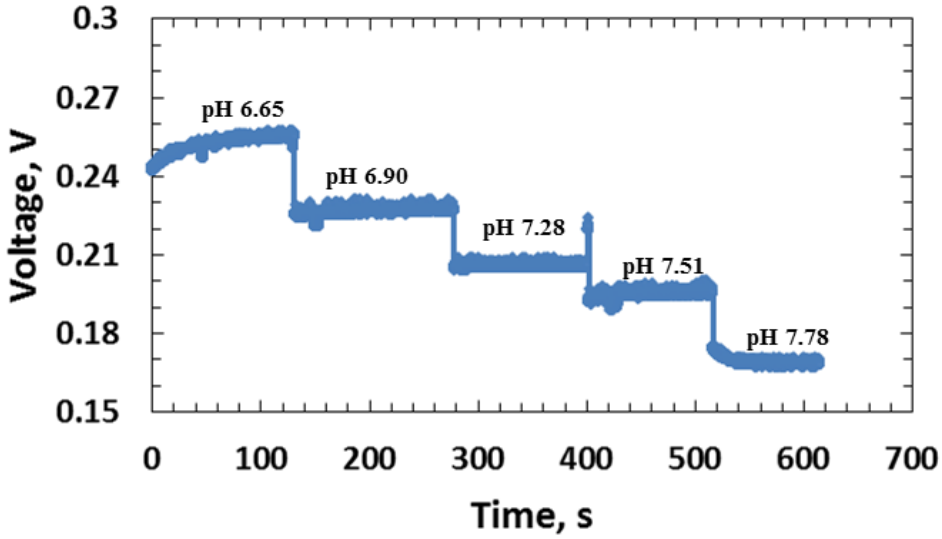


Figure 4-9: Higher resolution pH sensing test in a pH range of 6.65–7.78. Rinsing and drying steps were not applied during the test and different buffer solutions were sequentially dripped onto the sensor electrode to mimic practical sensing scenarios.

reached a stable condition, unlike the responses to other solutions. The phenomenon may be explained as the iridium oxide nanotubes were slowly hydrated in the aqueous environment from the initial condition of a dry electrode (the microelectrode was cleaned and air-dried) and reached to a new equilibrium point. The hydration process occurred within 20 seconds. Once the sensor surface was hydrated, the sensor responses were fast and stable with fluctuations less than 3 mV (Figure 4-8).

## 4.4 Discussions

Over deposition of $IrO_x$ is one of the major issues occurred during our investigation. The overflow of iridium oxide on top of the AAO template aggregate the $IrO_x$ into a single continuous layer, which induces the possibility that the whole piece of $IrO_x$ and the nanotubes underneath the piece peel off completely. The peeling off issue became severe when the AAO template is dissolved. It has been known that the electrodeposition of iridium

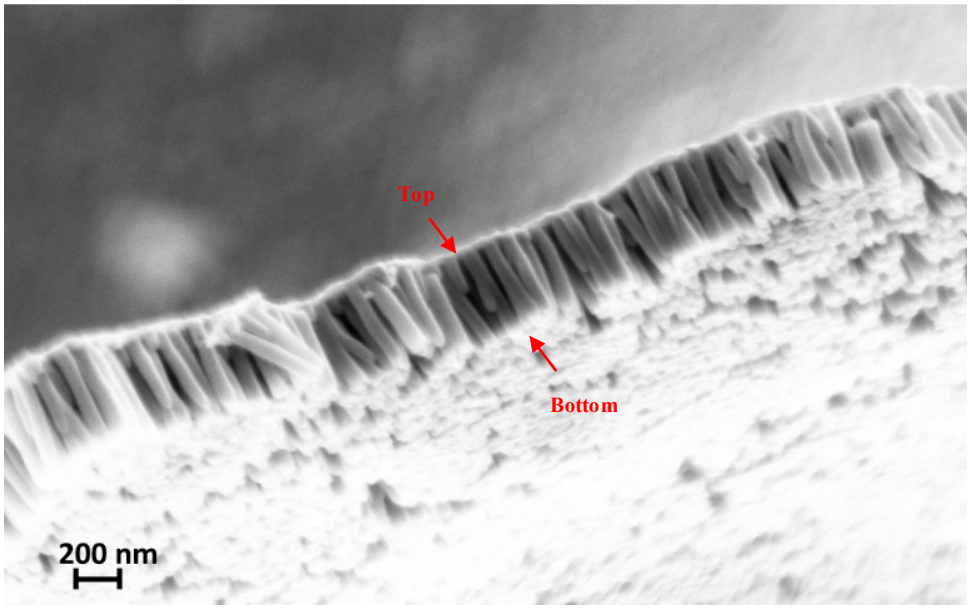


Figure 4-10: SEM photo of peeling-off $IrO_x$ nanotubes. The bottom portions of the nanotubes were peeled-off from the substrate while the top portions of the $IrO_x$ nanotubes were connected by the over-electrodeposited $IrO_x$ thin-film.

oxide yields poor adhesion [91]. Such method to grow iridium oxide nanotubes inside the AAO template pores also faces the similar issue. Each $IrO_x$ nanotube growing from the bottom of the nanopore has a small contact area. The free-standing nanotubes could be easily loosened and detached from their substrate or supportive metallic layers due to stresses occurred during dissolution of the AAO template in KOH solution when bubbles were formed. The peeling-off occurs more when the top surface of $IrO_x$ over the template pores connected together while the bottoms of the $IrO_x$ nanotubes tried to adhere to the substrate with much smaller areas. To show such events, a microsensor was fabricated with over-deposition of $IrO_x$. Figure 4-3(c) shows the top view of the microelectrode covered with a whole piece of an over-deposited $IrO_x$ layer. The device was dipped in the KOH solution for 2 hours to dissolve the AAO membrane. The nanotubes were detached and peeled-off as a whole piece from the substrate. As shown in Figure 4-9, the bottom portions

of individual nanotubes were peeled off from the gold layer while all nanotubes were still connected with their top portions to the over-deposited $IrO_x$ layer. To avoid such an overgrown issue, fabrication parameters should be tuned carefully to control the growth rate with respect to the thickness of the template on the microelectrodes.

## 4.5 Conclusions

In this Chapter, we developed pH sensors with patterned microelectrodes on which surfaces of 50×100 $\mu m^2$ were modified with electrodeposited iridium oxide nanotubes. Fabrication procedures and parameters were investigated. Nanotubes with diameters of 80–110 nm and length of approximately 1 μm were successfully grown on the defined electrode surface. The sensor exhibited super-Nernstian responses of 74.2 mV/pH initially, and 65 mV/pH stable over 14 days. The implementation of iridium oxide nanotubes allowed the micro-sensors, although with a small footprint, to have high sensitivity, fast responses and small voltage drifts. Repeatability and reversibility were also demonstrated. The pH sensing electrodes with high resolution and low temperature dependence could be utilized for many biomedical applications. The $IrO_x$ material, which is conventionally suitable for surface functionalization with enzymes and antibodies, along with our demonstrated cost-effective and low-temperature fabrication method for nanotubes could enable new types of high sensitivity biosensors.

# Chapter 5

# SOL-GEL-BASED IRIDIUM OXIDE FOR PSEUDO-REFERENCE ELECTRODES

## 5.1 Introduction

Implantable electrochemical sensors have emerged as one of the more attractive means for in situ sensing and monitoring biological conditions such as pH, pO2, and pCO2, physiological signals such as ECG, EEG, and biological analytes such as glucose, lactate, uric acid and neurotransmitters [5-7, 10, 92-94]. Reference electrodes (RE), the mandatory parts of the electrochemical sensors, are important to provide reference points for measurement [95-97]. Most biochemical sensors utilize dedicated silver/silver chloride (Ag/AgCl) wires as the REs in in vivo experiments [10, 98]. The Ag/AgCl wires are normally placed apart with a superfluous distance from the sensing sites due to difficulties of implantation processes [98]. Thus, sufficient ionic contact between the Ag/AgCl wires and the working electrode (WE) is required to guarantee a valid measurement of the sensor. Additionally, the Ag/AgCl RE is inconvenient, for example, in long-term experiments in which the sensor might be anchored to a mammalian organ and the additional electrodes would induce more injuries to tissues. Excessive noises are also predicted with the distant RE. Therefore, it is compelling that MEAs integrate both reference and working electrodes on the same probe [98].

On-probe planar Ag/AgCl reference electrodes have been considered in our previous work [25, 86]. However, many issues have been identified in biological applications. First, the traditional laboratory fabrication method using electroplating of bulk silver in a saturated chlorine solution has low throughput and is unrepeatable [99]. Second, the fabricated Ag/AgCl films easily delaminate and dissolve in long-term experiments, especially in biological environments with less chloride ions [97, 99-101]. Third, bulk and nano-structured silver electrodes have demonstrated cytotoxicity to living tissues in both

acute and long-term experiments [102, 103]. Iridium oxide (IrOx)-based electrodes have emerged as an attractive alternative for REs due to their unique properties. IrOx has been widely accepted in neuroscience applications, especially electrophysiological recording and stimulation because of its high charge density, biocompatibility, and corrosion resistance in electrolyte solutions [104-107]. In addition, IrOx electrodes, owing to their stable mechanical properties on both rigid and flexible electrodes, have been promisingly used for long-term experiments [98]. Although the electrode potential of IrOx is pH-dependent, it has been proven that the potential varies within a small dynamic range in biological environments where the change is less than 0.8 pH units [98, 108, 109]. Thus, we proposed to utilize IrOx electrodes as reference electrodes for biomedical recording; and we refer to them as pseudo-reference electrodes [110].

Previously, we knew that IrOx could be fabricated by different methods, such as directly sputtering using an IrOx target, thermal oxidation of iridium, anodic electrodeposition of IrOx, and sol-gel dip-coating. Sputtering and thermal oxidation of iridium are not preferable due to cost of materials needed. Electrodeposition has been well-developed and allows depositing hydrated IrOx onto micro-scale electrodes [98, 111]. However, the main shortcomings of the electrodeposited IrOx films are low adhesion to their substrates and delamination in biological environments [89, 112]. In addition, an issue of over-electrodeposition yielding conductive IrOx dendrites outside of the electrode areas could consequently cause cross-talk between electrodes in the MEA. Finally, higher dependence of such hydrated IrOx to pH change endowing a super-Nernst response of 66–72 mV/pH [89] is not desirable for pseudo-REs.

Sol-gel dip-coating has been implemented to fabricate IrOx electrodes for miniature pH sensor arrays [72, 113]. The method yields anhydrous IrOx films exhibiting the Nernst response around 56 mV/pH, which is lower than that of the electrodeposited

IrOx [72, 86]. Additionally, the IrOx film becomes stable and highly adhesive to the substrates after heat-treatment [86]. In this work, we investigated the implementation of the sol-gel-based IrOx films for pseudo-REs. The previous fabrication method introduced a thick SU-8 photoresist mask to precisely and selectively coat the gel solution on pre-defined electrodes [86]. However, the sacrificial layers degraded and became hard to remove after the heat treatment at 300 °C, thus it was difficult to apply the process for small electrode sites. Utilizing sol-gel processes with two-step heat treatment could prevent the aforementioned problem with the sacrificial layers. While the first step of pre-heating at a low temperature was aimed at dehydrating the sol-gel solution, the second one of curing at higher temperature was applied to yield a more adhesive amorphous IrOx thin film. The sacrificial photoresist mask was stripped off between these two steps. The lower temperature of the dehydration step allowed easy removal of the SU-8. Thus, it became possible to fabricate miniature electrodes with different dimensions on both rigid and flexible substrates.

In this Chapter, we introduced the modified sol-gel deposition to fabricate miniature IrOx electrodes. Various designs of IrOx electrodes have been fabricated on flexible substrates targeting biological applications. The pH-dependence of these electrodes was investigated. Long-term stability was examined in in vitro experiments by immersing the electrodes in acidic, alkaline and neutral solutions. The sol-gel-based IrOx electrode was integrated as the pseudo-RE of a dopamine (DA) sensor. The simple, cost-effective and high-throughput manufacturing processes yielded the DA sensor with many advantages such as high stability, reproducibility and high resolution.

## 5.2 Materials and Methods

### *5.2.1 Sensor Fabrication*

Microelectrodes of different dimensions were fabricated on a 125-μm polyimide flexible substrate. The substrate was cleaned with acetone and rinsed before applying 15-minute heat treatment at 100°C. Photolithography was carried out to pattern the microelectrodes of different sizes including 1 mm × 1 mm, 500 μm × 500 μm, and 100 μm × 100 μm for investigation. This was followed by deposition of layers of 15-nm thick chromium and 150-nm thick gold using an e-beam evaporator, as depicted in Figure 5-1(a). Lift-off was carried out to release sacrificial layers revealing the micro-patterns. Next, the negative-tone photoresist SU-8 (*MicroChem*) was spin-coated to form a mask layer. The thicker the SU-8 layer was, the easier it was to peel-off later. However, it was tedious to handle the device during fabrication processes. Thus, the thickness of the sacrificial mask layer was chosen as 50 μm. Different types of SU-8 including SU-8-2025, SU-8-50, and SU-8-100 were attempted. Based on our experimental data, we chose SU-8-50 to employ the 50-μm thick mask, as illustrated in Figure 5-1(b). The sample was then coated with an iridium chloride sol-gel solution (Figure 5-1(c)). The preparation of the solution and coating processes are described in Section 2.2. Figure 5-1(d) illustrates the peeling-off process after the first heat treatment step. The second heat treatment at 300°C was carried out to form a thin layer of iridium oxide (Figure 5-1(e)). In the final step, a 5-μm thick SU-8-5 layer was coated as an insulation layer covering the entire microelectrode except the sensing areas and connection pads, as shown in Figure 5-1(f). Finally, copper wires from external measurement circuits were connected to the pads using silver epoxy.

### *5.2.2 Sol-gel Deposition*

The sol-gel solution was mixed according to the recipe in [72] by dissolving 0.5-g iridium chloride in 21 ml of ethanol (*95%, Sigma*) and 5 ml of acetic acid solution (*99.7%,*

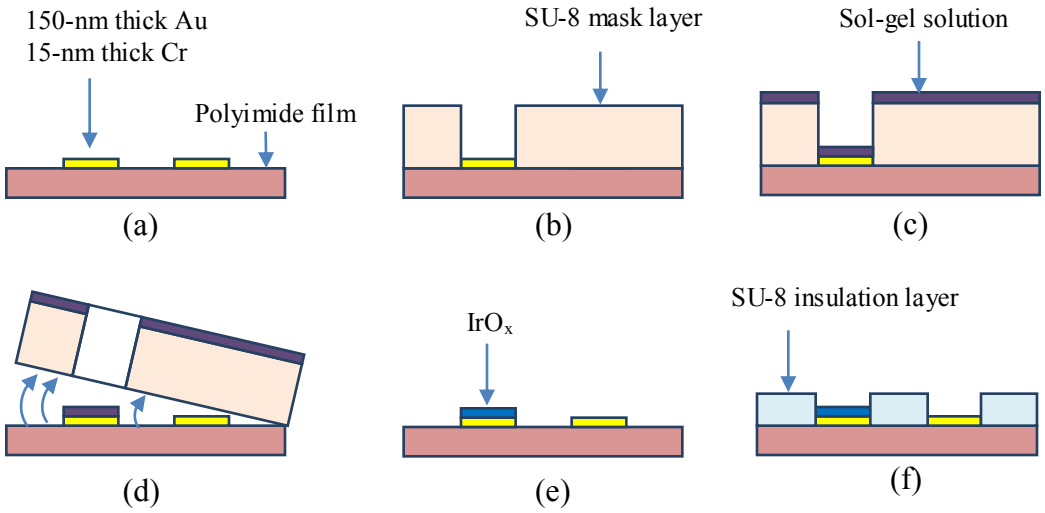


Figure 5-1. (a) Microelectrodes patterned on a flexible polyimide substrate. (b) A 50-μm thick SU-8 mask layer was fabricated for sol-gel deposition. (c) Sol-gel deposition of iridium chloride solution on the micro-electrodes. (d) The first heat treatment step at 100oC for 15 minutes was applied prior to peel-off of the mask layers. (e) The second heat treatment at 300oC was applied for four hours to produce IrOx. (f) A 5-μm thick SU-8 insulation layer was coated on the entire device except the sensing areas and connection pads.

*Glacial Ar*). The solution was stirred by a magnetic rod for one hour. Dip-coating process was carried out by immersing the entire substrate in the sol-gel solution. The SU-8 mask exposed only the sensing area of the micro-electrodes to the sol-gel solution for coating. After immersing the electrodes in the sol-gel solution for a few minutes, the whole substrate was drawn out with a withdraw rate of 2 cm/min using a dip-coating apparatus [72, 89]. The withdraw rate was experimentally determined at 2 cm/min to provide good film uniformity. The film quality and thickness had significant improvement when the dipping process was repeated five times.

After the sol-gel dip coating step, the sample was subjected to heat treatment to generate $IrO_x$ from iridium chloride. First, a heat treatment step at 100°C for 15 minutes dehydrated the sol-gel solution. Afterwards, the SU-8 sacrificial layer was peeled-off by

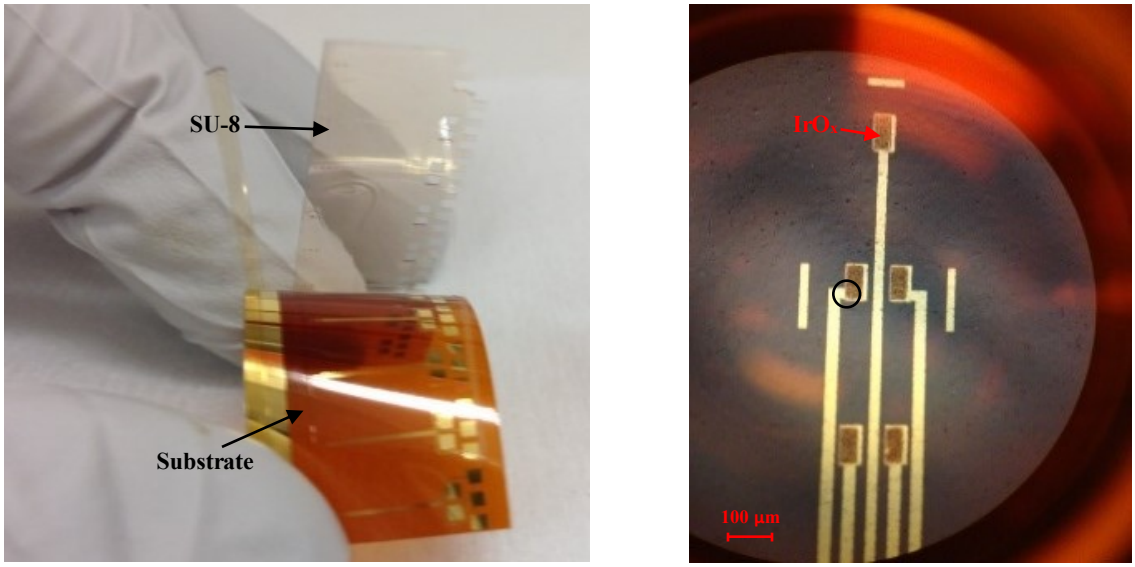


(a) (b)

Figure 5-2. (a) Photo of the peeled-off SU-8 mask layer after the first heat treatment. (b) A photo of the MEA with the sensing areas coated with IrOx. The sensing film size of each electrode was 50×100 µm2. The black circle on the top-right electrode of the MEA indicates the area imaged by a scanning electron microscopy in Figure 5-3(b).

bending the flexible substrate, as shown in Figure 5-2(a). It should be noted that the adhesion of SU-8 to the substrate is poor; therefore, the sacrificial mask was automatically detached by mechanical stresses. Next, a second heat treatment step was carried out with the samples in an oven. The heating profile was: (1) ramp-up to 300°C at a rate of 2°C/min; (2) soak at 300°C for four hours; and then (3) ramp-down to 25°C at a rate of 1°C/min. This step completed conversion of hydrated iridium chloride into iridium oxide, as illustrated by color change from brown to blue in Figure 5-1(e). The optical microscope photo in Figure 5-2(b) shows an MEA with five electrodes. Each electrode has opening area of 50×100 $\mu m^2$ and was coated with $IrO_x$.

*5.2.3 Material Characterization*

Iridium oxide fabricated by sol-gel deposition was characterized by energy dispersive spectroscopy (EDS). Figure 5-3(a) shows the material composition on the

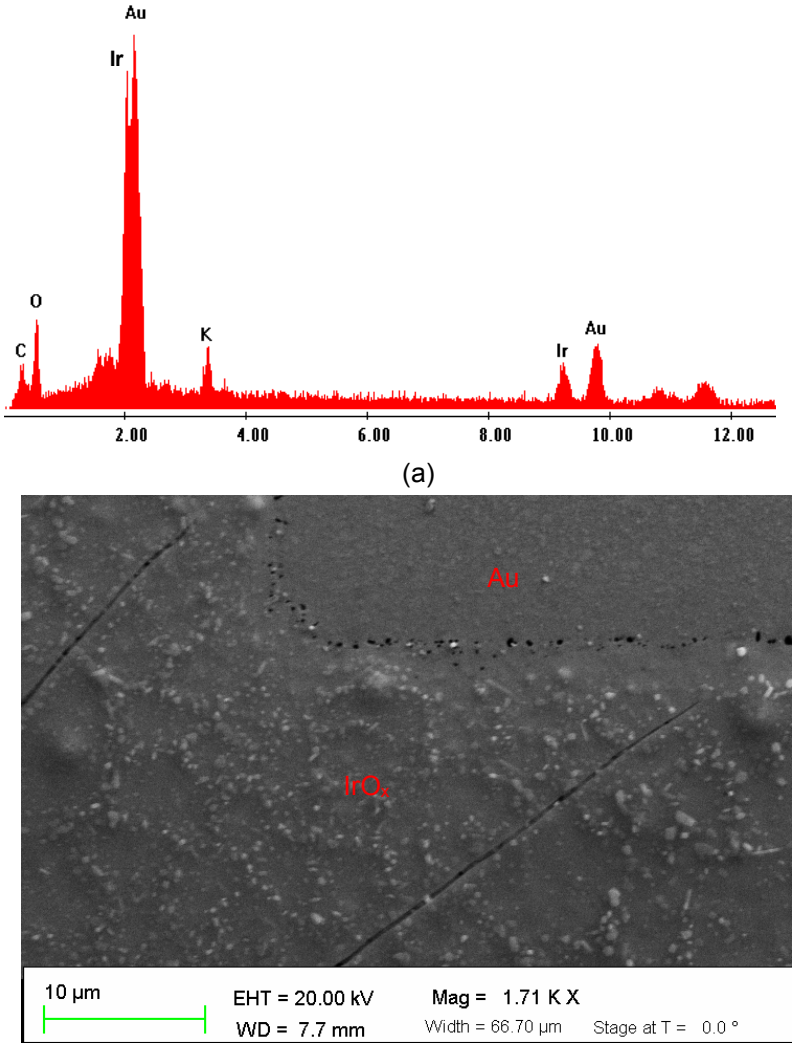


Figure 5-3: (a) Energy dispersive spectroscopy (EDS) shows visible peaks of Ir, Au, C, O, and K. (b) Scanning electron microscopic image of the surface on the microelectrode as indicated with the black circle in Figure 5-2(b).

surface of the electrode after sol-gel deposition. There were clear peaks of different materials including Ir, Au, C, O and K with composition percentages of 18.19%, 47.18%, 17.69%, 15.19% and 1.74%, respectively. The presence of carbon element was due to polyimide substrate while there was small amount of potassium due to contamination. Scanning electron microscopy was also utilized to examine of the surface morphologies of

the micro-electrode. The composition of the film is similar to the one made by one-step sol-gel heat treatment. Figure 3(b) shows the surface of the electrode coated with $IrO_x$, which was rougher than the one in the Au area. Micro-scale porous structures of $IrO_x$ were observed. The porous structures with a high surface-to-volume ratio could affect electrochemical properties of the bulk $IrO_x$ such as the ion exchange, rate to reach the equilibrium point of reversible reaction, or the amount of charge storage [86].

## 5.3 Experiments and Results

Typical electrochemical sensors have 3-electrode configuration with a working electrode (WE), a reference electrode (RE) and an auxiliary or counter electrode (CE). Applications using micro-electrochemical sensors could eliminate the CE since output signals of the sensor are small [10, 113, 114]. Among many electrochemistry methods, amperometric sensors require a fixed bias voltage applied between their WEs and REs. Since the output signals of the miniature amperometric sensors are in the range of pico-amps, the signals could be affected by minute changes of the bias voltage. Consequently, one of the important characters of the ideal RE is to provide a constant open-circuit potential regardless of electrolyte solutions. The change of $IrO_x$ electrode potential obeys its pH sensitivity. However, pH variations are narrowly limited in many *in vivo* biological mechanisms, especially targeted neurotransmitter concentration changes due to neuro-activities. Obviously a RE with less pH dependence is more preferable. Therefore, it is important to understand the pH dependency of the sol-gel-based $IrO_x$.

### *5.3.1 Characterization of Sol-gel-Based pH Electrodes*

The two-step sol-gel fabrication processes allow producing miniature $IrO_x$-based electrodes. Three different electrode dimensions including 1 mm × 1 mm, 500 μm × 500 μm and 100 μm × 100 μm were designed. Four electrodes of each type were fabricated and calibrated in order to demonstrate the reproducibility of the fabrication processes.

Open-circuit potentials of the $IrO_x$ micro-electrodes were measured versus a standard Ag/AgCl RE (*Basi*) in different standard buffer solutions pH= 4, 7 and 10 (*Mettler Toledo*). The open-circuit potential (*E*) of $IrO_x$ electrode in the half-reaction (5-1) is governed by the Nernst equation (5-2):

$$2IrO_2 + 2H^+ + 2e^- \leftrightarrow Ir_2O_3 + H_2O \quad (5\text{-}1)$$

$$E = E_0 + \frac{RT}{nF} log(C_{H^+}|_{x=0}) = E_0 - 0.059\ pH|_{x=0} \quad (5\text{-}2)$$

where $E_0$ is the standard electrode potential at 25°C, *R* is a gas constant, and *T*, *F* are denoted for temperature and Faraday's constant. The number of electron exchanged per proton *n* equals to one according to the Equation (5-1). The Equation (5-2) shows that the open-circuit potential depends on the concentration of proton $H^+$ near the surface of the electrode $C_{H^+}|_{x=0}$ or $pH|_{x=0}$.

Figure 5-4(a) shows the responses of four $IrO_x$ electrodes, each with a size of 500 µm × 500 µm, to the standard buffer solutions. The absolute slopes of pH responses were in a range of 51.3–58.3 mV/pH with a linear regression of approximately 0.993, which indicated Nernst response according to the Equation (5-2). Standard error of the means (SEoMs) of the measurements were 5.0 mV, 1.4 mV and 6.9 mV when measuring with commercial buffer solutions of pH=4, 7, and 10, respectively. Less SEoM in the case of the solution pH=7 indicated higher reproducibility of pH measurements in neutral solutions. The measured pH sensitivities of $IrO_x$-based electrodes with various dimensions are shown in Figure 5-4(b). Four electrodes of the same size were measured to obtain statistical variations. There were slight differences in sensitivity for electrodes size of 1 mm × 1 mm and 500 µm × 500 µm, which were 57±1.1 and 53±1.8 mV/pH. The smaller electrodes with a size of 100 µm × 100 µm exhibited less pH dependence of 47±1.4 mV/pH. The relationship between electrode potential and electrode size has not been well-studied yet the Nernst equation does not regard the sensor size. However, the empirical study showed

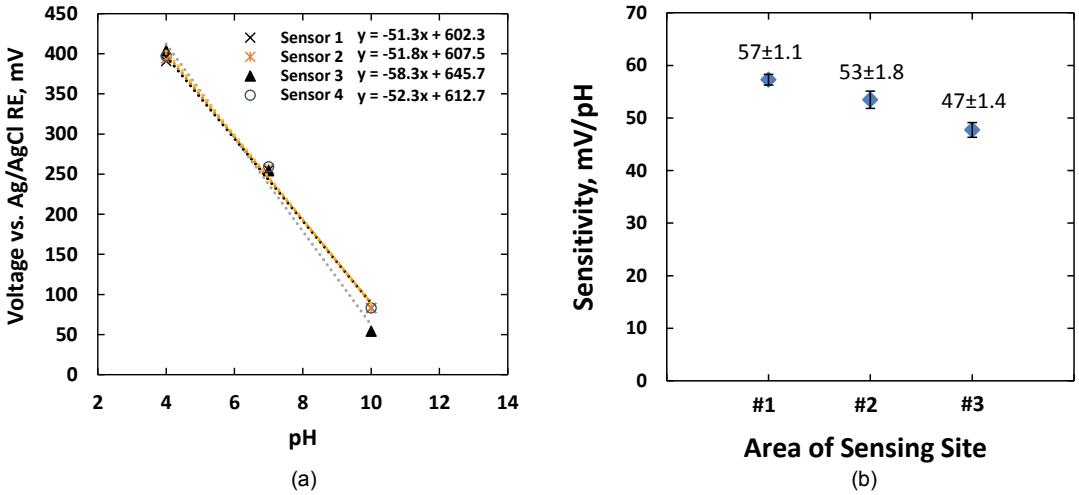


Figure 5-4: (a) The pH sensitivity of four IrOx-based electrodes with an electrode size of 500 µm × 500 µm versus a standard Ag/AgCl RE. (b) Sensitivities of IrOx-based electrodes with sizes of (#1) 1 mm × 1 mm , (#2) 500 µm × 500 µm, and (#3) 100 µm × 100 µm were 57±1.1, 53±1.8 and 47±1.4 mV/pH, respectively.

that the smaller electrode possessed less sensitivity. There are two possible reasons for the aforementioned phenomenon. Firstly, the reduced sensitivity of the miniature electrode might relate to the double layer region and diffusion layer formed around the finite space of the microelectrode in electrolyte solutions [114]. The ratio between the thickness of the diffusion layer and physical dimension of the electrode in such case became larger [114]. Bard *et al.* demonstrated that the profile of steady-state ion concentration was proportional to the inverse of distance from the electrode surface [114]. In other words, the local ion concentration and distribution of proton $H^+$ near the surface of the electrodes $pH|_{x=0}$ became complex and was adjusted from bulk ion concentration. Thus, the microelectrode showed less sensitivity to pH change of the solution. Secondly, a higher impedance in the smaller microelectrode (~ MΩ) which was comparable to the input impedance of the measurement system reduced the measured voltage from the actual open-circuit potential. An ultra-high input impedance will be needed in such cases.

With a pH sensitivity of 47–57 mV/pH for our miniature-dimension electrodes, the changes of pH in a typical biological environment within a range of 7.0−7.4 corresponded to a maximum variation of around 20 mV. Therefore, the variation in the open-circuit electrode potentials due to pH changes will be negligible compared to the applied bias voltage of 0.7 V in dopamine measurements.

*5.3.2 Long-term Stability of the $IrO_x$ Electrodes*

Longevity of the reference electrodes is critical in long-term electrochemical recording. Since we target biomedical applications, open-circuit potentials of the $IrO_x$ electrode versus a Ag/AgCl RE were examined in two different tests. First, the sensor was tested in a scenario in which the electrode surface first encountered a new biological environment during implantation. The pH sensitivity of the $IrO_x$ electrode was characterized when immersed in a 0.05-M phosphate buffered solution (PBS) for 36 hours. The PBS solution was chosen since it is a commonly used isotonic solution with physiologic pH. An $IrO_x$ electrode with a size of 500 μm × 500 μm was fabricated. Figure 5-5 shows potential responses of the $IrO_x$ electrode with different buffer solutions before and after immersing the electrode in the PBS solution. The measurements were repeated three times. The error bars in Figure 5-5 indicated the measurement variations. The measured sensitivities before and after the 36-hour experiment were 51.8 and 52.4 mV/pH, respectively.

The longevity was then further characterized to verify the performance of sol-gel-based $IrO_x$- electrodes in long-term implantable experiment. The sensors were immersed in different solutions including hydrochloric acid, fetal bovine serum (FBS), and an alkaline buffer solution. The choice of hydrochloric acid was to demonstrate that the sensor could function in a highly acidic biological environment such as inside the stomach with pH of around 2. The FBS solution was chosen because it is commonly used *in vitro* as serum-supplement for cell culture media. Another purpose for the experiment with FBS was to

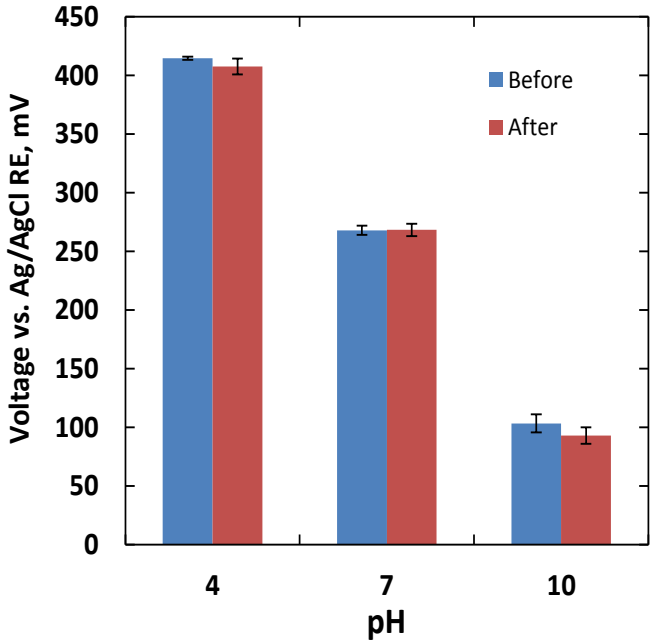


Figure 5-5: Open circuit potential of a 500 µm × 500 µm IrOx electrode before and after immersing it in 0.05-M PBS solution for 36 hours. The sensitivities were 51.8 and 52.4 mV/pH, respectively, before and after the experiment.

examine how the biofouling effect would affect performance of the sensing film. The alkaline buffer solution of pH=10 (*Mettler Toledo*), consisting of sodium hydroxide, potassium chloride and boric acid, was chosen to investigate if the film would be affected in an alkaline environment, and if abundant sodium and potassium ions, which are the most common ions in the biological environment, would affect the sensor lifetime.

In order to demonstrate the bending capability, six sensors were bended at different curvatures R= 14, 11, 8.4 and 3 cm. These sensors were fabrication in the same sol-gel batch and on the same substrate. The dimension of the sensors are 1 mm × 1 mm. Summary of the sensor sensitivities is illustrated in the Table 5-1. The sensor sensitivities have subtle change according to different curvatures. In addition, the SEoM of less than 3 mV/pH also indicated the reproducibility of the fabrication process.

Table 5-1: The sensitivities of six sensors on the array when the array was bended at different curvature radii.

| Bending | Mean of Sensitivities (mV/pH) | Standard Error of the Mean (SEoM) |
|---|---|---|
| Flat | 59.84 | 0.76 |
| Curvature R=14 cm | 58.97 | 1.03 |
| Curvature R=11 cm | 58.93 | 1.20 |
| Curvature R=8.4 cm | 59.87 | 1.06 |
| Curvature R=3 cm | 55.83 | 2.59 |

Twelve sensors with dimension of 1 mm × 1 mm were classified into four groups for the experiments. Three groups were kept in the individual beakers with hydrochloric acid (controlled at pH=2), alkaline buffer solution (pH=10), and standard tissue culture media RPMI 1640 supplemented with 10% FBS (*Fisher Scientific*). The electrodes in the fourth group were kept dry in air for comparison. The sensors of each group were tested daily with standard buffer solutions pH=4, 7, 10 to find the sensitivity curves. After the tests, the sensors were replaced in their original setups. The experiments were carried out for 30 days. Figure 5-6 shows the sensitivity results in the four different environments.

Figure 5-6(a) shows the responses of three sensors kept in the acidic solution with pH=2 over 30 days. The measurements were conducted after the $6^{th}$ day. The pH sensitivities of three sensors remained at 57.3±0.6 mV/pH after the $30^{th}$ day. Standard deviation of the calibration data over 30 days was less than 1.9 mV/pH, which reflected stable performance of these sensors. Figure 5-6(b) shows the responses of three sensors kept in the alkaline solution with pH=10. We noticed that the SU-8 insulation layer visually degraded and wrinkled while soaked in the alkaline solution after five days; however, the experiments were continued. The sensitivities of three sensors in this group were recorded at 48.1±0.55, 47.7±0.61 and 48.0±0.66 mV/pH after 30 days. The reduction in sensitivities was probably due to residues of alkaline solution and hydroxyl ions deeply absorbed and

retained at the mico- and nano-scale $IrO_x$ pores [72, 86]. The ion exchanges decreased diffusion processes and also altered equilibrium points from the double layer region when new solutions were tested. Both effects changed the electrode potentials of the sensors.

Figure 5-6(c) shows the sensitivities of three sensors kept in the FBS solution for 40 days. The average measured sensitivities were 57.4±0.3, 52.1±0.6, 51.7±0.9, 57.3±0.6, and 51.0±0.5 mV/pH on the 1$^{st}$, 3$^{rd}$, 10$^{th}$, 20$^{th}$ and 40$^{th}$ days, respectively. Experiment data showed that the pH responses of these three sensors to the buffer solution pH=7 decreased 17 mV over 40 days. This change in electrode potentials of the sol-gel $IrO_x$ electrodes were negligible compared to the applied bias voltage for amperometric sensors. Therefore, it is promising to use them as pseudo-reference electrodes in biological applications.

We noticed the pH sensitivity was reduced and remained at 42.0±0.6 mV/pH when the sensor were kept dry within 6 days of fabrication, as shown in Figure 5-6(d). The sensor sensitivity recovered to the Nernst performance after immersing in an aqueous solution for three hours. The highest SEoM in three measurements of 3.65 mV/pH was higher than the ones for the other electrodes in solutions. The lower sensitivity and higher variations in responses were probably due to dehydration and air filling up the micro- and nano-scale pores in the $IrO_x$ film surface. In other words, longer time was needed for the equilibrium points of the redox reaction to reach after ions exchange between solution and surface particles. Therefore, we concluded that the $IrO_x$-based electrodes should be preserved or presoaked in a hydrated condition such as PBS solution after fabrication in order to provide stable potentials. Identical conditions are also suggested for most commercially available reference electrodes.

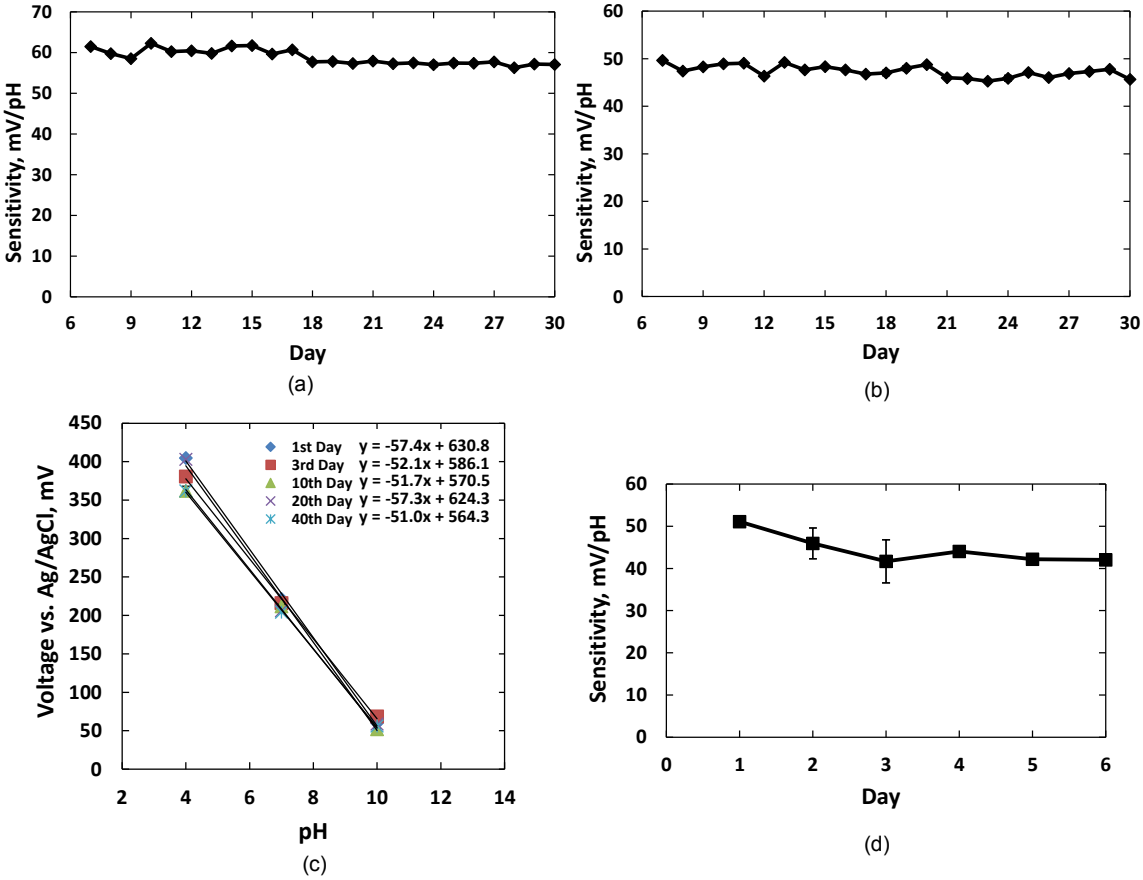


Figure 5-6: Longevity of IrOx-based electrodes was examined by soaking the electrodes in different solutions for a period of time, and keeping in dry condition. Twelve electrodes were classified into four groups. The sensor sensitivities of each group kept in: (a) hydrochloric acid solution (pH=2) for 30 days; (b) alkaline solution (pH=10) containing high concentration of sodium and potassium ions for 30 days; (c) standard tissue culture media supplemented with 10% FBS for 40 days; (d) dry condition for 6 days after fabrication were measured.

### *5.3.3 IrOx-Based Pseudo-Reference Electrodes*

Dopamine is one of the most ubiquitous neurotransmitters of the mammalian CNS. Recording of dopamine concentration in the CNS could help doctors to understand many diseases such as Parkinson's diseases, Alzheimer's diseases and neurodegenerative diseases [7, 115, 116]. Amperometry and cyclic voltammetry methods have been commonly used to detect dopamine [117, 118]. While the amperometry method utilizes a

fixed bias voltage, the cyclic voltammetry method sweeps the bias voltage. The applied voltages initiate redox reaction following Equation (5-3). If we denote dopamine ($C_8H_{11}NO_2$) as DA and $C_8H_{11}N(OH)_2$ as $DAH_2$, then Equation (5-3) is reduced to Equation (4). Current measurement recorded by amperometry and cyclic voltammetry methods follow the Butler-Volmer Equation (5-5) [117, 118].

$$C_8H_{11}NO_2 + 2H^+ + 2e^- \leftrightarrow C_8H_{11}N(OH)_2 \quad (5\text{-}3)$$

$$DA + 2H^+ + 2e^- \leftrightarrow DAH_2 \quad (5\text{-}4)$$

$$i = FAk_0[C_{DA}(0,t)e^{-\alpha f(E-E_0)} - C_{DAH_2}(0,t)e^{-(1-\alpha)f(E-E_0)}] \quad (5\text{-}5)$$

where $F$ is the Faraday constant, $A$ is active surface area of the electrode, $k_0$ is the rate of the reaction at equilibrium state, $C_x(0,t)$ is the concentration of chemical $x$, and $\alpha$ is transfer coefficient. Constant $f$ is calculated as $F/RT$, where $R$ is the gas constant and $T$ is temperature. According to the Equation (5-5), the redox current $i$ depends on the concentrations of DA and $DAH_2$ as well as the bias voltage $E$ between the WE and RE.

In our experiment, we implemented the amperometric method to detect the concentration of DA. The amperometric sensor consisted of a working (WE) and a reference (RE) electrodes. Two DA sensors were fabricated. They both employed gold electrodes with a size of 50 μm × 100 μm as the working electrodes. However, one sensor referred to a micro $IrO_x$ pseudo-RE while the other one was measured with a separated standard glass-tube Ag/AgCl RE. The $IrO_x$ pseudo-RE also had a size of 50 μm × 100 μm. The glass-tube Ag/AgCl RE consisted a Ag/AgCl wire with a diameter of 500 μm and a length of 5 mm. A fixed bias voltage of 0.7 V was applied between the RE and the gold WE for each DA sensor. The 0.7-V bias voltage was chosen since it generated peak redox currents [118, 119].

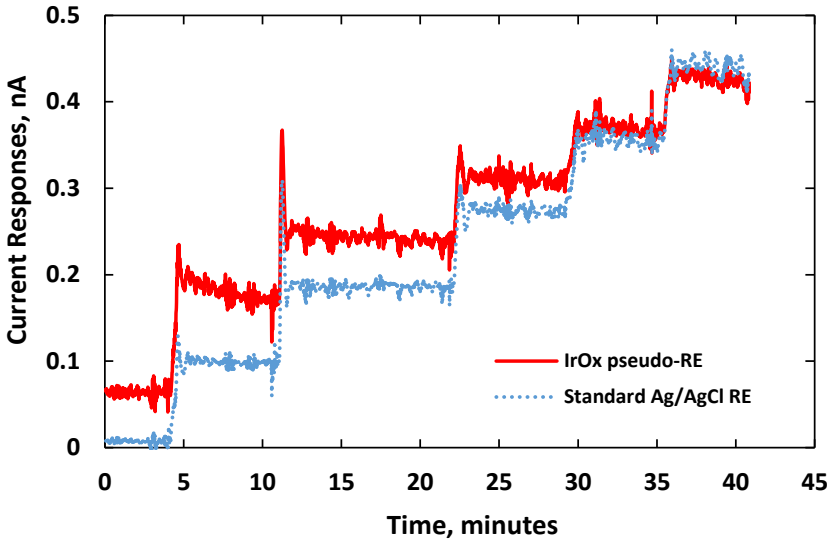


Figure 5-7: Electrical current responses of two DA sensors for incremental additions of 2.5-μM dopamine to 40 ml of 0.05-M PBS solution. Both sensors had identical gold WEs but with different REs: (red) the planar $IrO_x$ pseudo-RE; and (blue) a standard glass-tube Ag/AgCl RE.

Two sensors were kept in a beaker containing 40 ml of 0.05-M PBS solution. The temperature of the solution was maintained at 37°C with a water bath. The concentration of DA in the PBS solution was raised by incremental addition of 2.5 μM of DA (*Sigma*) under constant stirring by a magnetic rod. Electrical current was recorded with a commercial potentiostat (*Pinnacle, Inc.*). Figure 5-7 shows distinct responses to each increment of DA concentration. We noticed electrical current overshoots on both sensors as soon as the DA was added. The phenomenon happened in the transient period due to artifact noises or a local rise of ion concentration around the electrode [10, 114, 119]. The transient time between the adding of DA and the stable current response was short for both sensors demonstrating fast sensing electrode performance. Noises recorded by both sensors were also similar. The current responses damped down and reached their steady state after one minute.

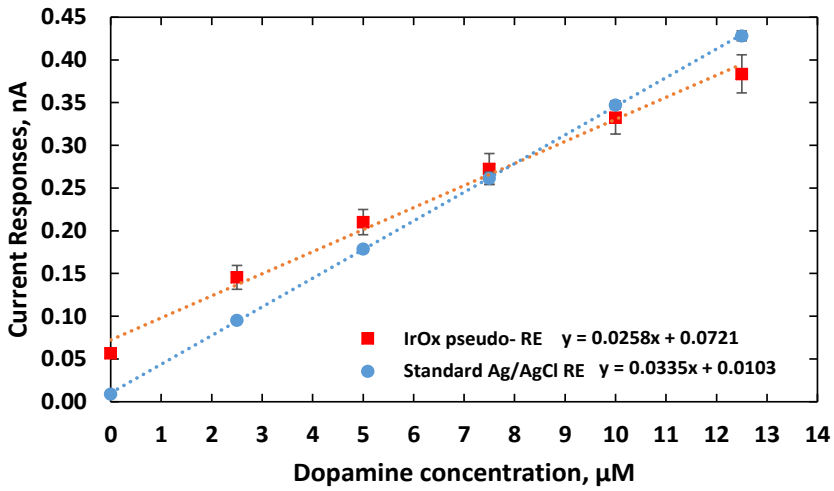


Figure 5-8: The sensitivity (slope) and repeatability (indicated by the standard error of the mean, SEoM) of two DA sensors after three trials. Both sensors have gold working electrodes with a size of 50 µm ×100 µm. One sensor has an external $IrO_x$ pseudo-RE (red line). The other sensor used an external standard Ag/AgCl reference probe (blue line).

The experiments were repeated three times recording electrical currents at various DA concentrations. As shown in Figure 5-8, the sensitivities of the two DA sensors were measured as 25.8±0.07 and 33.5±0.01 pA/µM, for using the $IrO_x$ pseudo-RE and a standard Ag/AgCl RE, respectively. Due to the fact that the highly electro-active $IrO_x$ has fast reversible redox reactions or a larger rate of reaction $k_0$ [27, 120], the DA sensor using the $IrO_x$ pseudo-RE has an output with higher baseline current. The measurements also indicated that the sensor exhibited less sensitivity than the one with a standard reference probe. It should be noted that the pseudo-RE has a miniature size (50 µm × 100 µm). According to the Equation (5-5), its sensitivity is expected to be less due to its higher impedance. Besides the electrode dimensions, to optimize the sensitivity, other factors should also be considered including spacing between the WE and RE, acquisition instrumentation configurations (input impedance and gain) and working electrode materials.

*5.3.4 IrOx-Based Working Electrodes*

We have also investigated the possibility of implementing $IrO_x$ electrodes for both working and reference electrodes. Dopamine sensors with the WE and RE on the same probe were fabricated with the same sol-gel batch processes. Each electrode had a size of 50 μm × 100 μm. A bias voltage of 0.7 V was applied between the two electrodes. The tests were carried out by incrementally adding DA to the PBS solution, as before. At the same time, another DA sensor consisting of a gold WE and a standard Ag/AgCl RE was placed in the beaker to compare results.

Figure 5-9 shows electric current responses of these two DA sensors while incremental adding 2.5-μM DA to raise the concentration of the PBS solution. The performance of the DA sensor with integrated $IrO_x$ WE and RE is similar to the one with a gold WE and an external Ag/AgCl reference probe. When the concentration of DA increased above 30 μM, the current responses of the DA sensor with the gold WE degraded. The degraded performance (blue curve) is indicated by * in Figure. 5-9. The degradation commonly happened with micro-electrodes due to accumulation of the byproduct ($DAH_2$) generated by the redox reaction within the micro-scale sensing area. This issue became more severe with higher background currents causing additional surface oxide or adsorbed hydrogen layer on the electrode surface [121, 122]. In the case of using sol-gel $IrO_x$ as the WE (red curve), the degradation was not observed. The $IrO_x$ sol-gel matrices with high porosity significantly improved the surface area of the micro-electrodes [123, 124]. The degradation with the $IrO_x$ WE was only initiated with a higher redox current. Therefore, the $IrO_x$-based WE could have higher dynamic range compared to the gold WE.

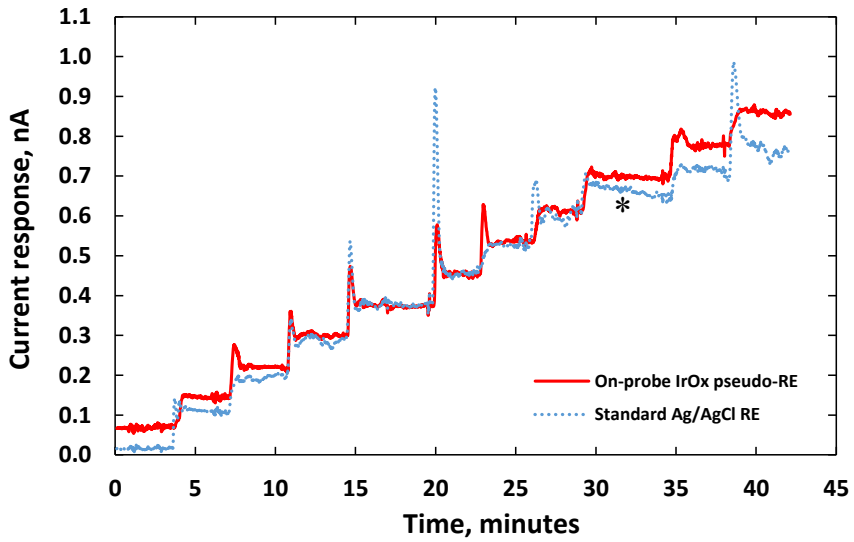


Figure 5-9: Current responses of two DA sensors for incremental additions of 2.5 µM dopamine to 40 ml of 0.05-M PBS solution: (red) the integrated DA sensor had an IrOx WE and an IrOx pseudo-RE on the same probe; and (blue) the other DA sensor had a gold WE with an external standard AgCl/Ag RE probe.

The electric current responses of the sensors were plotted as a function of DA concentration as shown in Figure. 5-10. The DA sensor utilizing $IrO_x$ WE and RE had a higher linear regression of 0.9997. It also coupled less noise although it still had a higher baseline, compared to the one using the external Ag/AgCl RE probe. This is due to the fact that the distance between the $IrO_x$ WE and RE was only 500 µm, which was much shorter than the distance between the gold WE and the external Ag/AgCl RE probe that had a fixed distance of 2 cm in our *in vitro* setup. Consequently, additional interferences from dynamic ion distribution between the electrodes with greater separation in solution added more noises into recorded potentials. The average standard deviation of measurement reflecting the dispersion of the measurement from the average sensor responses at different DA concentrations was 6 pA with the DA sensor integrating the $IrO_x$-based WE and RE, while for the one using the standard Ag/AgCl RE was around 9 pA. The sensitivities of these two

electrodes were 31.7 and 30.3 pA/μM, respectively. The limits of detections (LOD), the lowest quantity of dopamine that can be distinguished [125], were calculated to be 0.01 and 0.5 μM, respectively. Re-calibration after six days manifested the sensor sensitivities with a standard deviation of 27.8±2.9 and 28.6±4.0 pA/μM, respectively.

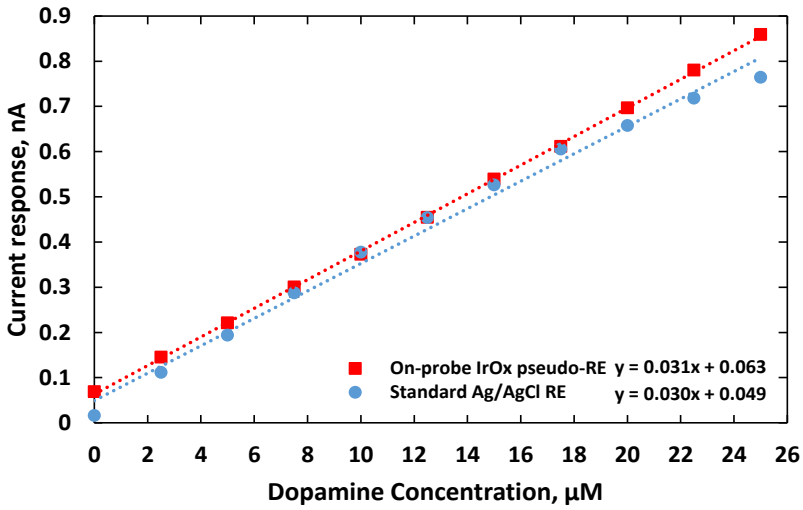


Figure 5-10: Sensitivities of (red) the DA sensor with integrated IrOx WE and IrOx pseudo-RE on the same probe; and (blue) the DA sensor that employed a gold WE and an external commercial glass-tube Ag/AgCl RE probe.

## 5.4 Conclusions

The sol-gel fabrication process utilizing a two-step heat treatment was developed to fabricate micro-scale $IrO_x$ electrodes on a flexible polymeric substrate. The fabrication processes allowed easy removal of the sacrificial mask layer after patterning while maintaining the film quality. The properties of the $IrO_x$ films were similar to the ones fabricated by the one-step heat treatment processes. Sensitivity to pH and longevity of the microelectrodes were studied. Sensor electrode performance did not change significantly over 30 days when they were kept in different environments designed to demonstrate their use in biomedical applications. Electrodes were demonstrated for application in DA concentration recording. The DA sensor with sol-gel $IrO_x$ working and pseudo-reference

electrodes on the same probe had similar sensitivity but less noise and better limit of detection than the one using a gold working electrode and an external Ag/AgCl reference probe. The flexible sensor with arrayed and integrated $IrO_x$ electrodes can be utilized in long-term implants to detect *in situ* multiple neurotransmitters for diagnosis of neural disorders.

# Chapter 6

# FUTURE WORKS

## 6.1 Introduction

For CNS disorders including Parkinson's disease, Alzheimer's disease, chronic pain and neurodegenerative disorder, it is particularly important to utilize implantable sensors for long-term monitoring. There is concerns about the effect of such implantable sensors in the CNS. It has been found that, the implantable electrode could cause damage to the CNS tissues. There are two types of injury: initial and sustained injury responses [126]. The initial injury responses relate to the device dimensions and mostly happen during surgery insertion. The responses could take effect for one week of post-implant. Otherwise, the sustained injury responses are less dependent of the device dimensions [126]. It has been demonstrated that the surface micro-motions of the brain tissue relative to the stationary brain [126, 126-130]. The micro-motions caused by pressure changes due to respiration or vascular pulsatility could be transferred and magnify along the micro-electrodes [126-129]. For example, Aaron Gilletti *et al.* observed that the micro-motions of the brain tissue is around 10−30 μm coming from respiration and 2−4 μm due to pulsatility [131]. Such micro-motions thus could generate displacement in the tip of the electrodes and consequently cause noises, measurement errors and/or damage blood vessels [128, 131, 132]. The sustained injury responses could take effect for four-weeks of post-implant. These, however, could be alleviated by the choice of materials [126, 127].

The use of conventional rigid needle-type microsensors made of metal, ceramic or silicon induce both initial and sustained injuries responses to cerebral tissues [130, 132]. Using flexible electrodes which have similar Young's modulus to the brain tissue could solve the issues. The flexible electrodes with capability of moving together with the cerebral tissues could suppress the micro-motions and then minimize damages to the tissue [129].

Computation simulation will demonstrate in the next section that the more flexible electrodes could cause less damage to the tissue. However, one issue has raised is that the flexible electrodes face difficulties to penetrate the tissue during implantation surgery [129, 132].

In this chapter, we will discuss on the new generation of ultra-thin and flexible implantable electrodes for biomedical applications. The sensing electrode was fabricated on Parylene-C (*poly*-(p-xylylene) polymers) substrates, which is biocompatibility, low Young's modulus and ease of fabrication. We suggested a solution to incorporate the ultra-thin and flexible electrodes with a biodegradable material that helps the electrode to penetrate into tissue during surgery. Such biodegradable will be dissolved after surgery and the sensing electrode will be exposed and ready for measurement.

## 6.2 Materials and Methods

### *6.2.1 Comparison of Rigid and Flexible Electrodes*

It is important to investigate the mechanical interaction of the implantable electrodes and body tissues. Finite element method using computerizing simulation is one of the powerful tools to do such task [126]. The ANSYS simulation model of the implantable electrode inside a brain tissue is illustrated in Figure 6-1. Since the model is symmetric, it is constructed using one half-symmetry module.

The electrode with a length of 7 mm, a thickness of 0.15 mm and a width of 0.3 mm was embraced and surrounded with model of brain tissue. Three different types of materials were chosen as materials for the electrodes, as described in the Table 6-1. While silicon is a traditional substrate for MEMS- and IC- devices, the polyimide has emerged as one of the common substrates for flexible circuitry. In our investigation, we introduce Parylene-C as one of the promising substrates for biomedical applications. The displacement of 1 μm is applied to the tail of the electrodes to mimic micro-motions relative

Table 6-1: Mechanical properties of substrates and brain tissue

| Materials | Density ($kg/m^2$) | Young's modulus | Poisson's Ratio |
|---|---|---|---|
| Silicon | 2329 | 200 GPa | 0.4 |
| Parylene-C | 1289 | 400 kPa | 0.33 |
| Polyimide | 1420 | 2.5 GPa | 0.34 |
| PVP | 1200 | 2.1 GPa | 0.33 |
| Brain Tissue | 1020 | 6 kPa | 0.3 |

between cerebral tissue and the skull. The displacement are following X-, Y-, and Z-directions as shown in Figure 6-1.

The total equivalent (*von*-Mises) elastic strains induced by such micro-motions following Y-direction are illustrated in Figure 6-2. In the case of the rigid probe, the displacement was transferred along the probe and the maximum equivalent strain of around 0.0337 µm/µm occurred at the tip of the probe. The simulation result indicated a severe scenario when the micro-motion at the tail of the probe could cause maximum

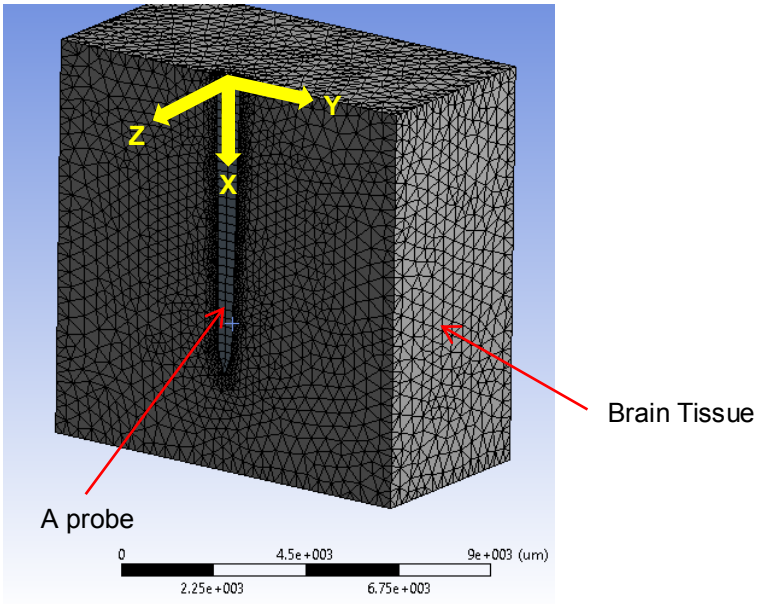


Figure 6-1: A half-symmetry model of a probe implanted inside brain tissue.

displacement at its tip and damage blood vessels (Figure 6-2(a)). Contradictory, in the case of the flexible probes (Figure 6-2(b) and (c)), the maximum displacement remained at the tail of the probes. In addition, in the case of Parylene-based probe, less train was observed than the one of polyimide-based.

Figure 6-3 summaries that the total equivalent (*von*-Mises) strain induced by micro-motions in different directions. It should be noted that the thickness of Parylene in the simulation is chosen to be 63 µm because our Parylene-coater could produce that thick layer within acceptable time (18 hour-deposition in 3 episodes). The thicker layer required longer deposition time became unrealistic. Based on the simulation data, the Parylene-substrate could be alleviated strain by around 40%, as compared to the conventional silicon-based probe.

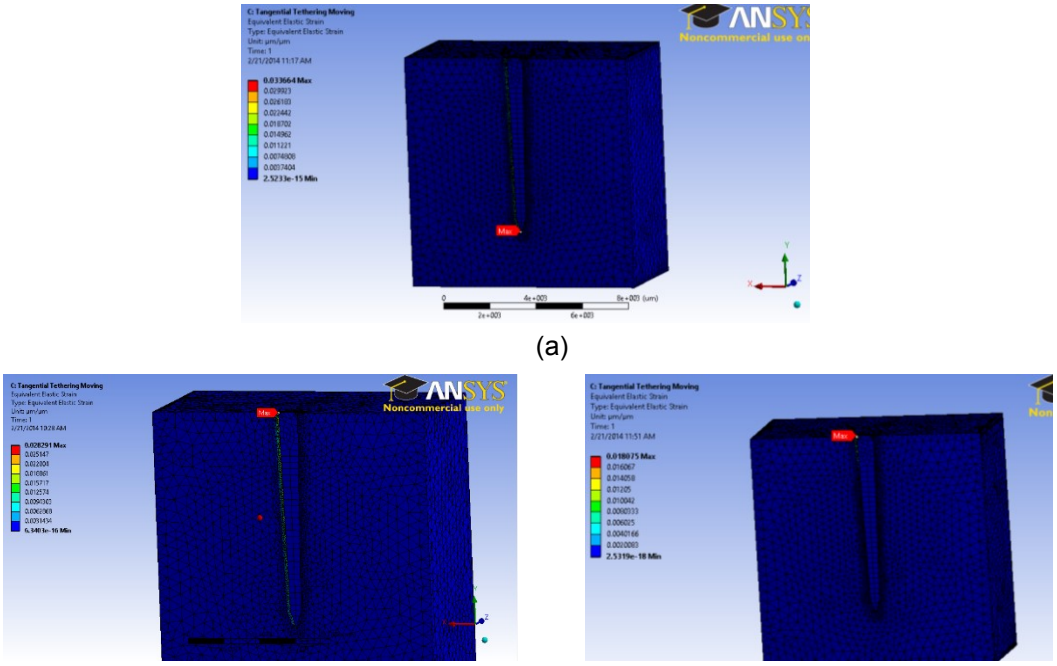


(a)

(b) (c)

Figure 6-2: Total equivalent elastic strains caused by tangential tethering displacement of 1 µm following Y-direction with the probes made of (a) silicon; (b) polyimide; (c) Parylene-C

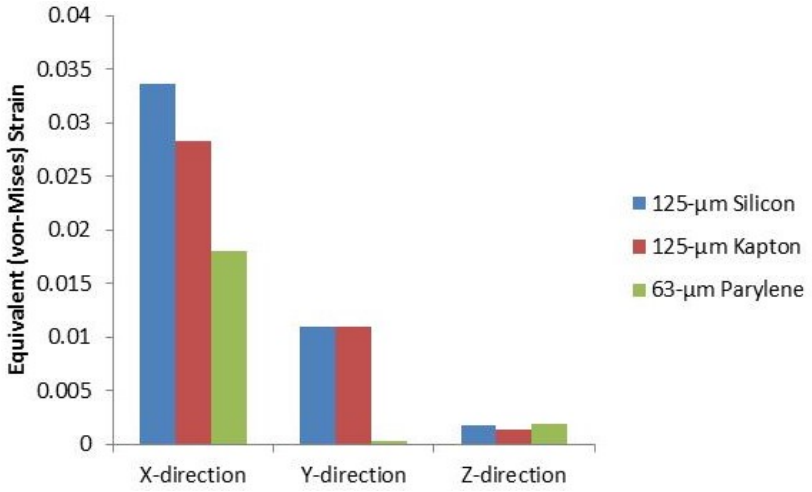


Figure 6-3: Total equivalent elastic strains caused by displacement of 1 µm following X-, Y- and Z-direction with the probes made of silicon; polyimide; and Parylene-C

*6.2.2 Enhancement Stiffness of the Ultra-Flexible Electrodes for Implant Insertion*

As shown previously, the use of ultra-thin and flexible substrate will reduce the risk of damaging blood vessels around the sensing sites. However, the insertion of such flexible probe during surgical implantation poses a challenge. It is necessary to temporarily increase the stiffness of the ultra-thin and flexible probes during the surgery. Once the probe is located to a desire location, the Young's modulus of the probe will decrease to close to the Young's modulus of the brain tissue. Such requirement urges to coat the Parylene-based probes with biodegradable materials. The advantage of this method is that the biodegradable materials will be dissolved inside the tissue body after time and expose the sensors.

The fabrication process is described in Figure 6-4. A glass slide was prepared and acted as the temporary carrier to provide uniformity for planar fabrication (step 1). A 20-µm thick Parylene substrate was formed on the glass slide by uniformly coating with a Parylene-coater in a chemical vapor deposition (step 2). A layer of NR-9 negative

photoresist was coated on the Parylene to pattern micro-electrode arrays in standard photolithography processes (step 3). The electrodes were defined in a lift-off process after metallization of 20-nm thick Cr and 150-nm thick Au layers. SU-8 insulation layer was coated and patterned to expose only the sensing areas and connection pads (step 4). Then, the probes on the ultra-flexible Parylene substrate thus were peeled off from the glass slide in the step 5. The mechanical stiffness of the flexible substrate was enhanced by dip-coating in 50wt% PVP solution before individual probes were tailored by laser machining (step 6). It should be noted that the PVP biodegradable materials was chosen because it is biocompatible, water soluble, easy to prepare and coat and becomes stiff when dried. Finally, each individual probe was manually tailored out using scissors, as shown in the step 7.

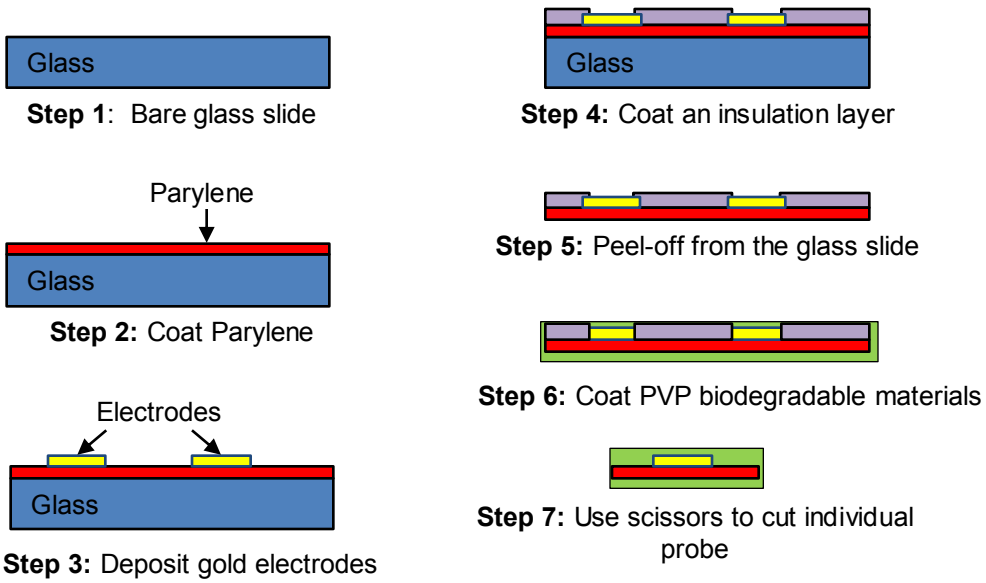


Figure 6-4: Fabrication processes: (1) Use a bare glass slide as the supportive substrate; (2) Coat Parylene on the glass slide; (3) Deposit micro-electrode arrays; (4) Coat an SU-8 insulation layer; (5) Peel-off the micro-electrode array patterned on Parylene; (6) Dip-coating to coat PVP biodegradable materials; (7) Use scissors to carefully cut an individual probes.

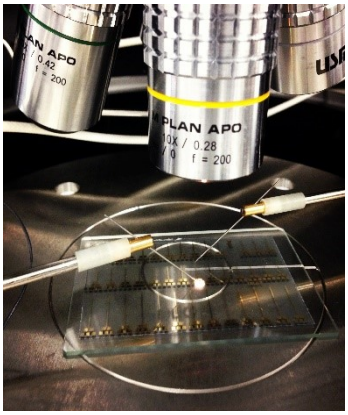


(a)

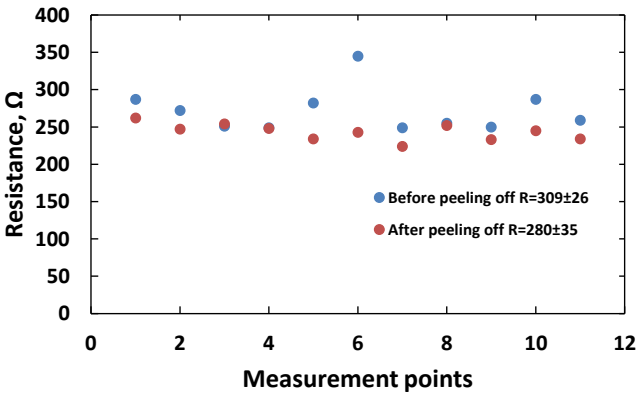


(b)

Figure 6-5: (a) Experiment setup to measure resistance between the tip and the contact pad of a micro-electrode using a probe station. (b) Resistance remains similar before and after the peeling off step.

In the step 5, there is concern about film cracks that may be introduced when the ultra-thin and flexible substrate was peeled off from the glass slide. Resistance were measured using a probe station before and after the peeling off step. The experiment setup is shown in the Figure 6-5(a). Two probes were connected to the tip and the contact pads of a micro electrodes. The measurements were repeated 11 times. The resistance between two points in the Figure 6-5(b) shows subtle changes; thus, the peeling off step does not affect the film quality.

Computation simulation again was utilized to investigation the capability of the PVP-encapsulated to penetrate through tissues. The probe was modeled with a 20-μm thick probe coated with different layer of the PVP, as shown in Figure 6-4 (a). The simulation indicated that the one with 125-μm thick PVP was able to penetrate the brain tissue model (Figure 6-6).

## 6.3 Preliminary Results and Discussion

Figure 6-7 (a) shows photos of the microelectrode array fabricated on the ultra-flexible Parylene substrate after being peeled off from the glass slide. The sensor array

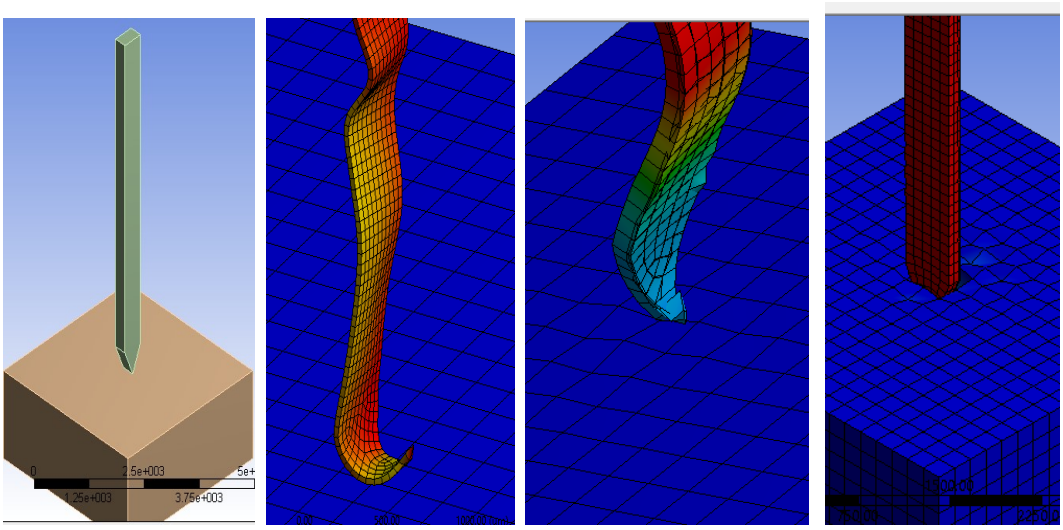

(a) (b) (c) (d)

Figure 6-6: Simulation results showing interaction of 20-μm thick probe and the brain tissue: (a) Modeling of the simulation; and the probe was encapsulated with (b) 50-μm thick, (c) 100-μm thick and (d) 125-μm thick PVP layer.

was flexible enough to be wrapped around a finger, as shown in Figure 6-7(a), without physical changes to electrodes. Each sensor array had five electrodes of 50×100 $\mu m^2$ each. The lengths of the probe varied from 7 mm to 12 mm for implanting at different brain sites. Figure 6-7(b) demonstrates the stiffened device after sol-gel dip-coating with PVP. The entire substrate could be held by tweezers without collapsing down.

The individual probe was tailored by scissors. The stiffness of the probe was demonstrated by inserting the sensor into a rat brain. Figure 6-8 showed the experiment to poke the rat brain using the fabricated probe. In the Figure 6-8(a), the probe was too flexible to penetrate the rat brain. After encapsulated by the PVP biodegradable materials, it could

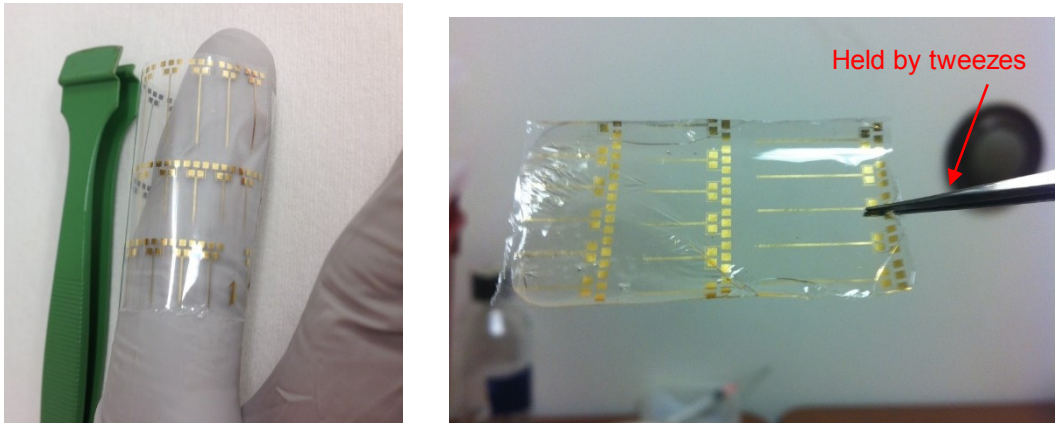


(a) (b)

Figure 6-7: Actual photos of the MEA made on 20-μm thick Parylene: (a) before coating the biodegradable layer; (b) after coating the biodegradable layer.

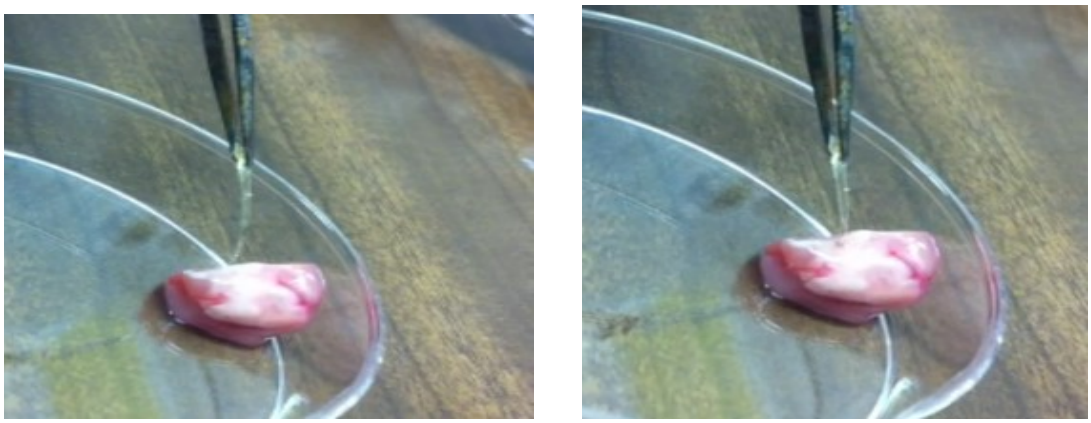

(a) (b)

Figure 6-8: Penetrating the 20-μm thick Parylene-based probe into a rat brain: (a) before coating the biodegradable layer; (b) after coating the biodegradable layer.

penetrate the rat brain without any difficulty. The PVP biodegradable material was dissolved away after 10 minutes in a wet environment.

## 6.4 Future Works

An implantable microsensor array was designed and fabricated on an ultra-flexible Parylene substrate. The mechanical stiffness of the sensors was enhanced by sol-gel dip-coating with PVP, a biodegradable material. Simulation and experimental results confirmed

the micro-probe was stiff enough to insert into the brain for implantation. There are few investigations needed to be conducted:

1) Establishing the relationship between withdraw rate of the dip-coating process and the coating thickness of the biodegradable material.
2) Investigating the integration the nanoporous AAO template on the ultra-thin and flexible micro-electrodes
3) Investigating growing of $IrO_2$ nanorods on the ultra-thin and flexible micro-electrodes.
4) Investigating growing of $IrO_x$ nanotubes on the ultra-thin and flexible micro-electrodes.
5) Developing multi-functional micro-electrode array including L-glutamate sensors, L-lactate sensors, dopamine sensors and pH sensors in a fully integrated sensing system.

# Appendix A

## RECIPE TO COAT THICK NR-9 PHOTORESIST LAYERS

The negative photoresist NR9-1500PY (Futurrex) is popularly used for lift-off process with small feature size. In the application to grow aluminum oxide nanorods, the total thickness of metallic supportive layer is around 1 μm. Therefore, if we use NR9-1500PY for such lift-off application, it is suggested to coat a thick NR9 layer (at least 2 μm). This following recipe has been used to coat 2-μ thick NR9 layer. The exposure wavelength is of 365 nm.

- Step 1: Spin coat NR9-1500PY for 45 seconds at 1700 rpm.
- Step 2: Pre-bake (soft-bake) at 150$^{o}$C for 60 seconds.
- Step 3: Expose for 16 seconds under a power of 20 mW/cm$^{2}$.
- Step 4: Post-exposure bake at 100$^{o}$C for 60 seconds.
- Step 5: Develop in RD6 resist development for 12 seconds.
- Step 6: Dry at 100$^{o}$C for 5 minutes.

Verify the thickness of the NR9-1500PY layer of 2 μm by profilometer.

# Appendix B

## RECIPES TO COAT THICK SU-8 PHOTORESIST LAYERS

The negative photoresist SU-8 (Microchem) is popularly used for high aspect ratio mold, insulation layers and sacrificial masks in sol-gel dip-coating applications. In the application of sacrificial masks, the thickness of the SU-8 layer is around 40−50 μm. The exact thickness is not critical since the sacrificial SU-8 layer will be peeled-off eventually. We chose different photoresists for this application including SU-8-25, SU-8-50 and SU-8-100. The SU-8 is a better choice since it takes less time for coating process. However, the layer quality yielded by these photoresists are similar. The following recipe is applied with the exposure wavelength of 365 nm.

**SU-8-25**

- Step 1: Spin coat SU-8-25 for 60 seconds at 1000 rpm.
- Step 2: Pre-bake (soft-bake) at 65°C for 10 minutes and 95°C for 20 minutes. Longer pre-bake time may be applied without damaging the SU-8 layer.
- Step 3: Expose for 25 seconds under a power of 20 mW/cm$^2$.
- Step 4: Post-exposure bake at 65°C for 5 minute and 95°C for 10 minute.
- Step 5: Develop in SU8 developer for 6 minutes.
- Step 6: Dry at 65°C for 5 minutes.

Should not use high temperature at the step 6, which may affect the peeling off step later on.

**SU-8-50**

- Step 1: Spin coat SU-8-50 for 60 seconds at 3000 rpm.
- Step 2: Pre-bake (soft-bake) at 65°C for 10 minutes and 95°C for 30 minutes. Longer pre-bake time may be applied without damaging the SU-8 layer.
- Step 3: Expose for 30 seconds under a power of 20 mW/cm$^2$.
- Step 4: Post-exposure bake at 65°C for 5 minute and 95°C for 10 minute.
- Step 5: Develop in SU8 developer for 6 minutes.

- Step 6: Dry at 65°C for 5 minutes.

Should not use high temperature at the step 6, which may affect the peeling off step later on.

**SU-8-100**

- Step 1: Spin coat SU-8-100 for 30 seconds at 3000 rpm and another 30 seconds at 4000 rpm.
- Step 2: Pre-bake (soft-bake) at 65°C for 10 minutes and 95°C for 40 minutes. Longer pre-bake time may be applied without damaging the SU-8 layer.
- Step 3: Expose for 30 seconds under a power of 20 $mW/cm^2$.
- Step 4: Post-exposure bake at 65°C for 5 minute and 95°C for 20 minute.
- Step 5: Develop in SU8 developer for 10 minutes.
- Step 6: Dry at 65°C for 5 minutes.

  Should not use high temperature at the step 6, which may affect the peeling off step later on.

# Appendix C

## RECIPES TO MAKE IROX SOLUTIONS

### 1. The chemical bath deposition

The salt solution made for the chemical bath deposition and the deposition process are mixed following these steps:

- Step 1: Prepare 40 ml deionized water
- Step 2: Add 0.1 gram of $IrO_4.2H_2O$ and mix for 3 hours using a magnetic rod. The salt solution can be kept at 4°C and use for multiple times.
- Step 3: Place a wafer integrated with anodic aluminum oxide (AAO) template into a 5-ml salt solution.
- Step 4: Add 1.5 mg of $K_2CO_3$.
- Step 5: Heat up at 90°C for 30 minutes.

### 2. Electrodeposition solution

The solution for electrodeposition process is prepared following these steps:

- Step 1: Prepare 50 ml deionized water
- Step 2: Add 0.075 gram of IrO4.2H2O and mix for 30 minutes using a magnetic rod.
- Step 3: Add 0.5 ml of 30% $H_2O_2$ and mix for 30 minutes using a magnetic rod.
- Step 4: Add 0.5 gram of $C_2H_2O_4.2H_2O$ and mix for 1 hour using a magnetic rod.
- Step 5: Gradually increase the pH of the solution by adding $K_2CO_3$ until pH=10.5. The solution is kept at 4°C for 2 days before using.

### 3. Sol-gel solution

The sol-gel solution for dip-coating process is prepared following these steps:

- Step 1: Prepare 21 ml of ethanol ($C_2H_5OH$).
- Step 2: Add 0.5 gram $IrO_4.2H_2O$ and mix for 30 minutes using a magnetic rod.
- Step 3: Add 5 ml of acetic acid ($CH_3COOH$) and mix for 2 hours using a magnetic rod. The solution is kept at 4°C and use for multiple times.

References

[1] P. Kurzweil, "Metal oxides and ion-exchanging surfaces as pH sensors in liquids: State-of-the-art and outlook," *Sensors*, vol. 9, no. 6, pp. 4955-4985, 2009.

[2] R.G. Sawyer, M.D. Spengler, R.B. Adams and T.L. Pruett, "The peritoneal environment during infection. The effect of monomicrobial and polymicrobial bacteria on pO2 and pH." *Annals of Surgery*, vol. 213, no. 3, pp. 253,1991.

[3] K.E. Schaefer, "Blood pH and pCO2 homeostasis in chronic respiratory acidosis related to the use of amine and other buffers," *Annals of the New York Academy of Sciences*, vol. 92, no. 2, pp. 401-413,1961.

[4] E. Jovanov, A. O'Donnell Lords, D. Raskovic, P.G. Cox, R. Adhami and F. Andrasik, "Stress monitoring using a distributed wireless intelligent sensor system," *Engineering in Medicine and Biology Magazine, IEEE*, vol. 22, no. 3, pp. 49-55, 2003.

[5] Y. Hu, Y. Zhang and G.S. Wilson, "A needle-type enzyme-based lactate sensor for in vivo monitoring," *Analytica Chimica Acta*, vol. 281, no. 3, pp. 503-511,1993.

[6] J. Wang, J. Liu, L. Chen and F. Lu, "Highly selective membrane-free, mediator-free glucose biosensor," *Analytical Chemistry*, vol. 66, no. 21, pp. 3600-3603,1994.

[7] T.T. Tseng and H.G. Monbouquette, "Implantable microprobe with arrayed microsensors for combined amperometric monitoring of the neurotransmitters, glutamate and dopamine," *Journal of Electroanalytical Chemistry*, vol. 682, pp. 141-146, 2012.

[8] H. Cao, C. Nguyen and J. Chiao, "Fabrication and surface-modification of implantable microprobes for neuroscience studies," *Advances in Natural Sciences: Nanoscience and Nanotechnology*, vol. 3, no. 2, pp. 025003, 2012.

[9] C.M. Nguyen, W. Huang, S. Rao, H. Cao, U. Tata, M. Chiao and J. Chiao, "Sol-Gel iridium oxide-based pH sensor array on flexible polyimide substrate," *Sensors Journal, IEEE*, vol. 10, pp. 3857-3864, 2013.

[10] H. Cao, A. Li, C.M. Nguyen, Y. Peng and J. Chiao, "An Integrated Flexible Implantable Micro-Probe for Sensing Neurotransmitters," *Sensors Journal, IEEE*, vol. 12, no. 5, pp. 1618-1624, 2012.

[11] Y.H. Liao and J.C. Chou, "Preparation and characteristics of ruthenium dioxide for pH array sensors with real-time measurement system," *Sensors and Actuators B: Chemical*, vol. 128, no. 2, pp. 603-612, 2008.

[12] K.M. Wassum, V.M. Tolosa, J. Wang, E. Walker, H.G. Monbouquette and N.T. Maidment, "Silicon wafer-based platinum microelectrode array biosensor for near real-time measurement of glutamate in vivo," *Sensors*, vol. 8, no. 8, pp. 5023-5036, 2008.

[13] M. Suzuki, H. Nakabayashi, Y. Jing and M. Honda, "Micro-arrayed cellular chips with optical sensor membranes for pH and oxygen," vol. 2, pp. 1716-1719 Vol. 2, 2005.

[14] S. Xu, C. Lao, B. Weintraub and Z.L. Wang, "Density-controlled growth of aligned ZnO nanowire arrays by seedless chemical approach on smooth surfaces," *Journal of Materials Research*, vol. 23, no. 8, pp. 2072-2077, 2008.

[15] N. De Tacconi, C. Chenthamarakshan, G. Yogeeswaran, A. Watcharenwong, R. De Zoysa, N. Basit and K. Rajeshwar, "Nanoporous TiO2 and WO3 films by anodization of titanium and tungsten substrates: Influence of process variables on morphology and photoelectrochemical response," *The Journal of Physical Chemistry B*, vol. 110, no. 50, pp. 25347-25355, 2006.

[16] I. Robel, V. Subramanian, M. Kuno and P.V. Kamat, "Quantum dot solar cells. Harvesting light energy with CdSe nanocrystals molecularly linked to mesoscopic $TiO_2$ films," *Journal of the American Chemical Society*, vol. 128, no. 7, pp. 2385-2393, 2006.

[17] Reui-San Chen, Y.S. Huang, D.S. Tsai, S. Chattopadhyay, C.T. Wu, Z.H. Lan and K.H. Chen, "Growth of well aligned $IrO_2$ nanotubes on $LiTaO_3$ (012) substrate," *Chemistry of materials*, vol. 16, no. 12, pp. 2457-2462, 2004.

[18] R.S. Chen, Y.S. Huang, Y.M. Liang, D.S. Tsai, Y. Chi and J.J. Kai, "Growth control and characterization of vertically aligned IrO2 nanorods," *Journal of Material Chemistry*, vol. 13, no. 10, pp. 2525-2529, 2003.

[19] A. Grupioni, E. Arashiro and T. Lassali, "Voltammetric characterization of an iridium oxide-based system: the pseudocapacitive nature of the $Ir_{0.3}Mn_{0.7}O_2$ electrode," *Electrochimica Acta*, vol. 48, no. 4, pp. 407-418, 2002.

[20] B. Xu and W. Zhang, "Modification of vertically aligned carbon nanotubes with $RuO_2$ for a solid-state pH sensor," *Electrochimica Acta*, vol. 55, no. 8, pp. 2859-2864, 2010.

[21] R.S. Chen, Y.S. Chen, Y.S. Huang, Y.L. Chen, Y. Chi, C.S. Liu, K.K. Tiong and A.J. Carty, "Growth of IrO2 films and nanorods by means of CVD: An example of compositional and morphological control of nanostructures," *Chemical Vapor Deposition*, vol. 9, no. 6, pp. 301-305, 2003.

[22] B.H. Meekins and P.V. Kamat, "Role of Water Oxidation Catalyst IrO 2 in Shuttling Photogenerated Holes Across $TiO_2$ Interface," *The Journal of Physical Chemistry Letters*, vol. 2, no. 18, pp. 2304-2310, 2011.

[23] Y.M. Chen, J.H. Cai, Y.S. Huang, K.Y. Lee, D.S. Tsai and K.K. Tiong, "Deposition and characterization of $IrO_x$ nanofoils on carbon nanotube templates by reactive magnetron sputtering," *Thin Solid Films*, vol. 520, no. 7, pp. 2409-2413, 2011.

[24] R. Chen, H. Chang, Y. Huang, D. Tsai, S. Chattopadhyay and K. Chen, "Growth and characterization of vertically aligned self-assembled $IrO_2$ nanotubes on oxide substrates," *Journal of Crystal Growth*, vol. 271, no. 1, pp. 105-112, 2004.

[25] W. Huang, S. Deb, Y. Seo, S. Rao, M. Chiao and J. Chiao, "A passive radio-frequency pH-sensing tag for wireless food-quality monitoring," *Sensors Journal, IEEE*, vol. 12, no. 3, pp. 487-495, 2012.

[26] Y.M. Chen, J.H. Cai, Y.S. Huang, K.Y. Lee, D.S. Tsai and K.K. Tiong, "A nanostructured electrode of IrOx foil on the carbon nanotubes for supercapacitors," *Nanotechnology*, vol. 22, pp. 355708, 2011.

[27] S.F. Cogan, P.R. Troyk, J. Ehrlich, T.D. Plante and D.E. Detlefsen, "Potential-biased, asymmetric waveforms for charge-injection with activated iridium oxide (AIROF) neural stimulation electrodes," *Biomedical Engineering, IEEE Transactions on*, vol. 53, no. 2, pp. 327-332, 2006.

[28] S.F. Cogan, T. Plante and J. Ehrlich, "Sputtered iridium oxide films (SIROFs) for low-impedance neural stimulation and recording electrodes," vol. 2, pp. 4153-4156, 2004.

[29] S. Trasatti and P. Kurzweil, "Electrochemical supercapacitors as versatile energy stores," *Platinum Metals Rev*, vol. 38, no. 2, pp. 46-56, 1994.

[30] M. Chuang and J.A. Ho, "Efficient electrocatalytic oxidation of water: minimization of catalyst loading by an electrostatic assembly of hydrous iridium oxide colloids," *RSC Advances*, vol. 2, no. 10, pp. 4092-4096, 2012.

[31] C. Nguyen, O. Thumthan, C. Huang, U. Tata, Y. Hao and J. Chiao, "Chemical bath method to grow precipitated nanorods of iridium oxide on alumina membranes," *Micro & Nano Letters*, vol. 7, no. 12, pp. 1256-1259, 2012.

[32] D. Wei, M.J. Bailey, P. Andrew and T. Ryhänen, "Electrochemical biosensors at the nanoscale," *Lab on a Chip*, vol. 9, no. 15, pp. 2123-2131, 2009.

[33] Z. Wang and M. Brust, "Fabrication of nanostructure via self-assembly of nanowires within the AAO template," *Nanoscale Research Letters*, vol. 2, no. 1, pp. 34-39, 2007.

[34] A. Thormann, N. Teuscher, M. Pfannmöller, U. Rothe and A. Heilmann, "Nanoporous aluminum oxide membranes for filtration and biofunctionalization," *Small*, vol. 3, no. 6, pp. 1032-1040, 2007.

[35] C. Lin, T. Juo, Y. Chen, C. Chiou, H. Wang and Y. Liu, "Enhanced cyclic voltammetry using 1-D gold nanorods synthesized via AAO template electrochemical deposition," *Desalination*, vol. 233, no. 1, pp. 113-119, 2008.

[36] M. Wesche, M. Hüske, A. Yakushenko, D. Brüggemann, D. Mayer, A. Offenhäusser and B. Wolfrum, "A nanoporous alumina microelectrode array for functional cell–chip coupling," *Nanotechnology*, vol. 23, no. 49, pp. 495303, 2012.

[37] C. Nguyen, "Fabrication of Ph-Sensing Iridium Oxide Nanotubes on Patterned Electrodes Using Anodic Aluminum Oxide Nano-Template," *Sensors 2013 Conference, IEEE,* 2013.

[38] C. Lu, Z. Chen and H. Nalwa, "Anodic Aluminum OxideaBased Nanostructures and Devices," *Encyclopedia of Nanoscience and Nanotechnology*, vol. 11, no. 1, pp. 235-259, 2011.

[39] D. Al-Mawlawi, C. Liu and M. Moskovits, "Nanowires formed in anodic oxide nanotemplates," *Journal of Materials Research*, vol. 9, no. 04, pp. 1014-1018, 1994.

[40] S. Hwang, S. Jeong, H. Hwang, O. Lee and K. Lee, "Fabrication of highly ordered pore array in anodic aluminum oxide," *Korean Journal of Chemical Engineering*, vol. 19, no. 3, pp. 467-473, 2002.

[41] A. Belwalkar, E. Grasing, W. Van Geertruyden, Z. Huang and W. Misiolek, "Effect of processing parameters on pore structure and thickness of anodic aluminum oxide (AAO) tubular membranes," *Journal of Membrane Science*, vol. 319, no. 1, pp. 192-198, 2008.

[42] Y. Lin, Y. Sun, W. Jian, H. Chang, Y. Huang and J. Lin, "Electrical transport studies of individual IrO2 nanorods and their nanorod contacts," *Nanotechnology*, vol. 19, pp. 045711, 2008.

[43] F. Zhang, R. Barrowcliff, G. Stecker, W. Pan, D. Wang and S.T. Hsu, "Synthesis of metallic iridium oxide nanowires via metal organic chemical vapor deposition," *Japanese Journal of Applied Physics, Part*, vol. 2, 2005.

[44] M. Hara, T. John and T.E. Mallouk, "Photocatalytic oxidation of water by silica-supported tris (4, 4'-dialkyl-2, 2'-bipyridyl) ruthenium polymeric sensitizers and colloidal iridium oxide," *Chemistry of materials*, vol. 13, no. 12, pp. 4668-4675, 2001.

[45] A. Yu, I. Roes, A. Davies and Z. Chen, "Ultrathin, transparent, and flexible graphene films for supercapacitor application," *Applied Physics Letters*, vol. 96, no. 25, pp. 253105-253105-3, 2010.

[46] B.J. Venton, H. Zhang, P.A. Garris, P.E. Phillips, D. Sulzer and R.M. Wightman, "Real-time decoding of dopamine concentration changes in the caudate–putamen during tonic and phasic firing," *Journal of neurochemistry*, vol. 87, no. 5, pp. 1284-1295, 2003.

[47] F. Arslan, "An amperometric biosensor for uric acid determination prepared from uricase immobilized in polyaniline-polypyrrole film," *Sensors*, vol. 8, no. 9, pp. 5492-5500, 2008.

[48] A. Liu, I. Honma and H. Zhou, "Amperometric biosensor based on tyrosinase-conjugated polysacchride hybrid film: Selective determination of nanomolar neurotransmitters metabolite of 3, 4-dihydroxyphenylacetic acid (DOPAC) in biological fluid," *Biosensors and Bioelectronics*, vol. 21, no. 5, pp. 809-816, 2005.

[49] P. Limousin, P. Krack, P. Pollak, A. Benazzouz, C. Ardouin, D. Hoffmann and A. Benabid, "Electrical stimulation of the subthalamic nucleus in advanced Parkinson's disease," *New England Journal of Medicine*, vol. 339, no. 16, pp. 1105-1111,1998.

[50] R. Lenigk, E. Lam, A. Lai, H. Wang, Y. Han, P. Carlier and R. Renneberg, "Enzyme biosensor for studying therapeutics of Alzheimer's disease," *Biosensors and Bioelectronics*, vol. 15, no. 9, pp. 541-547, 2000.

[51] J. Zhang, N. Trombly and A. Mason, "A low noise readout circuit for integrated electrochemical biosensor arrays," *Sensors 2004 Conference, IEEE*, pp. 36-39, 2004.

[52] F. Agnesi, S.J. Tye, J.M. Bledsoe, C.J. Griessenauer, C.J. Kimble, G.C. Sieck, K.E. Bennet, P.A. Garris, C.D. Blaha and K.H. Lee, "Wireless Instantaneous Neurotransmitter Concentration System-based amperometric detection of dopamine, adenosine, and glutamate for intraoperative neurochemical monitoring," *Journal of Neurosurgery*, vol. 111, no. 4, Oct, pp. 701-711, 2009.

[53] C.M. Yates, J. Butterworth, M.C. Tennant and A. Gordon, "Enzyme Activities in Relation to pH and Lactate in Postmortem Brain in Alzheimer-Type and Other Dementias," *Journal of Neurochemistry*, vol. 55, no. 5, pp. 1624-1630, 1990.

[54] A. Cornish-Bowden, "Fundamentals of enzyme kinetics" 4$^{th}$ ed., Wiley Blackwell, 2012.

[55] M. Dixon, "The effect of pH on the affinities of enzymes for substrates and inhibitors," *Biochemical Journal*, vol. 55, no. 1, pp. 161, 1953.

[56] F.H. Epstein, V.L. Hood and R.L. Tannen, "Protection of acid–base balance by pH regulation of acid production," *New England Journal of Medicine*, vol. 339, no. 12, pp. 819-826, 1998.

[57] J.G. Gaertner and P. Dhurjati, "Fractional factorial study of hybridoma behavior. 2. Kinetics of nutrient uptake and waste production," *Biotechnology Progress*, vol. 9, no. 3, pp. 309-316, 1993.

[58] T. Sakurai and Y. Husimi, "Real-time monitoring of DNA polymerase reactions by a micro ISFET pH sensor," *Analytical Chemistry*, vol. 64, no. 17, pp. 1996-1997, 1992.

[59] D.G. Pijanowska and W. Torbicz, "pH-ISFET based urea biosensor," *Sensors and Actuators B: Chemical*, vol. 44, no. 1, pp. 370-376, 1997.

[60] U.E. Spichiger-Keller, "Potentiometric chemical sensors and biological applications," *Chemical Sensors and Biosensors for Medical and Biological Applications*, pp. 199-257, 1998.

[61] J. Voldman, M.L. Gray and M.A. Schmidt, "Microfabrication in biology and medicine," *Annual Review of Biomedical Engineering*, vol. 1, no. 1, pp. 401-425, 1999.

[62] S. Amer and W. Badawy, "An integrated platform for bio-analysis and drug delivery," *Current Pharmaceutical Biotechnology*, vol. 6, no. 1, pp. 57-64, 2005.

[63] A. Fura, T.W. Harper, H. Zhang, L. Fung and W.C. Shyu, "Shift in pH of biological fluids during storage and processing: effect on bioanalysis," *Journal of Pharmaceutical and Biomedical Analysis*, vol. 32, no. 3, pp. 513-522, 2003.

[64] T. Sakurai and Y. Husimi, "Real-time monitoring of DNA polymerase reactions by a micro ISFET pH sensor," *Analytical Chemistry*, vol. 64, no. 17, pp. 1996-1997, 1992.

[65] A. Richter, G. Paschew, S. Klatt, J. Lienig, K. Arndt and H.P. Adler, "Review on hydrogel-based pH sensors and microsensors," *Sensors*, vol. 8, no. 1, pp. 561-581, 2008.

[66] T.P. Jones and M.D. Porter, "Optical pH sensor based on the chemical modification of a porous polymer film," *Analytical Chemistry*, vol. 60, no. 5, pp. 404-406, 1988.

[67] Z. Jin, Y. Su and Y. Duan, "An improved optical pH sensor based on polyaniline," *Sensors and Actuators B: Chemical*, vol. 71, no. 1, pp. 118-122, 2000.

[68] K. Shiu, F. Song and H. Dai, "Potentiometric pH sensor with anthraquinonesulfonate adsorbed on glassy carbon electrodes," *Electroanalysis*, vol. 8, no. 12, pp. 1160-1164, 1996.

[69] P.J. Kinlen, J.E. Heider and D.E. Hubbard, "A solid-state pH sensor based on a Nafion-coated iridium oxide indicator electrode and a polymer-based silver chloride reference electrode," *Sensors and Actuators B: Chemical*, vol. 22, no. 1, pp. 13-25, 1994.

[70] H.N. McMurray, P. Douglas and D. Abbot, "Novel thick-film pH sensors based on ruthenium dioxide-glass composites," *Sensors and Actuators B: Chemical*, vol. 28, no. 1, pp. 9-15, 1995.

[71] A. Fog and R.P. Buck, "Electronic semiconducting oxides as pH sensors," *Sensors and Actuators*, vol. 5, no. 2, pp. 137-146, 1984.

[72] C. Nguyen, W. Huang, S. Rao, H. Cao, U. Tata, M. Chiao and J. Chiao, "A Sol-gel Iridium Oxide based pH Sensor Array on Flexible Polyimide Substrate," *Sensors Journal, IEEE,* vol. 13, no. 10, pp. 3857-3864, 2013.

[73] A. Errachid, A. Ivorra, J. Aguilo, R. Villa, N. Zine and J. Bausells, "New technology for multi-sensor silicon needles for biomedical applications," *Sensors and Actuators B: Chemical*, vol. 78, no. 1, pp. 279-284, 2001.

[74] Marina Vorozhtsova, Jana Drbohlavova and Jaromir Hubalek, "Chemical Microsensors with Ordered Nanostructures, Microsensors," ISBN: 978-953-307-170-1, InTech, DOI: 10.5772/18066. Available from: http://www.intechopen.com/books/microsensors/chemical-microsensors-with-ordered-nanostructures

[75] B. Mizaikoff and C. Kranz, "Interfacing chemistry with microdevices: Potential and challenges of chemical microsensors," *Advanced Semiconductor Devices and Microsystems 2002*, pp. 307-316, 2002.

[76] A. Düzgün, G.A. Zelada-Guillén, G.A. Crespo, S. Macho, J. Riu and F.X. Rius, "Nanostructured materials in potentiometry," *Analytical and Bioanalytical Chemistry*, vol. 399, no. 1, pp. 171-181, 2011.

[77] M.C. Frost and M.E. Meyerhoff, "Implantable chemical sensors for real-time clinical monitoring: progress and challenges," *Current Opinion in Chemical Biology*, vol. 6, no. 5, pp. 633-641, 2002.

[78] R. Vargas, T. Goto, W. Zhang and T. Hirai, "Epitaxial growth of iridium and platinum films on sapphire by metalorganic chemical vapor deposition," *Applied Physics Letters*, vol. 65, no. 9, pp. 1094-1096, 1994.

[79] B. Cao and W. Cai, "From ZnO nanorods to nanoplates: chemical bath deposition growth and surface-related emissions," *The Journal of Physical Chemistry C*, vol. 112, no. 3, pp. 680-685, 2008.

[80] M. Knez, K. Nielsch and L. Niinistö, "Synthesis and surface engineering of complex nanostructures by atomic layer deposition," *Advanced Materials*, vol. 19, no. 21, pp. 3425-3438, 2007.

[81] A. Huczko, "Template-based synthesis of nanomaterials," *Applied Physics A*, vol. 70, no. 4, pp. 365-376, 2000.

[82] J. Hulteen, "A general template-based method for the preparation of nanomaterials," *Journal of Materials Chemistry*, vol. 7, no. 7, pp. 1075-1087, 1997.

[83] T. Katsube, I. Lauks and J. Zemel, "pH-sensitive sputtered iridium oxide films," *Sensors and Actuators*, vol. 2, pp. 399-410, 1982.

[84] K. Yamanaka, "Anodically electrodeposited iridium oxide films (AEIROF) from alkaline solutions for electrochromic display devices," *Japanese Journal of Applied Physics*, vol. 28, no. 4R, pp. 632, 1989.

[85] S. Yao, M. Wang and M. Madou, "A pH electrode based on melt-oxidized iridium oxide," *Journal of the Electrochemical Society*, vol. 148, no. 4, pp. H29-H36, 2001.

[86] W. Huang, H. Cao, S. Deb, M. Chiao and J. Chiao, "A flexible pH sensor based on the iridium oxide sensing film," *Sensors and Actuators A: Physical*, vol. 169, no. 1, pp. 1-11, 2011.

[87] E. Mafakheri, A. Salimi, R. Hallaj, A. Ramazani and M.A. Kashi, "Synthesis of iridium oxide nanotubes by electrodeposition into polycarbonate template: fabrication of chromium (III) and arsenic (III) electrochemical sensor," *Electroanalysis*, vol. 23, no. 10, pp. 2429-2437, 2011.

[88] A.N. Bezbaruah and T.C. Zhang, "Fabrication of anodically electrodeposited iridium oxide film pH microelectrodes for microenvironmental studies," *Analytical Chemistry*, vol. 74, no. 22, pp. 5726-5733, 2002.

[89] S.A. Marzouk, "Improved electrodeposited iridium oxide pH sensor fabricated on etched titanium substrates," *Analytical Chemistry*, vol. 75, no. 6, pp. 1258-1266, 2003.

[90] D.C. Howse, J.J. Caronna, T.E. Duffy and F. Plum, "Cerebral energy metabolism, pH, and blood flow during seizures in the cat," *American Journal of Physiology--Legacy Content*, vol. 227, no. 6, pp. 1444-1451, 1974.

[91] R.D. Meyer, S.F. Cogan, T.H. Nguyen and R.D. Rauh, "Electrodeposited iridium oxide for neural stimulation and recording electrodes," *Neural Systems and Rehabilitation Engineering, IEEE Transactions on*, vol. 9, no. 1, pp. 2-11, 2001.

[92] A. Weltin, B. Enderle, J. Kieninger and G.A. Urban, "A novel, multiparametric, flexible microsensor for metabolic monitoring in vivo,", pp. 1-3, 2013.

[93] N.V. Kulagina, L. Shankar and A.C. Michael, "Monitoring glutamate and ascorbate in the extracellular space of brain tissue with electrochemical microsensors," *Analytical Chemistry*, vol. 71, no. 22, pp. 5093-5100, 1999.

[94] W. Huang, S. Deb, Y. Seo, S. Rao, M. Chiao and J. Chiao, "A passive radio-frequency pH-sensing tag for wireless food-quality monitoring," *Sensors Journal, IEEE*, vol. 12, no. 3, pp. 487-495, 2012.

[95] M.W. Shinwari, D. Zhitomirsky, I.A. Deen, P. Selvaganapathy, M.J. Deen and D. Landheer, "Microfabricated reference electrodes and their biosensing applications," *Sensors*, vol. 10, no. 3, pp. 1679-1715, 2010.

[96] P. Gros, H. Durliat and M. Comtat, "Use of polypyrrole film containing Fe $(CN)_6^{3-}$ as pseudo-reference electrode: application for amperometric biosensors," *Electrochimica Acta*, vol. 46, no. 5, pp. 643-650, 2001.

[97] J.J. Pedrotti, L. Angnes and I.G. Gutz, "Miniaturized reference electrodes with microporous polymer junctions," *Electroanalysis*, vol. 8, no. 7, pp. 673-675, 1996.

[98] V.M. Tolosa, K.M. Wassum, N.T. Maidment and H.G. Monbouquette, "Electrochemically deposited iridium oxide reference electrode integrated with an electroenzymatic glutamate sensor on a multi-electrode arraymicroprobe," *Biosensors and Bioelectronics*, vol. 42, pp. 256-260, 2013.

[99] T. Matsumoto, A. Ohashi and N. Ito, "Development of a micro-planar Ag/AgCl quasi-reference electrode with long-term stability for an amperometric glucose sensor," *Analytica Chimica Acta*, vol. 462, no. 2, pp. 253-259, 2002.

[100] S. Park, S.B. Jun, S. Park, H.C. Kim and S.J. Kim, "Application of a new Cl-plasma-treated Ag/AgCl reference electrode to micromachined glucose sensor," *Sensors Journal, IEEE*, vol. 3, no. 3, pp. 267-273, 2003.

[101] F. Moussy and D.J. Harrison, "Prevention of the rapid degradation of subcutaneously implanted Ag/AgCl reference electrodes using polymer coatings," *Analytical Chemistry*, vol. 66, no. 5, pp. 674-679, 1994.

[102] W.F. Jackson and B.R. Duling, "Toxic effects of silver-silver chloride electrodes on vascular smooth muscle," *Circulation research*, vol. 53, no. 1, Jul, pp. 105-108, 1983.

[103] Y. Zhang, D.S. Bindra, M. Barrau and G.S. Wilson, "Application of cell culture toxicity tests to the development of implantable biosensors," *Biosensors and Bioelectronics*, vol. 6, no. 8, pp. 653-661, 1991.

[104] J.D. Weiland and D.J. Anderson, "Chronic neural stimulation with thin-film, iridium oxide electrodes," *Biomedical Engineering, IEEE Transactions on*, vol. 47, no. 7, pp. 911-918, 2000.

[105] J.D. Weiland, D.J. Anderson and M.S. Humayun, "In vitro electrical properties for iridium oxide versus titanium nitride stimulating electrodes," *Biomedical Engineering, IEEE Transactions on*, vol. 49, no. 12, pp. 1574-1579, 2002.

[106] E. Slavcheva, R. Vitushinsky, W. Mokwa and U. Schnakenberg, "Sputtered iridium oxide films as charge injection material for functional electrostimulation," *Journal of the Electrochemical Society*, vol. 151, no. 7, pp. E226-E237, 2004.

[107] I. Lee, C. Whang, J. Park, D. Lee and W. Seo, "Biocompatibility and charge injection property of iridium film formed by ion beam assisted deposition," *Biomaterials*, vol. 24, no. 13, pp. 2225-2231, 2003.

[108] S.A. Grant, K. Bettencourt, P. Krulevitch, J. Hamilton and R. Glass, "In vitro and in vivo measurements of fiber optic and electrochemical sensors to monitor brain tissue pH," *Sensors and Actuators B: Chemical*, vol. 72, no. 2, pp. 174-179, 2001.

[109] R.K. Franklin, M.D. Johnson, K. Scottt, J.H. Shim, H. Nam, D.R. Kipke and R.B. Brown, "Iridium oxide reference electrodes for neurochemical sensing with MEMS microelectrode arrays," *Sensors 2005 Conference, IEEE,* 2005.

[110] G. Inzelt, "Pseudo-reference Electrodes," Springer, pp. 331-332, 2013.

[111] I.A. Ges, B.L. Ivanov, A.A. Werdich and F.J. Baudenbacher, "Differential pH measurements of metabolic cellular activity in nl culture volumes using microfabricated iridium oxide electrodes," *Biosensors and Bioelectronics*, vol. 22, no. 7, pp. 1303-1310, 2007.

[112] Y. Kamegaya, K. Sasaki, M. Oguri, T. Asaki, H. Kobayashi and T. Mitamura, "Improved durability of iridium oxide coated titanium anode with interlayers for oxygen evolution at high current densities," *Electrochimica Acta*, vol. 40, no. 7, pp. 889-895, 1995.

[113] A. Osaka, T. Takatsuna and Y. Miura, "Iridium oxide films via sol-gel processing," *Journal of Non-Crystalline Solids*, vol. 178, pp. 313-319, 1994.

[114] A.J. Bard and L.R. Faulkner, "Electrochemical methods: fundamentals and applications," 2nd ed., Wiley Blackwell, 1980.

[115] M. Hsu, Y. Chen, C. Lee and H. Chiu, "Gold nanostructures on flexible substrates as electrochemical dopamine sensors," *ACS applied materials & interfaces*, vol. 4, no. 10, pp. 5570-5575, 2012.

[116] D. Ravi Shankaran, N. Uehara and T. Kato, "Sol–gel derived metal dispersed ceramic–graphite composite electrode for amperometric determination of dopamine," *Analytica Chimica Acta*, vol. 478, no. 2, pp. 321-327, 2003.

[117] F. Thomas and G. Henze, "Introduction to voltammetric analysis: theory and practice," CSIRO Publishing, 2001.

[118] H. Mohammad-Shiri, M. Ghaemi, S. Riahi and A. Akbari-Sehat, "Computational and electrochemical studies on the redox reaction of dopamine in aqueous solution," *Int.J.Electrochem.Sci*, vol. 6, pp. 317-336, 2011.

[119] M.R. Bari and R.E. Sabzi, "Amperometric Determination of Dopamine on a Glassy Carbon Electrode Chemically Modified with Cobalt Pentacyanonitrosylferrate," *Asian Journal of Chemistry*, vol. 20, no. 5, pp. 3357, 2008.

[120] J. Klein, S. Clauson and S. Cogan, "Morphology and charge capacity of sputtered iridium oxide films," *Journal of Vacuum Science & Technology A*, vol. 7, no. 5, pp. 3043-3047, 1989.

[121] T. Luczak and M. Beltowska-Brzezinska, "Gold electrodes modified with gold nanoparticles and thio compounds for electrochemical sensing of dopamine alone and in presence of potential interferents. A comparative study," *Mikrochimica Acta*, vol. 174, no. 1-2, pp. 19-30, 2011.

[122] J. Li and N. Wu, "Biosensors based on nanomaterials and nanodevices," CRC Press, 2013.

[123] S.F. Cogan, J. Ehrlich, T.D. Plante, A. Smirnov, D.B. Shire, M. Gingerich and J.F. Rizzo, "Sputtered iridium oxide films for neural stimulation electrodes," *Journal of Biomedical Materials Research Part B: Applied Biomaterials*, vol. 89, no. 2, pp. 353-361, 2009.

[124] G. Li and P. Miao, "Theoretical Background of Electrochemical Analysis," in *Electrochemical Analysis of Proteins and Cells*, Springer, pp. 5-18, 2013.

[125] A. Shrivastava and V.B. Gupta, "Methods for the determination of limit of detection and limit of quantitation of the analytical methods," *Chronicles of Young Scientists*, vol. 2, no. 1, pp. 21, 2011.

[126] J. Subbaroyan, D.C. Martin and D.R. Kipke, "A finite-element model of the mechanical effects of implantable microelectrodes in the cerebral cortex," *Journal of Neural Engineering*, vol. 2, no. 4, pp. 103, 2005.

[127] R. Zhu, G. Huang, H. Yoon, C.S. Smith and V.K. Varadan, "Biomechanical strain analysis at the interface of brain and nanowire electrodes on a neural probe," *Journal of Nanotechnology in Engineering and Medicine*, vol. 2, no. 3, pp. 031001, 2011.

[128] H. Lee, R.V. Bellamkonda, W. Sun and M.E. Levenston, "Biomechanical analysis of silicon microelectrode-induced strain in the brain," *Journal of Neural Engineering*, vol. 2, no. 4, pp. 81, 2005.

[129] K. Lee, J. He, A. Singh, S. Massia, G. Ehteshami, B. Kim and G. Raupp, "Polyimide-based intracortical neural implant with improved structural stiffness," *Journal of Micromechanics and Microengineering*, vol. 14, no. 1, pp. 32, 2004.

[130] G.C. McConnell, T.M. Schneider, D.J. Owens and R.V. Bellamkonda, "Extraction force and cortical tissue reaction of silicon microelectrode arrays implanted in the rat brain," *Biomedical Engineering, IEEE Transactions on*, vol. 54, no. 6, pp. 1097-1107, 2007.

[131] A. Gilletti and J. Muthuswamy, "Brain micromotion around implants in the rodent somatosensory cortex," *Journal of Neural Engineering*, vol. 3, no. 3, pp. 189, 2006.

[132] K. Lee, A. Singh, J. He, S. Massia, B. Kim and G. Raupp, "Polyimide based neural implants with stiffness improvement," *Sensors and Actuators B: Chemical*, vol. 102, no. 1, pp. 67-72, 2004.

## Biographical Information

Cuong. M. Nguyen was born in Hanoi, Vietnam. He received his B.Sc. degree in Mechatronics from Department of Mechanical Engineering at the Hanoi University of Technology (Vietnam) in 2008 with his thesis title “Implementation of Symbolic Methods in Automated Calculation of Differential Equations of Motion for Multi-body Mechanical Systems” (in Vietnamese). Since 2010, he joined iMEMS research group and focused on design and fabrication of implantable and flexible electrochemical sensors featuring with nanostructured materials for biomedical applications. His current research interests include MEMS and BioMEMS devices fabrication, nanotechnology, flexible microelectronics, analog circuit design and low-power low-noise signal conditioning interface for neural signal recording. Nguyen has received several awards in various international/regional conferences and contests including in the BioWireleSS (2015), BMES (2014), MTT-S Fellowship (2013), Outstanding Teaching Award (2013) and in the Vietnamese National Olympiad on Strength of Materials (2006), and Chemistry (2003). He has authored/co-authored 14 peer-reviewed journal and conference publications and 8 short abstracts; also severed as a reviewer for multiple journals/conferences. Nguyen is a member of the Surface Mount Technology Association, Microwave Theory and Techniques Society (IEEE), and Biomedical Engineering Society.